Multi-wavelength observations of sprites over southern Africa

Stanislaus Ogechukwu Nnadih

A thesis submitted for the degree of PhD

SpaceLab, Department of Electrical Engineering

University of Cape Town

South Africa

January, 2020

SLI9–01D

Declaration

I, Stanislaus Ogechukwu Nnadih, declare that this thesis and the work presented therein is my own research work and has not previously been submitted for a degree or any other qualification at this University or any other institution.

SIGNATURE:.....Signed by candidate

DATE: ...17...January, 2020

Abstract

Sprites are short-lived, optical upper atmospheric lightning-induced phenomena that occur above an active thunderstorm, at an altitude range of 40 - 85 km. They are often described as electrical discharges in the mesosphere, following mostly large positive cloud-to-ground lightning discharges. Since their discovery in the late 1980s, sprites have been observed extensively in other continents except in Africa, where there is little or no active sprites-related research. Despite the numerous observations of sprites to date, there is no conclusive study that has reviewed the electron energies and the strength of the electric field within sprites as a function of altitude. This thesis presents the first ground-based observations of sprites in southern Africa. These observations were conducted at the South African Astronomical Observatory, Sutherland, South Africa, during the austral summer of 2015/2016, 2016/2017 and 2017/2018, as well as at a site that is close to South African Square Kilometre Array, Carnarvon in 2017/2018. Sprites were observed using multiple cameras that were filtered at specific wavelengths. In 5 out of 65 nights of observations, 113 video frames containing one or more sprites were recorded, comprising different morphologies (Carrot-single (10%), Carrot/Column (10%), Carrot-groups (37%), Column-groups (12%), Tree-like (4%), Unclassified (23%), Jelly-fish (3%)). These events were between 429 to 890 km away from the observer. The error in this distance estimate was ± 5% of the distance. During these observations, the cloud-top temperatures of the storms that initiated these events was about -58 degrees Celsius. Sprite events observed at specific wavelengths suggest that the first positive band of N2 dominates at the upper altitudes (around 65 km). By using the Maxwell-Boltzmann energy distribution function in collisional plasma, the average characteristic electron energies and the strength of the electric fields in sprites were estimated as 5.5 eV and 150 V/m respectively, which were comparable to those inferred from space-based observations. The charge moment change of the lightning strokes associated with the observed events agreed with the threshold for dielectric breakdown of the mesosphere and correlates well with the observed sprites brightness. The study also showed that the average detection rate for sprites in southern Africa was 0.14 sprites/minutes and that the carrot-shaped sprites are usually accompanied by an increase in the charged moment as compared to the columniform sprites.

Acknowledgements

The years I spent on this program have been the most intense and exhausting years of my life. However, it has also been memorable and rewarding. I thank God for his grace and favour during this period.

I am grateful to my supervisor, Prof. Peter Martinez, for his advice and encouragement through all the difficult challenges I encountered in this study. His steadfast support and excellent contributions in this study are greatly appreciated.

I am also thankful to my second supervisor, Prof. Michael Kosch, for the opportunity to bring to fruition the South African National Space Agency's dream of recording sprite events using ground-based systems in southern Africa. His boundless enthusiasm for research, optimism in the face of difficult situations and academic support is immensely appreciated.

Prof. Peter and Prof Michael made me understand that persistence and resilience in the quest to surmount difficulties often leads to success. They taught me what it means to be a good scientist. It has been a privilege to work with them. I sincerely appreciate their efforts. Thank you, Peter and Michael.

I also wish to thank Dr Martin Fullekrug for sharing his years' experience in sprites-research, and to Joszef Bor, Stefan Lot, Jeff Lapierre, Chris Lennard and Janusz Mlynarczyk for their generous support at various stages in this study.

This thesis could not have been completed without the supporting data that were provided by the South African Weather Service, the Earth Network Total Lightning Network and the Climate System Analysis Group in the Department of Environmental and Geographical Science at the University of Cape Town, and the support of the South African Astronomical Observatory to host our instrument.

Last, but not least, I would want to thank my family for moral support during these last three years and in a special way, to thank the management of the African Regional Centre for Space Science and Technology in English, The Nigerian Space Agency, for the opportunity to study in the Republic of South Africa.

Stanislaus Ogechukwu Nnadih
January, 2020

This study is supported by the National Research Foundation (South Africa) through grant number 105535. The instruments used for the observations were provided by the Science Centre of the South African National Space Agency.

Dedication

This work is dedicated to God.

Contents

List of Figures

List of Tables

List of Abbreviations and Symbols

AGC	Automatic Gain Control
AGU	American Geophysical Union
AMMA	Africa Monsoon Multidisciplinary Analysis
APT	Automatic Photoelectric Telescope
BLC	Black Light Control
CCD	Charge Coupled Device
CG	Cloud to Ground
CMC	Charge Moment Change
CSAG	Climate System Analysis
DE	Detection Efficiency
DSP	Digital Signal Processor
ELF	Extreme Low Frequency
ELVES	Emissions of Light and Very low-frequency perturbations from Electro-magnetic pulse Source
EM	Electromagnetic spectrum
EMP	Electro Magnetic Pulse
ENTLN	Earth Network Total Lightning Network
EUMETSAT	European Meteorological Satellite
FOV	Field of View
GPS	Global Positioning System
Ho_x	Oxides of Hydrogen
IC	Intra Cloud lightning discharge
LDN	Lightning Detection Network
LIS	Lightning Imaging Sensor
MCC	Mesoscale Convective Complex
MCS	Mesoscale Convective Storms
MDF	Magnetic Direction Finding
NTP	Network Timing Protocol
N_2(1PG)	First Positive Group Nitrogen Neutral
N_2(2PG)	Second Positive Group Nitrogen Neutral

$\mathrm{N_2}^+$(1NG)	First Negative (ions) Group Nitrogen Neutral
$\mathrm{No_x}$	Oxides of Nitrogen
OSR	Optical Space Research
QE	Quasi Electrostatic
RF	Radio Frequency
SAAO	South African Astronomical Observatory
SAIP	South African Institute of Physics
SALDN	South African Lightning Detection Network
SANSA	South African National Space Agency
SA-SKA	South African Square Kilometre Array
SAT24	Satellite 24
SAWS	South African Weather Service
SNR	Signal to Noise Ratio
TLE	Transient Luminous Event
TOA	Time of Arrival
TOGA	Time of Group Arrival
TV	Television
UFO	Unidentified Flying Object
UTC	Universal Time Coordinate
VERSIM	VLF ELF Remote Sensing of the Ionosphere and Magnetosphere
VLF	Very Low Frequency
WTLN	WeatherBug Total Lightning Network
WWLLN	World-Wide Lightning Location Network

a	Acceleration
h	Altitude
$Star_{\mathrm{avg}}$	Average star brightness
K	Boltzmann constant
Q_{o}	Characteristic electron energy
q	Charge of electrons
E_{k}	Critical breakdown
E	Electric field
θ	Elevation angle
Q	Energy of the electrons
$f(v)$	Flux of electron within sprites
$Sprites_{\mathrm{flux}}$	Flux of sprite events
F	Force
d	Ground distance from the camera to the storm
H_{NS}	Horizontal magnetic field
$Kler$	Klerefontein
$BLNTR$	Lightning Detection Sensor tag
m	Mass of electron
N_2	Nitrogen emission
O	Observer position
R_{e}	Radius of the Earth
T_{R}	Reversal temperature
SR	Schumann Resonance
$Sky_{\mathrm{bk1}}, Sky_{\mathrm{bk2}}$	Sky background pixel value without the pixel value of sprite events
$SP + Sky_{\mathrm{bk}}$	Sprite events with background sky pixel value
$Suth$	Sutherland
T	Temperature
t	Time between collision of electron
v	Velocity
H_{EW}	Vertical electric field

Chapter 1

Introduction

Anecdotal accounts of unusual sporadic optical phenomena over active thunderstorms have been found in the scientific literature for many years (MacKenzie and Toynbee 1886; Davidson 1893; Boys 1926; Malan 1937; Ashmore 1950; Wilson 1956; Powell 1968; Corliss 1977; Vonnegut 1980) prior to the first accidentally recorded image in late 1980's (Franz et al. 1990). For instance, in 1876, an experimental scientist (Boys 1926) reported seeing a series of unusual upwards lightning phenomena in the distant horizon. He noted:

> *"... for every flash seen in the rain cloud and below, and simultaneous with it, there were one or more very slender flashes of typical lightning form from the cloud upwards and many times as long as the usual kind of lightning below. These reached one-third or perhaps half-way towards the stars... and in one instance, there were seven of these flashes going simultaneously into the clear sky".*

These serendipitous observations of upwards lightning phenomena were also subjectively described by other early ground-based observers. They used different phrases to describe what they saw, which include "... a continuous dart of light...resembling rockets more than light" (MacKenzie and Toynbee 1886), "a luminous trail shot up to 15 degrees or so, faster than a rocket" (Everett 1903), " a long and weak streamer of reddish hue" (Malan 1937), "flames appearing to rise from the top of the cloud" (Ashmore 1950) and "...the discharge assumed a shape similar to the root of an inverted tree" (Wood 1951). However, these descriptions were ignored by the scientific community, largely because they were anecdotal and/or were not captured on a photographic image (William et al. 1998).

There were also a few other unverifiable airborne eyewitness reports of these rare forms of lightning that were not openly reported by the observers because the scientific community was skeptical of these unusual upwards lightning phenomena (William et al. 1998). In 1980, Vaughan and Vonnegut (1982) gathered and published these reports from the airborne observers in the Aircraft Owners and Pilots Association (AOPA) Newsletter, encouraging their readers to report if they had seen such lightning phenomena. This publication emboldened some of the pilots to describe what they had seen over thunderstorms. More than 10 detailed reports were received within a few months from various pilots. Each of them used different analogies to present verbal pictures of their observations. Some of them recommended that it was not safe to fly too close over the top of the storm cloud and that further studies need to be made to improve our understanding of the electrical processes taking place in thunderclouds (Vaughan 1989).

1.1 Discovery of sprites

The first serendipitous recording of a sprite was obtained purely by chance in 1989 (Franz et al. 1990), while a group of researchers at the University of Minnesota were calibrating their optical instrument in preparation for a sounding rocket experiment. As part of the calibration routine the instruments, which comprised a low-light television camera, a recorder and a video monitor, were positioned to record images of the stars and a distant lightning storm. While the camera was pointing in the direction of that storm, the monitor displayed huge twin flashes of light above the horizon (William et al. 1998). The images of these recorded events accurately matched the characteristics of the phenomena that had been verbally reported by earlier observers between 1876 and 1989. There were also other additional video observations of these events that were acquired using the space shuttle, between 1989 and 1991 (William et al. 1998). These images and video frame data confirmed the existence of these unusual phenomena above active thunderstorms, which finally became known as "sprites" because of their fleeting, mysterious nature (Sentman and Wescott 1994).

The discovery of sprites confirmed the prediction of Wilson (1956), who first understood that the relationship between the thundercloud electric field, which decreases with altitude r, (Figure 1.1), and the critical breakdown field $\mathrm{E_k}$ suggests that there is a height above which the electric force due to the cloud will exceed the gas discharge threshold that will result in an observable optical emission at that altitude.

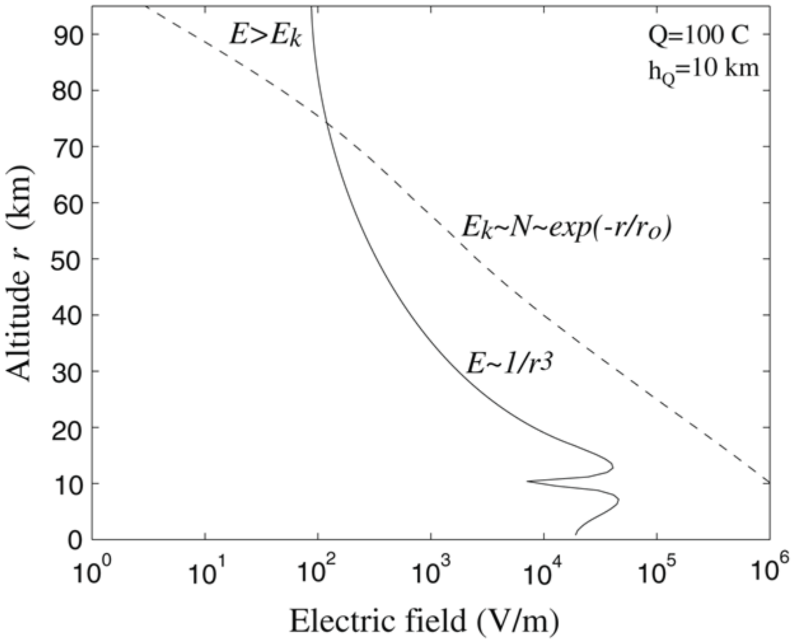

Figure 1.1: Altitude profile for dielectric breakdown of the atmosphere (Wilson 1956) (dashed line) and for the electric field from a lightning strike (Solid line).

This discovery of sprites also sparked off interest in lightning strike phenomena and the potential dangers it might pose to crewed spacecraft during take-off or landing. This interest necessitated a series of space/ground-based observations of sprites, which finally led to the discovery of some other stratospheric/mesospheric lightning-induced optical phenomena such as the Emissions of Light and Very low-frequency perturbations from Electro-magnetic pulse Sources (ELVES) that consist of a horizontal brightening flash spanning several hundred kilometers at the altitudes of the air-glow layers, the

Jets (blue jets and Gigantic jets) (Wescott et al. 1995), and the Halos. These various types of transient optical phenomena are collectively referred to as Transient Luminous Events(TLEs).

1.2 General characteristics of sprites

Sprites are short-lived, optical upper atmospheric lightning phenomena that occur above an active thunderstorm, at an altitude range of 40 to 80 km (Barrington-Leigh and Inam 1999). They are often described as electrical discharges in the mesosphere, following large positive Cloud-to-Ground (+CG) lightning discharges (Sentman et al. 1995; Winckler et al. 1999; Liu et al. 2015). Although, in rare cases, negative Cloud-to-Ground (-CG) and Intra-Cloud lightning discharges have also been known to initiate sprites (Barrington-Leigh 2001; Suzuki et al. 2006; Ohkubo et al. 2005; der Velde et al. 2006; Taylor et al. 2008; Liu et al. 2012). There are a few authors that suggest that sprites can also be initiated even when the lightning electric field is far below the theoretical breakdown threshold electric field E_k (Kosar et al. 2012). The tendency for this to occur was attributed to the existence of mesospheric irregularities (Gamero et al. 2011; Qin et al. 2012; 2013), which enhance the electron density at this altitude, making it possible for sprites to be initiated below the conventional breakdown threshold.

Sprites achieve their maximum brightness at an altitude range of 65 – 85 km (Neubert et al. 2008), lasting a few milliseconds (Sentman et al. 1995), and a width that spans several tens of kilometres at their widest point (Lyons 1996). When observed with a colour camera, sprites appear to have an upper red portion and a wispy faint blue tendril below the upper segment (Figure 1.2B). Spectroscopic observations of sprites reveal that whilst the red appearance originates from electron impact excitation of the first positive nitrogen neutral transition(N_2(1PG)), the blueish tendrils result from a combination of the first negative ions(N_2^+(1NG)) and second positive neutral emissions in nitrogen (N_2(2PG)) (Hampton et al. 1996; Armstrong et al. 1998; Suszcynsky et al. 1998; Jehl and Blanc 2013). Photometric observations of sprites reveal that the blueish emission from sprites has shorter duration (~1 - 5 ms) than the red emissions, which in some cases may last up to ~100 ms. The shorter the blue emission and poor atmospheric transmission in the blue region due to Rayleigh scattering contributes to the factor that makes it difficult to observe the blue emissions of sprites using ground-based systems (Heavner et al. 2010).

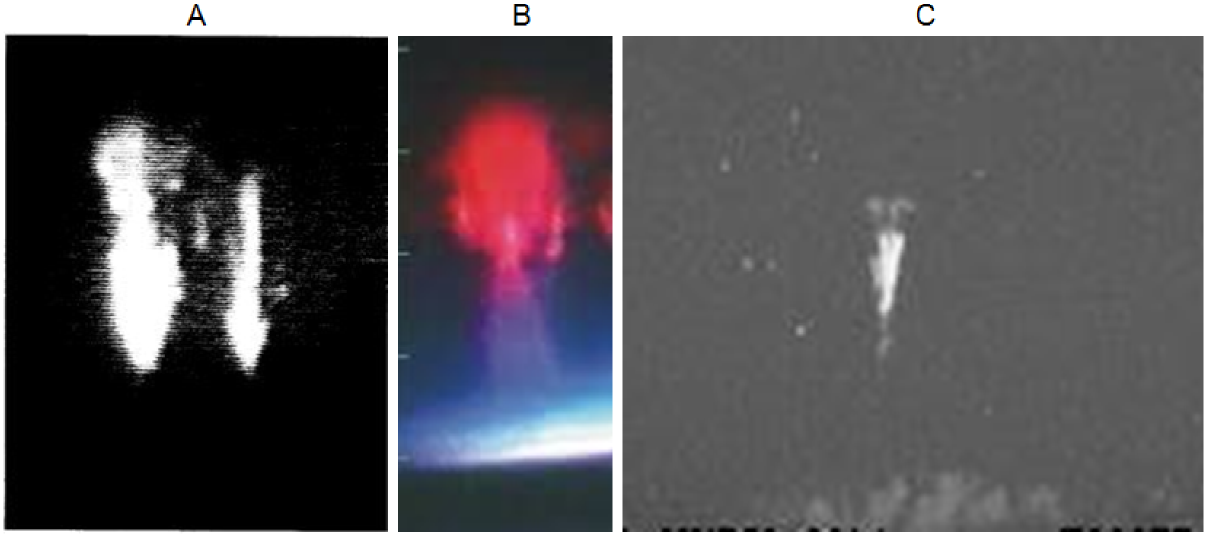

Figure 1.2: Some examples of historically significant sprite observations. (A) The first recorded sprite image (Franz et al. 1990). (B) The first sprite events recorded with a colour camera. (Sentman et al. 1995) (C) The first sprite events recorded in southern Africa (Nnadih et al. 2018).

High-speed imagery (1000 - 4000 frames per second(fps)) of sprites reveals that sprites tend to move downwards and then upwards (Stanley 1999; Stenbaek-Nielsen et al. 2013) with a speed in excess of 10^7 m/s. They exhibit several morphologies that are distinguished by the following descriptive names for the final structure of the emission as recorded by the observing instrument (Bor 2013): carrot, jelly-fish, column, angle, tree-like shapes, wishbone. Telescopic imagery of sprite events reveals thousands of growing channels, which consist of both vertical and slanted filamentary structures that have a diameter of the order of tens to hundreds of meters (Gerken et al. 2000). These structures are called sprite streamers. A streamer is a transient filamentary nonlinear ionized wave that propagates self-consistently in an electric field region (Liu et al. 2015). They are regarded as the building blocks of sprites (Liu and Pasko 2004; Pasko et al. 2013).

Sprites may occur singly or in a cluster of two or more (Sentman et al. 1995). The clustered events are further subclassified into homogeneous (sprites of the same morphological type) and inhomogeneous (sprites of different morphological types) events (Bor 2013). The tendency for sprites to appear in clusters was assumed to be caused by a horizontal fractal lightning discharge (Valdivia et al. 1997), which generates an electromagnetic pulse (EMP) that excites the optical emission in the lower ionosphere. These clusters can sometimes occur across $\sim$100 km track in the form of sequential luminous emissions that are displaced in time and space from each other, creating an illusion of motion in the sky, which most observers refer to as "dancing sprites" (Winckler et al. 1996; Lyons 1996; Fullekrug et al. 2013; Lu et al. 2013; Yang et al. 2013; Serge et al. 2015).

Several models have been proposed for the physical processes that are responsible for the initiation of sprites. These include:

1. The *radio wave heating model*, which postulates a low RF breakdown of the upper atmosphere as a result of a lightning discharge at the lower altitudes and suggests that a horizontal lightning discharge with intracloud charge moment change (CMC) between 600 and 800 C.km could initiate observable optical emissions (Milikh and Papadopoulos 1995).
2. The *quasi-electrostatic(QE) heating model*, which suggests that the temporal quasi-electrostatic field that exists at the high altitudes following an abrupt removal of charges (positive or negative thundercloud charges) at low altitudes could lead to

electron heating and excitation of optical emissions in the mesosphere (Pasko et al. 1997).

3. The *runaway electron model*, which stipulates that runaway electrons from large quasi-electrostatic fields produced by positive cloud-to-ground lightning discharges also initiate optical emissions that have the same characteristics as sprite events (Taranenko and Roussel-Dupre 1996).

Whilst the quasi-electrostatic heating model is the generally accepted mechanism for sprites initiation (Raizer et al. 1998; Valdivia et al. 1997; Pasko et al. 1998; Liu et al. 2016), this model is not able to account for certain observable characteristics associated with sprites phenomena. These characteristics include the diversity in shapes/structures of sprite events, the horizontal displacement between these events and their parent lightning strokes, as well as the time difference between the initiation of these events and the causative lightning discharges (Bell et al. 1998; Wescott et al. 2001; Cummer and Fullekrug 2001). There are a few studies that have provided insights into some of these sprites characteristics that were not explained by the QE model. For instance, these studies (Lyons 1996; Wescott et al. 2001; Sao-Sabbas et al. 2003) show that sprites tend to appear within 50 km from the parent lightning strokes, possibly because of the horizontally extended cloud-to-cloud (intra-cloud) lightning channels, which in some cases initiate sprites. Some other authors(Der Velde et al. 2006) suggest that for the most frequently observed sprite structures (the column and carrot-shaped sprites), the time difference between the causative lightning stroke and the sprite events are < 30ms for the column sprites, and up to about 200ms for the carrot-shaped sprites. They did not explain the factors that caused these time differences aside from the nature of the ELF/VLF sferic that initiated the events. However, study (Soula et al. 2009) has shown that the time difference between these events and their causative lightning strokes could be attributed to the nature of the Charge Moment Change (CMC) and current waveform that is associated with the corresponding lightning discharges.

Sprites research has been conducted extensively from space-based systems over central Africa, northern Australia (Sentman et al. 1995; Yair et al. 2004; Blanc et al. 2004) and South America, as well as over the Pacific and Indian oceans (Chern et al. 2006; Chen et al. 2008; Jehl and Blanc 2013; Sato et al. 2015). Dedicated satellite science payloads have been used to study sprites from space, for example, the Imager for Sprites and Upper Atmospheric Lightning (ISUAL) mission(Frey et al. 2016). Sprites have also been successfully studied using ground-based systems on different continents (Matsudo et al. 2007; Williams 2010; Yaniv et al. 2013), using various techniques such as radio measurements, theoretical analysis and numerical simulations(Liu et al. 2015; Pasko 2007; Fullekrug et al. 2013). These studies have led to some interesting discoveries, which are well documented in the scientific literature describing sprites phenomenology(Rodger 1999; Pasko 2015; Ebert 2010). These include, for example: the Extremely Low Frequency (ELF) radiations produced by the electrical current in sprites (Cummer 1998) and the energy deposited by a large sprite being of the order of 1 GJ (Heavner 2000)

Whilst some of these studies suggest that the initiation of sprites could chemically change the concentration of the oxides of nitrogen and hydrogen (NO_x, HO_x) in the mesosphere, which could lead to the cooling or heating of this layer, others show that this initiation could also affect long-distance communication through the lower ionosphere by altering the electron density in the ionosphere (Rakov and Uman 2003a; Watts 2016; Hiraki et al. 2008). Hence, it is important to determine the global occurrence rate of sprites in order to verify these assertions. The global occurrence rate for sprites has been estimated by several scholars (Sato and Fukunishi (2003) (0.5 sprites/minutes); Yair et al. (2004) (0.13 sprites/minute); Blanc et al. (2004), (1.33 sprites/minute); Ignaccolo et al. (2006) (2.8 sprites/minute); Chen et al. (2008), (1 sprites/minute)). However, these global estimates were extrapolated from local observations acquired over short periods and do not include any ground-based measurements from Africa, despite it being a lightning-rich continent (Christian et al. 2003).

Whereas Yair (2004), Blanc (2004) and Ignaccolo (2006) used a few hours of data for their estimate, Sato and Fukunishi (2003) used 216 days of ELF data containing 715,500 sprites. Their study was partly based on the charge-moment-change distribution of positive cloud-to-ground (+CG) lightning discharges and suggests that the use of charge moment change distribution for both +CG and -CG discharges could allow a more reliable empirically based estimation of sprites occurrence on a global scale. Charge-moment-change (CMC) is an important lightning metric (Wilson 1956; Hu 2002; Huang et al. 1999) that is not measured by the lightning detection networks. It is defined as the product of the electric charge and the altitude from which this charge is lowered to the ground. In order to verify Sato et al.'s assertion that the CMC of lightning discharges allows a more reliable estimate of sprites initiation on a global scale, the initiation of sprites as a function of charge moment change of both +CG and -CG lightning discharges needs to be verified. The charge moment change distribution of +CG lightning discharges has been estimated by Hu (2002) to be as low as 120 C.km. Since lightning discharges in southern Africa are mostly negative polarity (-CG) (Malan 1937), the initiation of sprites as a function of charge moment change of -CG lightning discharges can be verified from active sprite research in South Africa.

Although there are numerous ground/space-based observations (Hampton et al. 1996; Armstrong et al. 1998; Suszcynsky et al. 1998) that confirmed the molecular state of species of nitrogen within sprites at various altitudes using different data sets of sprites observed at specific wavelengths, these studies (Hampton et al. 1996; Armstrong et al. 1998; Suszcynsky et al. 1998) did not estimate the fluxes of electrons at different altitudes. There is no conclusive study that has reviewed the specific emission spectrum within a sprite as a function of altitude. Imaging a set of sprite events at two wavelengths (427.8 and 640 nm), as reported in this thesis, has allowed us to derive the absolute photon fluxes within sprites as a function of altitude.

Despite the numerous published observations of sprites to date, there are no substantive published studies of sprites in Africa, although there were a few days of observations carried out in West Africa during the 2006 AMMA (Africa Monsoon Multidisciplinary Analysis) campaign (Williams 2010). This dissertation describes the observations that led to the first ground-based recording of sprites over southern Africa. The preliminary results were presented at local and international conferences (SAIP 2016/2018, VERSIM 2016 and AGU 2016); based on the recommendations received at these scientific gatherings, the datasets were re-analyzed and the results were partly published in the South African Journal of Science. This thesis contains a detailed report of the series of ground-based observations of sprites over South Africa during the austral summer of 2015/2016, 2016/2017 and 2017/2018.

1.3 Open questions in sprite research

Space and ground-based optical observations (Sentman et al. 1995; Lyons 1996; Hardman et al. 2000; Yair et al. 2004; Neubert et al. 2001) have shown the occurrence of sprites on a global scale. Some of these studies were focused on mid-latitude thunderstorms, whereas the vast majority of thunderstorms occur in the tropics (Price 2004). Do the sprites in the tropics differ in any way from those that occur in mid-latitudes? How do the causative lightning discharges that initiate these sprites differ (if at all) in these regions? Some of the published studies were conducted over winter thunderstorms, which are generally much smaller than summer thunderstorms (Price 2004). Does the phenomenology of sprites produced by winter storms differ from those initiated by summer storms? Although the meteorological conditions suitable for sprites initiation over summer storms in the U.S are sufficiently known, the Mesoscale Convective Storms (MCS) that are usually associated with sprites differ from one place to another (Matsudo et al. 2007). Does the frequency of the sprites-producing storms in other regions and seasons, most especially during the austral summer storms in Africa, differ from those for the summer storms studied in the U.S.?

The color images of sprites show an upper red portion and bluish hair-like structures that extend downwards to the tops of the clouds. The extent to which these bluish sections extend up into the upper part of sprites remains unknown. The spectral measurements of sprites that confirmed the existence of various molecular states of nitrogen within sprite events suggest that these species have different threshold energies, lifetimes and quenching altitudes (Heavner et al. 2010). These studies either used a spectrometer and/or photometer to observe different sprite events at specific wavelengths and were therefore are not able to quantify or estimate the fluxes of electrons at different altitudes. Do the electron fluxes within sprites vary with altitude? Knowledge of this will assist us to estimate the characteristic electron energy and the strength of the electric field dissipated by sprite events at different altitudes.

1.4 Research objectives of this study

This research is aimed at contributing to what is already known about the sprites phenomena. It has characterized the occurrence of sprites in southern Africa. In addition, the study conducted a series of ground-based observations of sprite emissions at specific wavelengths in the red and blue regions of the electromagnetic spectrum. These emissions have different energy thresholds. The red emission of sprites is from the neutral N_2 (1PG) (635-675, 7.5 eV) and the blue emission from ionized N_2^+(1NG) (427.8 nm, 18.6 eV). Thus, the study set out to:

1. Observe a series of sprite events in southern Africa at multiple wavelengths, using ground-based systems;
2. Derive the absolute fluxes of the electrons within sprite events at different altitudes;
3. Determine the characteristics (nature, temperature, size) of the austral summer thunderstorms that initiate sprites in South Africa; and
4. Derive the characteristic electron energy and the strength of the electric field within sprite events, using ground-based optical systems.

1.5 Contributions of this thesis

The contributions of this study are as follows:

1. The study made the first ground-based observations of sprites in southern Africa. These observations suggest that the morphology of sprites in southern Africa is same as those observed elsewhere, and that the frequency of the sprites-producing convective thunderstorms is lower compared to the occurrence of such thunderstorms in central Europe and the Americas.
2. The study showed that the fluxes of electrons within sprites, when observed in the specific wavelength range (635 - 675 nm), peak between 55 km and 70 km in those sprite events, for which the fluxes of the electrons were estimated.
3. The study uses a new approach to derive the electron characteristic energy and the strength of the electric field within sprites from ground-based optical data. The

technique uses the Maxwell-Boltzmann distribution function for collisional gases in non-relativistic motion, with few assumptions to determine these parameters.

4. Finally, the study shows the relationship between sprite morphology and the lightning charge moment change for the two most frequently observed sprite structures (carrot and column), and suggest that the carrot-shaped sprites are usually accompanied by an increase in the current strength when compared to the column-shaped sprites

1.6 Thesis structure

This thesis is structured as follows:

1. **Chapter two** presents a review of the processes that lead to thunderstorms and lightning discharges. The global and regional lightning detection networks, as well as lightning charge moment change, are also discussed in this chapter.

2. **Chapter three** discusses the methodologies and instrumentation that was used during the three-year ground-based observations of sprites in southern Africa. The results of these observations are also presented therein.

3. In **chapter four**, we use the results presented in chapter three to describe the sprites-producing thunderstorms in southern Africa. These results were first calibrated using the stars and then classified into their respective groups. We also describe the methodology used to determine the brightness of sprites, the fluxes of electrons, the characteristic electron energy and the strength of the electric field within sprites at various altitudes. The relationship between the lightning charge moment change

and the sprite's structure as well as charge moment change and sprite brightness are also presented therein.

4. **Chapter five** discusses the results and conclusions of our analysis and proposes some suggestions for future work.

Chapter 2

Thundercloud systems and lightning discharges

This chapter describes the processes that lead to the development of the convective thunderstorms and lightning discharges that precede the initiation of the transient luminous events known as sprites. Since sprite events usually occur during intense thunderstorms, we first discuss the stages in the development of convective storm and the large thundercloud systems known as the Mesoscale Convective System (MCS) in South Africa. We then discuss the processes that lead to the initiation of electrical discharges in thunderstorms, the global and regional (South Africa) lightning discharges rates as well as various lightning detection networks. Finally, we conclude the chapter by briefly describing the lightning charge moment change, which is an important metric in sprites research that is not measured by the lightning detection networks.

2.1 Stages in the life of a thunderstorm

Thundercloud systems can be described as atmospheric heat engines, with input energy from the sun and the water molecules in the atmosphere acting as the primary heat-transfer agent (Moore and Vonnegut 1977). The primary outputs from such a heat engine are the electrical discharges within the cloud, below, and in some cases, above the cloud. These include Corona, lightning and sprites, the latter being a member of the upper atmospheric optical discharges collectively known as Transient Luminous Events (TLEs) (Rakov and Uman 2003a).

Thunderclouds are generally characterised by regions of strong upward and downward air currents known as cells, which are air parcels that are electrically active, having a diameter of approximately 1.5 km (Malan 1963). A typical thundercloud consists of several cells at various stages of development. These stages include:

1. **The cumulus stage**: This stage starts with the sunlight shining on the surface of the Earth, the rays of the sun warms the ground, and the ground, in turn, warms the air layer that was in contact with it. As this layer of air gets warmer, it expands and become lighter than the surrounding air. As a result of this, it rises vertically above the colder air parcel. The updraft of air in the atmosphere can also result when winds that have different temperature converge, or where winds are blown over high terrains increasing their elevation. In either of these cases, the warm moist air

will be forced to rise above the cold air. As the warm air parcel rises, it expands further due to the decrease of the atmospheric pressure with height. Consequently, the rising air parcel cools. If it contains water (as in most cases), the moisture began to condense into very small microscopic water drops, millions of which are required to form a single raindrop (Cooray 2014). As the moist air parcels condense, they release energy (latent heat), which warms the surrounding air, making the air parcel less dense than the surrounding air. At this stage, the moist air tends to rise higher in the atmosphere, at speeds as high as 50 m/s (Cooray 2014), forming the thunderstorm clouds known as cumulonimbus, which marks the beginning of the mature stage of the thundercloud.

2. **The mature stage**: As the liquid droplet continues to rise, its moisture condenses faster, and at the same time, the temperature of the air parcel continues to decrease. When the temperature drops below 0^o C, some of the air parcel freezes, forming small ice crystals, whilst a few others remain as water even at a temperature below 0^o C, called super-cooled water droplets. When some of the small ice crystals collide with the super-cooled water droplets, they freeze together in what is known as riming. As they rim, they grow in size. A well-grown ice-crystal-super-cooled water droplet is known as graupel particles. The size of the graupel particle continues to grow to an extent that the rising air parcel finds it difficult to push upward, at that instance, they are forced to spread out horizontally giving the thundercloud its characteristic anvil shape. Consequently, the graupel begins to fall. As they fall, they collide with ice crystal and super-cooled water droplets that are moving up in the updraft.

Whilst the ice crystals become positively charged as a result of the collisions, and are transported by the up draught, the graupel becomes negatively charged and falls under gravity. The separation of charges produces enormous electrical potential within the cloud, and between the cloud and the ground, to about 3 million volts, and eventually leads to dielectric breakdown in the air. (Groenendaal 2007). During this stage, considerable strong turbulence as well as updrafts and downdrafts are observed.

3. In the final or **dissipating stage** of the thundercloud, the downdrafts dominate over the updrafts and eventually spread throughout all the cells in the storm. Since the updraft is no longer active, the storm gradually diminishes in intensity and disappears. Figure 2.1 shows the different stages of formation for a typical thunderstorm.

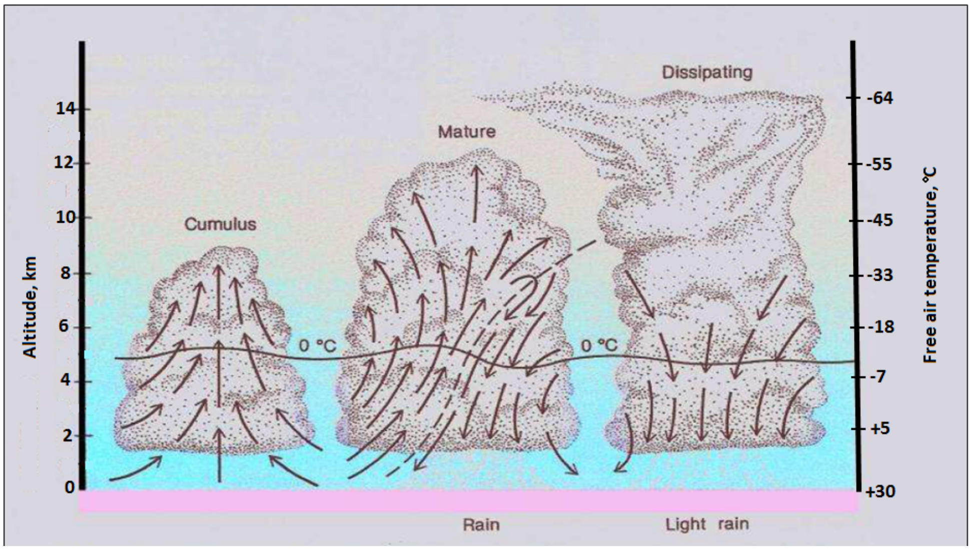

Figure 2.1: Different stages of thunderstorm formation (Adapted from (Moran and Morgan 1994)). The arrows show the direction of movement of the moist parcels of air.

A thunderstorm can be described as a short-lived (30 to 60 minutes) “air mass” storm (Moore and Vonnegut 1977), in which the single-cell updraft quickly transforms into downdrafts terminating the storm, or a longer-lived multi-cellular cluster of cells that persists for several hours, and is accompanied by a quasi-steady state and rotating updraft. The larger multi-cellular clusters with a lifetime exceeding several hours and spanning horizontally over hundreds of kilometres are collectively called Mesoscale Convective Systems (MCSs)(Lyons 2004).

2.2 Mesoscale convective systems in South Africa

Mesoscale Convective Systems (MCSs) are large convective thunderclouds (Houze 2004), which occur when smaller clouds combine to form a large cluster of storms that persists for several hours. They develop mostly over land areas (Laing and Fritsch 2004) and are usually round or linear in shape, covering hundreds of kilometres in one direction, but less than the extratropical cyclone (Houze 2004). An exceptional kind of the MCS is the Mesoscale Convective Complex (MCC), which according to Maddox (Maddox 1980) is a long-lived convective cloud system that has the characteristics shown in Table 2.1

MCCs modify the environment in which they develop (Laing and Fritsch 1993), and are of great interest to the scientific community because they lead to considerable damage through flooding, hail, tornadoes, strong wind bursts and lightning(Blamey and Reason 2012). The latter may precede Transient Luminous Events (TLEs). However, they also provide most of the rainfall that is needed for agriculture in semiarid regions like southern Africa (Blamey and Reason 2012).

Storm parameters	**MCC criteria**
Size	$A \geq 100\ 000$ km^2 $B \geq 50\ 000$ km^2
Cloud shield temperature	$A \leq 32^{o}$C $B \leq 52^{o}$C
Shape—eccentricity	≥ 0.7 at max extent (i.e., round or oval)
Initiation	When size and temperature thresholds are first met
Duration	Size and temperature definition must be met for a period ≥ 6 h
Termination	Size definitions A and B are no longer satisfied

Table 2.1: MaddoxMaddox (1980) criteria for a typical MCC. The “A” and “B” are two different sizes of the storm and their corresponding cloud shield temperature threshold. Adapted from Blamey and Reason(Blamey and Reason 2012).

Previous studies (Admirat et al. 1985; Carte 1981) have shown that large convective storms are rare in southern Africa, occurring occasionally and are not only governed by the cloud microphysical processes, diurnal heating and mesoscale forcing, but also by synoptic conditions, which determine the dynamic vertical motion and thermal environment in which they develop (Tyson 1986). A study that focused on the global distribution of thunderstorms(Zipser et al. 2006) identified the south-eastern and eastern part of southern Africa as a convective hotspot, having an average cloud-top area that is larger than the average MCCs that occur in Australia. In 2012, South African researchers(Blamey and Reason 2012) studied MCCs that occurred over southern Africa between 1998 to 2006 and found that they had an average cloud-top area of approximately 121 000 km^2, lasting between 6 to 9 hours. Their study recorded approximately 70 MCCs within the research period and found that the MCCs in southern Africa occur mostly during the austral summer (November to February), initiating in the late afternoon/evening and reaching their full extent around midnight. The observed MCS were relatively small in dimension (about 121,000 km^2) when compared with those that occur in the United States (Ashley et al. 2003) and South America (Durkee and Mote 2009), and their lifetime was also shorter than the MCCs that were observed in central Africa (Laing and Fritsch 1993). Figure 2.2 shows the origin and path of the MCCs that were tracked over southern Africa between 1998 and 2006.

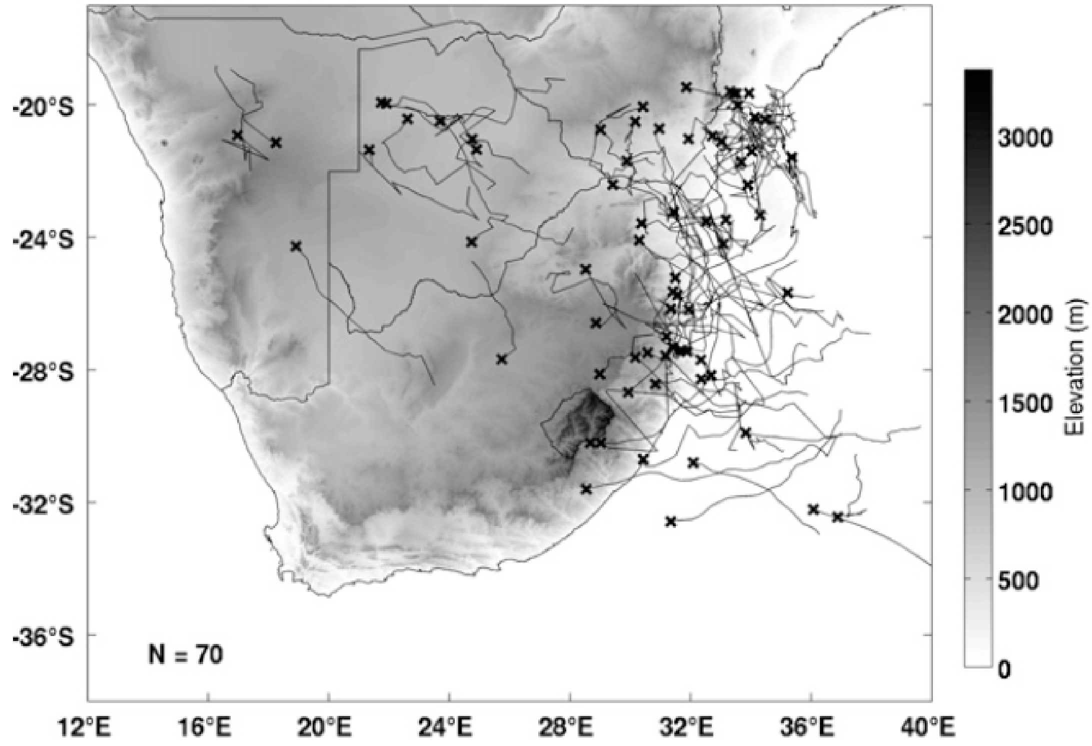

Figure 2.2: The Mesoscale Convective Complexes (MCCs) observed over southern Africa for the period of October 1998 to March 2006. For each storm, the cross shows the origin of the storm, the line shows the track. "N" is the number of MCCs that were observed during the study period (Blamey and Reason 2012).

Although the southern African MCCs have similar characteristics to those found in

Central Africa, the Americas, the Indian subcontinent and Western Pacific region (Laing and Fritsch 1993), their frequency of occurrence and size distribution are much smaller (Blamey and Reason 2012), and could account for the nature of the lightning discharges that initiate the upper atmospheric lightning phenomena (sprites) in the region.

2.3 Lightning Discharges

Within the convective cloud systems, there is charge separation between the positively charged particles and negatively charged region of equal magnitude. The positively charged particles are normally found above the negatively charged particles, forming an electric dipole as postulated by Wilson in 1916. However, a few studies(Krehbiel 1986; Lang et al. 2004) suggest that in some cases, there is also another positively charged region near the base of the storm, in which when considering the particles in this layer, describes the convective clouds as a tripole phenomenon (Williams 1989) as shown in Figure 2.3.

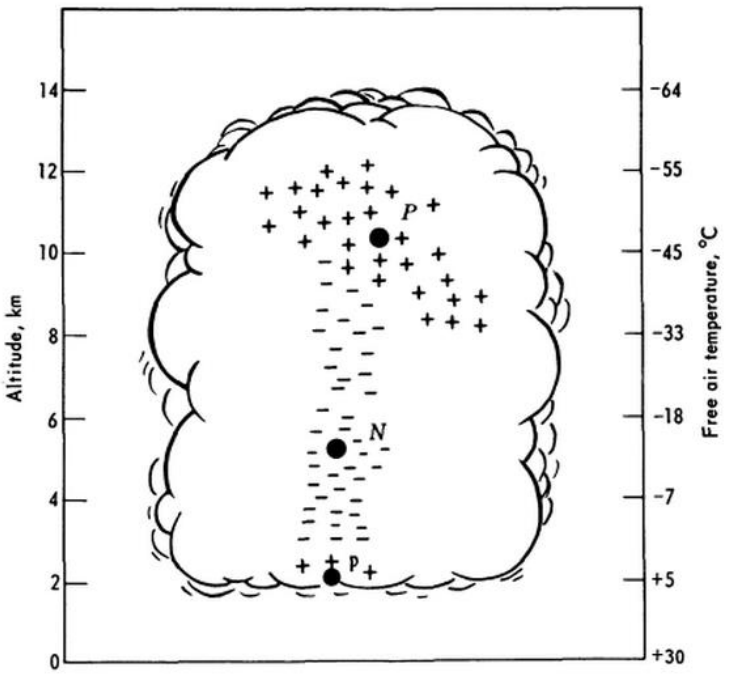

Figure 2.3: Charge structure of a typical South African convective storm (Uman 1987).

The generally accepted process for charge generation in the convective storm is the graupel/ice-crystals mechanism (Rakov and Uman 2003a), in which the large graupel particles fall under gravity and collide with the small ice crystals that are suspended in the presence of water droplets, or in updrafts. As these particles collide, they sometimes freeze or stick together in a process called riming (Rakov and Uman 2003b; Takahashi 1978). When they fall apart, the graupel becomes negatively charged whereas the ice-crystal carries a net positive charge. Jayaratne et al.Jayaratne (1984) suggest that whilst at the height above the critical value known as the reversal temperature (T$_R$, between -10^o to -20^o), the graupel/ice-crystal collision results in the graupel becoming negatively charged and the ice-crystals become positively charged, at a height below T$_R$, the graupel become positively charged and the ice-crystals become negatively charged(Rakov and

Uman 2003a). The mechanism that is responsible for the reversal of charges as shown in Figure 2.4 is still debatable (Rakov and Uman 2003a; Saunders 1993; Mansell et al. 2005).

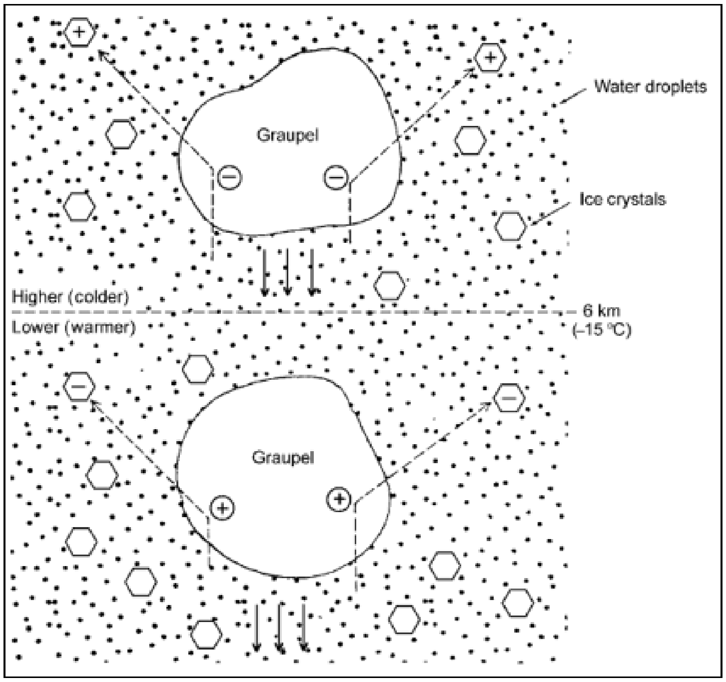

Figure 2.4: The charge reversal by the collision of the graupel and ice-crystals. The assumed charge reversal altitude is 6 km and the temperature is -15°C (Rakov and Uman 2003a).

The precipitation particles (graupel) that fall to the base of the storm with its positive charge could account for the existence of positively charge particles in the lower section of the storm (Jayaratne and Saunders 1984) as shown in Figure 2.3. As soon as the charged region of the storm attains a charge that is sufficiently large (approximately 3 × 10 ^{6} v/m, at standard atmospheric conditions) to exceed the dielectric breakdown voltage of the atmosphere, the air around it becomes a conductor, allowing the flow of charge known as the lightning discharge (flash) (Rakov and Uman 2003a).

These flashes can occur within a cloud (intra-cloud or cloud discharge), between two clouds (cloud-to-cloud discharges), between the cloud and the Earth's surface (cloud-to-ground or ground discharges) and/or between a cloud and the surrounding air (air discharge) (Uman 1987). The cloud discharges, cloud-to-cloud and air discharges are collectively referred to as intra-cloud lightning discharges (IC) (Gijben 2012). The IC lightning discharges have a duration of the order of 0.2 seconds, during which a continuous low luminous flash is observed in the cloud Uman (1987). The luminous glow usually starts from the lower negative charge region in the cloud (4 to 8 km) and propagates towards the upper positive charged (8 to 12 km) region (Cummins and Murphy 2009). They are the most dominant form of lightning flash and can be used to determine the growth rate and intensity of thunderstorms (Vaisala 2002).

The cloud-to-ground (CG) lightning discharges are those electrical discharges in the cloud that transfer charges directly to the ground. They can be divided into two different categories depending on the polarity of the charges they transfer to the ground. If they are initiated from the negatively charged region, thus transferring electrons to the ground, they are regarded as negative CG, and if they originate from the positively charged layer of the cloud, thus transferring positive charges to the ground, they are known as positive CG lightning discharges (Wood 2004).

The negative CG lightning discharges account for 90% of the total lightning discharges that strike the surface of the Earth(Rakov and Uman 2003b). They initiate as a weakly luminous pre-discharge called a stepped leader that propagates from the cloud towards the ground in a series of steps that are typically 1 μs in duration and tens of meters in length (Rakov and Uman 2003a). The essence of the leader is to form a conducting path between the charged cloud and the ground that offers the least resistance, which depends on several factors such as the shape of the electric field, dust and other particles in the atmosphere (Bhavika 2007). As the stepped leader approaches the ground, the electric field between the end of the leader and the ground begins to build up, until it exceeds the critical value. When the critical value is exceeded, one or more upward connecting leaders are developed from the ground to connect to the downward stepped leader. This marks the beginning of the attachment process, which ends as soon as the connection between the stepped leader and the upwards streamers is established. The attachment process occurs when the leaders are tens of meters above the ground. At this instance, the first return stroke occurs, which neutralizes the charges in the stepped leader, by transporting the negative charge from the leader to the ground. If there is no additional descending strokes, the lightning discharge process may terminate, in which case, the lightning flash is regarded as a single-stroke flash (Rakov and Uman 2003a). However, in most cases, a dart leader is formed, which continuously move downwards through the same channel as the first return stroke. If there are numerous descending charges in the cloud, the so-called J and K processes redistribute the remaining charges in the cloud (Uman 1987). The J-process redistributes the cloud charges from the flash origin into the negatively charged region in the cloud, within tens of milliseconds in response to a preceding return stroke. The K-process is characterised by short-lived small electric field variations at 2–20 millisecond intervals that are usually regarded as attempted dart leaders (Uman 1987). These processes continue resulting in a series of return strokes in the lightning flash, which has an average duration of tens of microseconds at 20 to 100 ms intervals (Cummins and Murphy 2009). Figure 2.5 shows the pictorial representation of the processes that lead to a negative lightning flash.

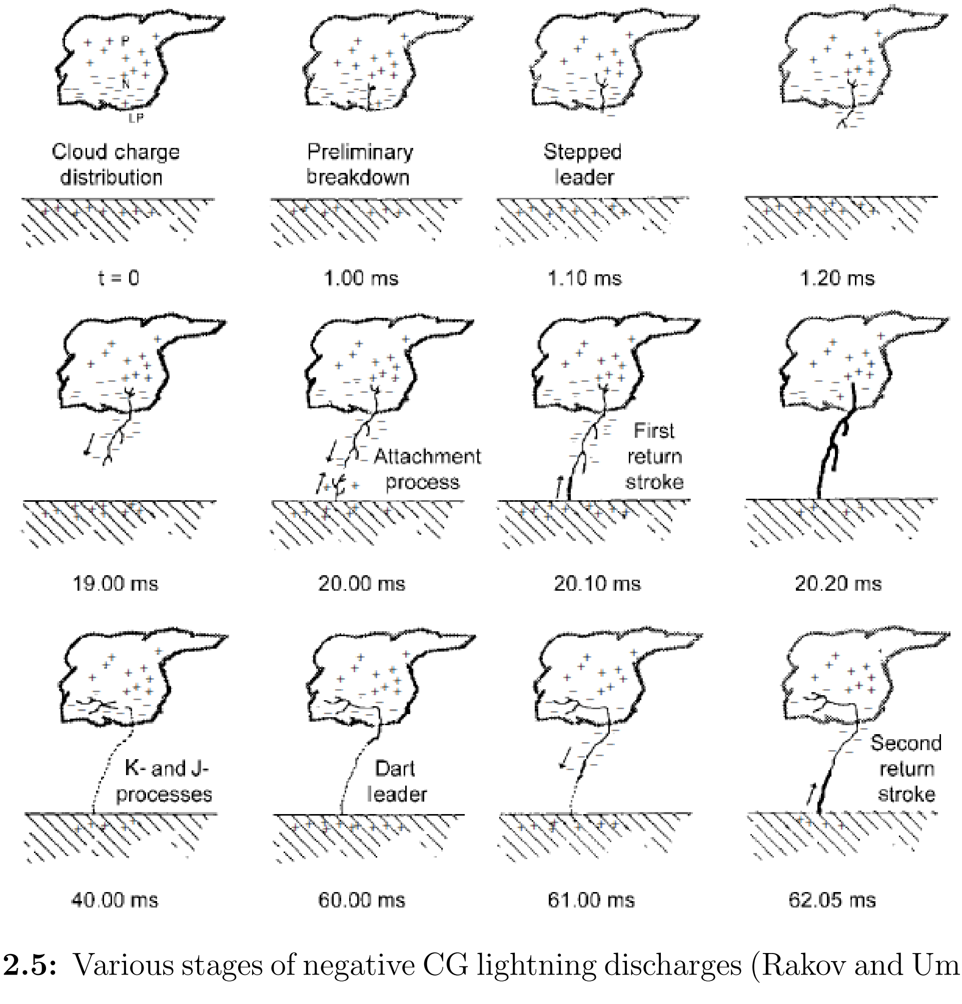

Figure 2.5: Various stages of negative CG lightning discharges (Rakov and Uman 2003b).

A similar process occurs for the positive CG lightning discharge, in which a net positive charge is lowered from the charged cloud to the ground. The +CG lightning discharges account for 10% of the total lightning flashes that strike the Earth's surface (Rakov and Uman 2003b).

2.4 Global lightning discharge rates

The rate at which lightning strokes occur across the globe differs from one geographical location to another. This was first proposed by the pioneering work of Brooks in 1925 (Brooks 1925), using "thunder day" data from several meteorological locations around the world. Brook's study suggests that there were about 1800 thunderstorms around the globe, producing approximately 100 lightning flashes per second (fl s^{-1}). However, a recent study (Mezuman et al. 2014) has shown that the global thunderstorm cells in 2012 was around 1050 per hour, varying from around 840 at 03UTC to 1150 storms at 19UTC.

This global lightning flash rate determination has been improved over the years using various systems such as satellites, radio frequency radiation detectors and ground-based very low-frequency detectors (Orville and Spencer 1979; Kotaki and Katoh 1983; Rakov and Uman 2003a; Holzworth 2018). These systems reported the global flash rate to be between 54 and 173 fl s^{-1}, depending on the season (Kotaki and Katoh 1983), and also influenced by the atmospheric circulation patterns, geographical location and ocean currents (Price 2013).

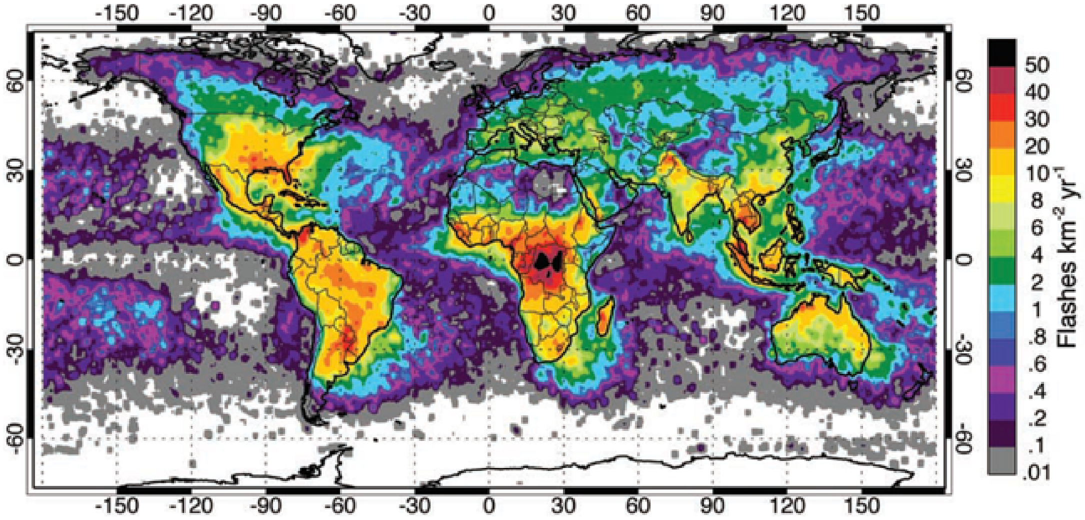

Figure 2.6: The global frequency and lightning distribution as observed from space using the Optical Tranisent Detector (OTD) on the MicroLab-1 satellite (Christian et al. 2003).

A study (Christian et al. 2003) of global lightning discharges, using the Optical Transient Detector (OTD) on the MicroLab-1 satellite suggests that the total average global flash rate for both intracloud and cloud-to-ground lightning discharges is around 44 fl s^{-1}, with an uncertainty of ± 5 fl s^{-1}. These authors suggest that approximately 78% of these lightning flashes occur in the tropics, where there are high temperatures and a higher concentration of water vapour compared to the polar regions. Their study also shows that most of the lightning flashes occur over land, as shown in Figure 2.6, which results from the intense thermal heating of the land, leading to atmospheric instability that eventually result in strong convention.

Christian et al. (2003) identified the Congo basin in Africa and the Amazon basin in South America as the two lightning hotspots in the world, having a ground flash density that exceeds 50 km^{-2} per year and suggests that lightning activities occur throughout the year in these regions. In South Africa, their study shows that there are approximately 23 flashes km^{-2} per year, which is comparable to the flashes that occur in some parts of North and South America, Northern Australia and Asia, thereby suggesting that South Africa is also one of the lightning-rich region in the world.

2.4.1 Lightning discharges in South Africa

The lightning climatology of South Africa was initially studied by Gill (2008), to determine the lightning ground flash density, flash median peak current and flash multiplicity across the nation. The study was based on a year of lightning flash data from the South African Lightning Detection Network (SALDN), which consists of 23 sensors that are located in different parts of the country. Gill's work was later updated, using five-year lightning flash data, from 2006 to 2010 (Gijben 2012) to ascertain the lightning-intensive risk regions, the positive lightning strike risk area and the total lightning risk map in the region. These studies suggest that the general flash density across the nation decreases from the east to west as shown in Figure 2.7, with little or no lightning activity in the western part of the country, which was proposed to be caused by the cold Benguela current that prevents atmospheric convection in that region (Collier et al. 2006).

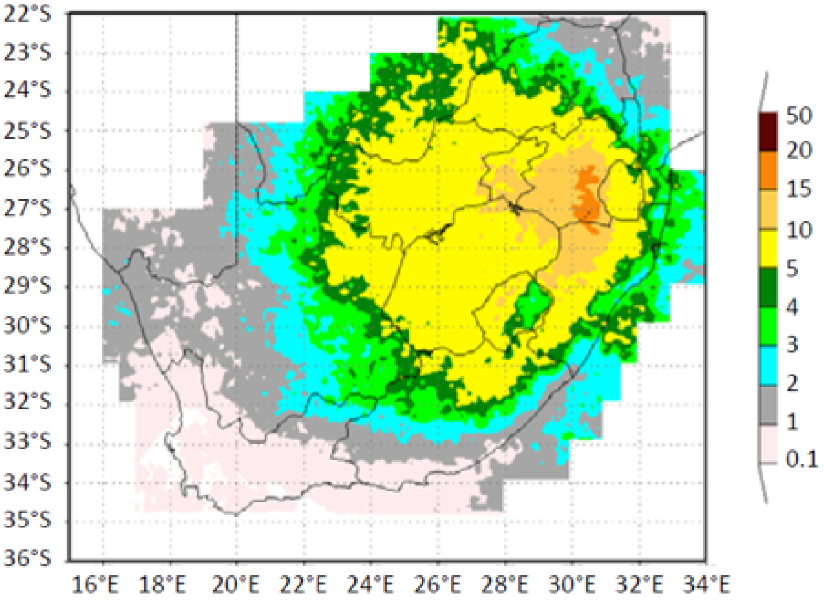

Figure 2.7: Map showing the 5-year total ground lightning flashes per square km in South Africa from 2006 to 2011. Source: South Africa Weather Service. Cited from Gijben (2012).

Whilst the eastern escarpment has the highest lightning flash density (between 15 -20 flashes km^{-2} per year (Gill 2008), the region has also been identified to have the highest flash multiplicity, which is influenced by the high-pressure systems in the Indian Ocean and the warm Agulhas current that flows down the east coast of Africa (Collier et al. 2006). The lightning flash density in the country also varies from one season to another, having its peak in the summer season (November to February). The percentage of positive strokes tends to be higher during the winter season whereas, in the spring and early summer, most of the recorded strokes had a negative polarity (Gijben 2012). Figure 2.8 shows the seasonal ground flash variations within South Africa.

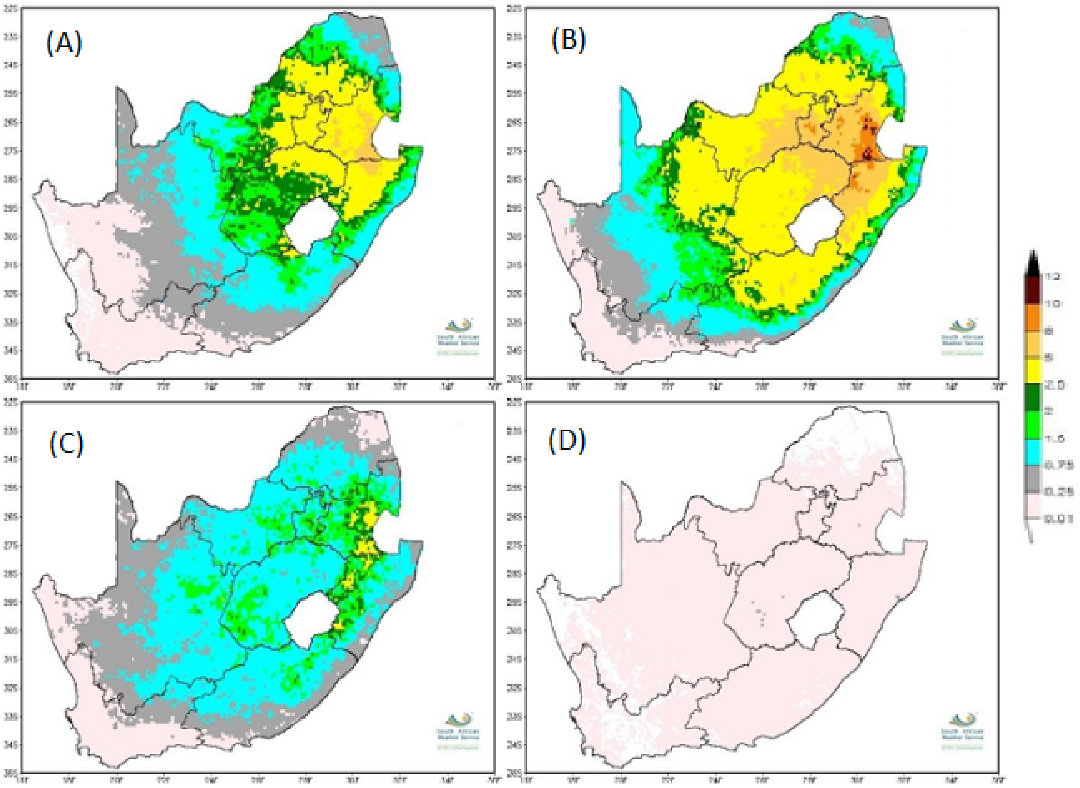

Figure 2.8: The seasonal total ground lightning flash densities over South Africa from 2006 to 2010. (A) Spring (September, October, November), (B) Summer (December, January, February), (C)Autumn (March, April, May), (D) Winter (June, July, August) (Source: South African Weather Service). The white area within the plot is the Kingdom of Lesotho.

2.5 Ground-based lightning detection networks

The ground-based lightning detection networks use various techniques and sensors that operate within the frequency range of 1 Hz to near 300 MHz (Rakov and Uman 2003a) to detect and locate accurately the electromagnetic radiation that is emitted by a lightning flash. These sensors can be localised in a region or span across multiple nations, as illustrated by the South African Lightning Detection Network and the World-Wide Lightning Locations Networks, respectively. The accuracy of these networks to detect the position and time of arrival of a lightning stroke depends on the number of ground sensors that are utilized in the detection of the stroke.

2.5.1 World-Wide Lightning Location Network

The World-Wide Lightning Location Network (WWLLN) was developed to provide low cost, real-time global lightning coverage, especially over the oceans and in remote areas, where local or regional lightning detection networks are not available (Burgesser 2017). The network consists of about 70 sensors that operate in the frequency range of 3 to 30 kHz (Bui et al. 2015). These sensors are positioned around the globe to detect the very low frequency (VLF) signals of the lightning discharges called *sferics*. The propagation of these very long wavelength signals allows lightning strokes to be detected in real-time at up to 10,000 km away from the receiver, with a 10 km accuracy (Lay et al. 2004).

The WWLLN network initially operated in a simple mode setting, by sending the trigger times of the lightning stroke on each station to a central processing unit, but was later upgraded to use time of group arrival (TOGA) techniques, to accurately locate the *sferics* (Dowden et al. 2002; Rodger et al. 2004). The use of TOGA techniques requires at least 5 sensors within the network to detect a discharge that could be several thousands of kilometres away from the sensors. The geographical location of these sensors is important because *sferics* that are detected by several sensors are much more accurately located than the one that is only detected by few sensors (Holzworth 2018). This implies that for the effective operation of the network, additional sensors are needed to cover the whole globe. However, due to the limited number of the sensors around the globe, the detection efficiency of the network for *sferics* with an amplitude greater than 30 kA is approximately 30% (Holzworth 2018). Nevertheless, the network has successfully been used for various lightning-related studies by several investigators (e.g. Shevtsov et al. (2016), Virts et al. (2015), Soula et al. (2016)).

Whilst a few of these researchers (Abarca et al. 2010) that used the lightning stroke data from the WWLLN suggest that, aside from the limited number of sensors that make up the system, the changes in the ionosphere could also affect the detection efficiency of the network, most especially during sunrise and sunset, other researchers (Rudlosky and Shea 2013; Hutchins et al. 2012) that compared the efficiency of the network to a space-based lightning detection system (LIS), suggest that the efficiency of the network improved over time, probably during their study period and over their area of interest. They also suggest that the improvement of the efficiency of the WWLLN results from the addition of new stations as well as the upgrading of the lightning detection algorithms (Burgesser 2017). Figure 2.9 shows the location of the WWLLN sensors around the globe.

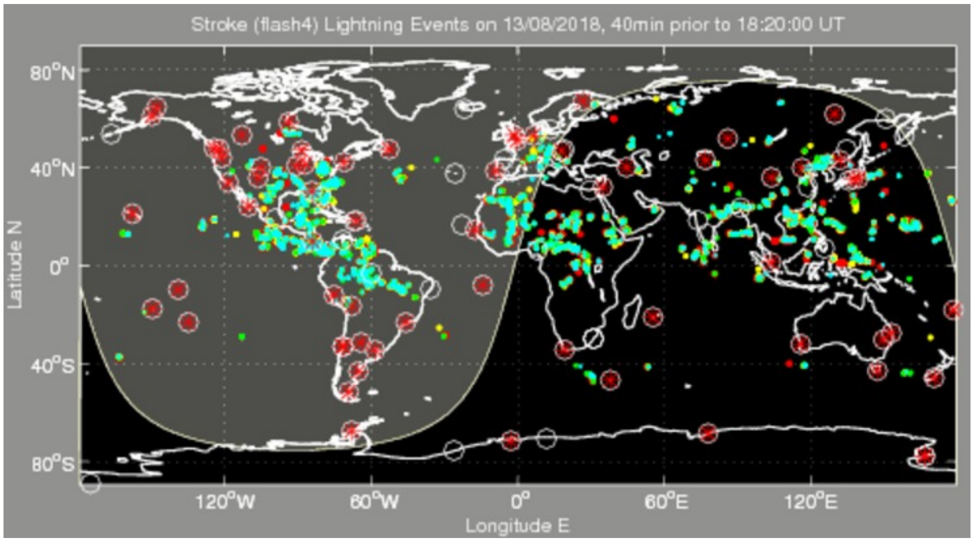

Figure 2.9: The lightning events on the globe as detected by the WWLLN. The red asterisks in the white circles are the active sensors. The active lightning stroke locations are shown as coloured dots (cyan, green, yellow and red) - cyan indicates the most recent stroke (less than 10 minutes), red – the oldest stroke (30 to 40 minutes earlier)(Holzworth 2018).

2.5.2 Earth Network Total Lightning Network

The Earth Network Total Lightning Network (ENTLN) was originally known as the WeatherBug Total Lightning Network (WTLN) (Bui et al. 2015). The network is currently managed by Earth Network and consists of over 1500 lightning detection sensors that are located in more than 40 countries around the globe (Zhu et al. 2017). These sensors are a wide-band system that operates at a frequency range from 1 Hz to 12 MHz, which enables it to detect not only the strong CG lightning discharges but also the weak Intra Cloud discharges.

The system consists of an antenna, a GPS receiver, a GPS-based timing circuit with a digital signal processor (DSP), onboard storage and an internet connectivity port (ENT). When a lightning discharge occurs, the electromagnetic energy from the discharge is emitted in all directions. Depending on the location of the stroke, the electric waveform signal and the amplitude of the stroke are recorded and sent to the central server through the internet(ENT). The DSP on the server is then used to ensure high-quality detection and to eliminate false detection. The system uses time-of-arrival techniques, and sophisticated algorithms to determine the position (latitude and longitude), the altitude, polarity (positive or negative) and the type of the discharge. For instance, the system identifies CG lightning discharges, if they contain at least one return stroke or IC lightning discharge if there was no return stroke (Bui et al. 2015; Zhu et al. 2017). However, the IC classification may also include other types of non-CG lightning discharges such as narrow bipolar events and k-changes (ENT). Figure 2.10 shows the distributions of the IC and CG lightning stroke that was detected by the ENTLN during the 2017 sprite campaign presented later in this thesis.

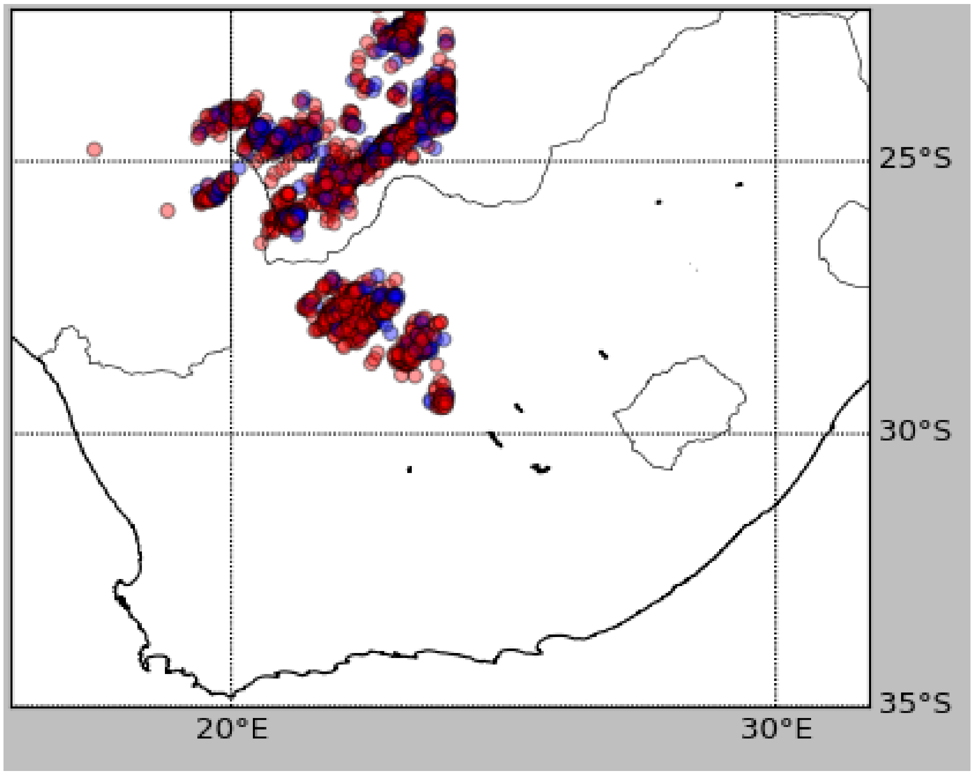

Figure 2.10: The IC and CG lightning strokes detected on 24 January 2017. The red and blue circles represent the IC and CG lightning strokes respectively.

The network was specifically established to detect both the weak IC and large CG lightning discharges and has the potential to improve severe weather warning times over all other available technologies (Hutchins et al. 2013). The detection efficiency (DE) of the ENTLN varies depending on the sensor location density in each geographical location. For instance, in 2014, the network had a DE of 85% - 100 % in North, Central and South America, as well as in Europe and Australia. In the same year, the network also had between 10% - 63% DE in North Africa and Central Asia. In the Pacific Ocean, the Atlantic Ocean and north Indian Ocean, the estimated DE ranges from 50% to 99% (Bui et al. 2015). In South Africa, where the network had over 17 sensors that are located mostly in the eastern and southeastern part of the country, the DE of the network is between 60% to 70% (ENT).

Figure 2.11(left) shows the location of the ENTLN sensors in South Africa. Figure 2.11(right) shows the global detection efficiency of this network (ENT).

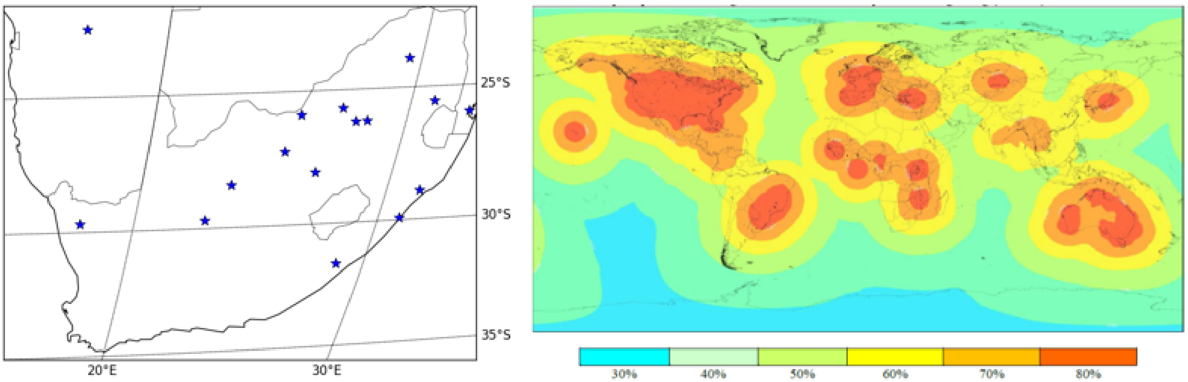

Figure 2.11: (Left) Showing the location of the Earth Network Total Lightning Network (ENTLN) sensors in South Africa. (Right) The global detection efficiency of ENTLN (ENT).

2.5.3 South African Lightning Detection Network

The South African Lightning Detection Network (SALDN) is managed by the South African Weather Service (SAWS). The network currently has 22 Vaisala lightning detection sensors installed in South Africa, and an additional sensor in Swaziland, making it a 23-sensor network. These sensors operate at a very low frequency to detect the electromagnetic pulses that are emitted by a lightning flash. These flashes propagate as both low-frequency waves through the atmosphere (skywaves) as well as along the ground as ground waves (Gijben 2012). The geographical location of these sensors as shown in Figure 2.12 ensures that the network has a predicted lightning stroke detection efficiency of 90% and location accuracy of 500m in South Africa (Groenendaal 2007). However, these values have not been verified by field experiments (Gijben 2012).

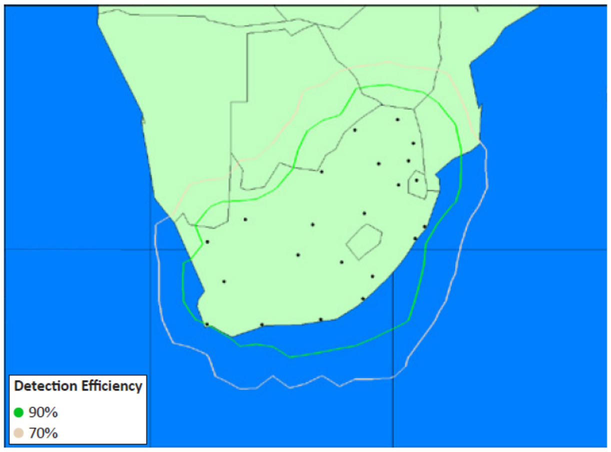

Figure 2.12: The approximate location of the SALDN sensors and the predicted detection efficiency of the network(Gijben 2012).

The SALDN sensors determine the position and polarity of lightning strokes using both magnetic direction finding (MDF) and time-of-group-arrival (TOGA) techniques. The MDF method uses two orthogonal loop antennas that are oriented in the North-South and East-West planes to detect the magnetic fields from the lightning discharge. The radiated magnetic field induces currents in the loops, which are used to determine the direction of the strokes. The direction of the stroke is then sent to a position analyser, which triangulates the information to determine the precise position of the lightning stroke (SAW). TOGA uses an array of four antennas to determine the possible location of a stroke based on the arrival time of the stroke signal at the antennas. By combining these techniques, the SALDN is able to determine the position and time of each lightning stroke.

2.6 Lightning Charge Moment Change

The lightning Charge Moment Change (CMC) parameter is an important metric that is not measured by the lightning detection networks (Wilson 1956; Huang et al. 1999; Hu 2002). The lightning charge moment change is defined as the multiplication of the charge and the altitude from which this charge is lowered to the ground.

Previous studies (Boccippio et al. 1995; Lyons 1996) proposed that the peak currents of lightning discharges could be used to determine the occurrence of sprites during intense storms. These studies suggest that, whilst the average peak current of the lightning discharges that initiate sprites is greater than 30 kA, the very large peak currents (> 90 kA) are usually associated with elves, and that the size of the sprites increases with higher peak current. However, Huang et al. (1999) have shown that the total charge transfer of the lightning discharge is a better indicator of sprite occurrence and that little correlation exists between the LDN peak current and the total charge transfer for positive cloud-to-ground discharges.

Chapter 3

Sprite observations in South Africa

In 1937, anecdotal[1] accounts of sprites were published by Malan (1937), a South African atmospheric researcher, who reported seeing an unusual form of lightning over thunderstorms in Johannesburg, at an altitude of approximately 50 km. According to this researcher, there was a huge cloud at a distance and within an hour and a half, a long and weak streamer of reddish hue appeared about ten times in the upper cloud with a weak illumination of the same cloud occurring simultaneously (Malan 1937). He assumed that the weak illumination was due to cloud-to-ground lightning discharges behind the hills.

Although sprites occur over active thunderstorms on a global scale, they are rarely reported because they are very brief and most people tend to find shelter during an

---

[1] As with all anecdotal accounts, one may dispute whether or not Malan actually did see sprites, but we believe he did, because we know sprites can be visible to the naked eye, and Malan was an experienced observer of atmospheric phenomena

intense thunderstorm. Prior to this study, sprites had not been recorded over southern Africa using ground-based systems. It is important to study such transient atmospheric phenomena in order to better understand the interconnected processes that govern our natural environment.

3.1 Ground-based observations of sprites

In 2014, the South African National Space Agency (SANSA) proposed to search for these elusive upper atmospheric phenomena (Campbell 2014) as a way to encourage studies of the electric phenomena in the middle atmosphere. Prior to the proposal, this region of the atmosphere had not been extensively studied in Africa. The proposal was approved, and in the summer of 2015/2016, the first ground-based observations of sprite events, which were tagged as the "AfriSprite Campaign", were conducted at the South African Astronomical Observatory (SAAO) in Sutherland, northern Cape (Nnadih et al. 2018).

The SAAO is an ideal location for these observations because of its clear, dark skies, and high altitude of approximately 1798m above sea level. This location assisted in observing a significant portion of the lightning and sprites-rich zone over land and over the Indian Ocean at a distance. During these observations, sprites were observed as far as Bloemfontein and Lesotho towards both the north and the north east and in Port Elizabeth towards the east(approximately 700 km). The success of these observations paved the way for more detailed follow-up observations of sprites and a contract between the South African National Space Agency (SANSA) and the South African Astronomical Observatory (SAAO) to host the Optical Space Research (OSR) Laboratory at SAAO, which has been used to further studies of sprites in South Africa.

Subsequent to the AfriSprite Campaign, follow-up observations of sprites at multiple wavelengths were conducted at the SAAO, using the OSR facility. During these observations, it was concluded that there was a need to surveil the thunderstorms at a closer range. This decision, made in an attempt to maximize the chances of recording the blue emissions of sprites, was taken because on 18 out of 23 nights of the observation period, the thunderstorms were approximately 800 km away from SAAO. Since the blue emissions from sprites have a shorter wavelength than the red emissions, and are easily absorbed/scattered by the atmosphere, observing thunderstorms that are closer to the camera location could increase the chances of recording the blue emissions from sprites.

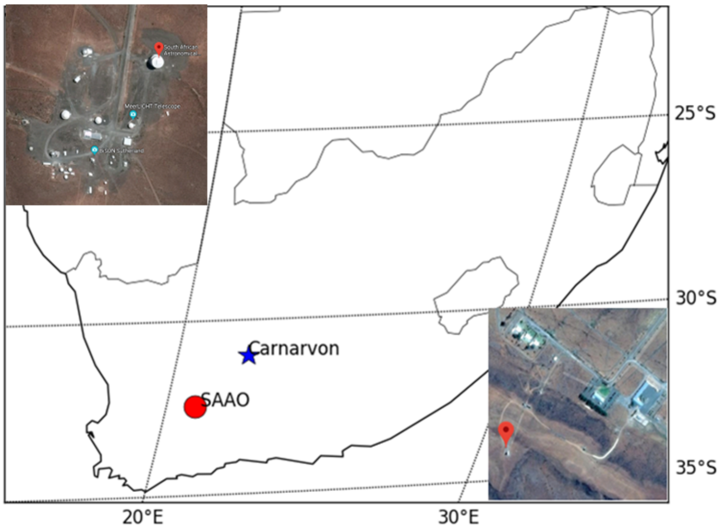

Figure 3.1: The observation sites. The red circle is the position of the South African Astronomical Observatory (SAAO) (upper left). The blue asterisk is location of Klerefontein, Carnarvon (lower right).

There were a few other alternative sites that could have been used for these observations, but whilst searching for the ideal location for sprite observations, factors such as the safety of the instruments and the observers, as well as internet access for real-time tracking of the thunderstorms, the Klerefontein farm at Carnarvon in the northern Cape province of South Africa (21.9801 E, 30.9721 S), was selected as an alternative location for sprites observation. The farm is located very near to the South African Square Kilometre Array (SA-SKA), which is known to be in a lightning-rich region of South Africa (Collier et al. 2006) and is situated to the North-East of the SAAO. The Klerefontein farm lies 192 km away from SAAO and approximately 500 km to the active thunderstorm region in South Africa. Although this site is much lower in altitude (1309 m) than SAAO, sprite events that could not been seen from SAAO were recorded from this site.

3.2 Instrumentation

Sprites were observed using a Watec 910 Hx camera and an iXon Electron Multiplying CCD camera (Figure 3.2). During these observations, the cameras were all mounted on a single tripod mount so that they could all be pointed in the same direction at the same time.

a) Watec 910Hx camera

In our observations, we used Watec 910Hx cameras to record sprites in white light and in filtered red and blue light (see below). The Watec 910Hx is a commercial monochromatic Charge Coupled Device (CCD) TV camera, which has been used extensively in sprites research around the world, such as the EuroSprite campaigns (Neubert et al. 2001; Bor 2013). These CCD cameras are low-light cameras with a minimum illumination of 5.1×10^{-6} lux and a 0.5 inch interline image sensor, which records video frames with 8-bit resolution using a fixed nonlinear gain.

During the observations the CCD detector arrays of 752(H)× 582 (V) effective pixels were oriented with the long axis of the detector in the horizontal plane. These cameras were fitted with an 8mm f/1.4 lens giving a FOV of $43^o \times 33^o$ and were operated at a frame rate of 25 Hz. Nitrogen filters were also attached to these cameras to enhance their signal-to-noise Ratio (SNR) at specific wavelengths. These filters are standard nitrogen emission filters (Cotton 2010). Their spectral bandpass of 635-675 nm for the red and 426-440 nm for the blue covers the emission spectrum of sprites (Red: neutral N_2(1P) at 640 nm; Blue: ionized (N_2^+(1N)at 427.8nm) as suggested by Yaniv et al. (2014). They enabled the observations of sprite events simultaneously at multiple wavelengths.

Figure 3.2: (Left) The Watec 910Hx camera (Astroshop 2018) and (Right) iXon Andor EMCCD camera (Technology 2018).

The cameras were connected through a video digitizer (Pinnacle Dazzle) to a computer that ran the Sonotaco image capture software version 2 (`http://sonotaco.com/soft/e_index.html`) developed by the Japanese company Sonotaco to study Unidentified Flying Objects, but which was later adapted for the study of meteor showers and Transient Luminous Events (e.g. sprites), and has been used extensively by several sprites observers around the world (Sato et al. 2015; Bor et al. 2009; Fullekrug et al. 2013). The software has a triggering mechanism that allows it to read out the incoming image frames on the CCD chip continuously, but only stores the frames with image intensity that exceed the detection threshold set by the observer. This technique greatly reduced the data rate and ensured that the recorded data contained the required events. The triggered frames were time-stamped by the software, then digitised, and stored for subsequent analysis. To ensure the accuracy of the timing system in the software, the computers were connected to the Network Timing Protocol (NTP) server of the host facility (SAAO or SA-SKA). Table 3.1 shows the camera settings that were used during this study.

Camera Parameter	**Setting used during the observations**	**Rationale**
Shutter speed AGC–Auto Gain Control BLC–Black Light Compensation	1/50/s OFF: Set Manual to 41dB OFF	These were the preferred settings during the observations. The AGC was set to OFF position, then manually set to prevent the camera from automatically adjusting the image brightness. The BLC was set to OFF based on the recommendation from the user manual (Stewart 2015).
Sharpness Gamma	10 0.45	These were the recommended settings from the user manual of the camera (Stewart 2015).
Wide Dynamic Range Motion	Not used OFF	These were the recommended settings from the camera user manual (Stewart 2015) for observations of transient events.

Table 3.1: Watec 910Hx camera settings used during the observations.

b) iXon EMCCD Camera

The iXon EMCCD camera is a back-illuminated, single–photon counting camera that amplifies weak signals to a signal level that can be detected by the CCD camera. It has a 30° FOV, depending on the lens and an image area of 25.4mm × 25.4 mm. The camera has a variable readout rate of up to 10 MHz, which provides heightened application flexibility and can be cooled down to -100 degrees Celsius during operation to reduce thermal noise (Andor-Technology 2018). The camera has a quantum efficiency (QE) of $\sim$ 75 % at a wavelength (Andor-Technology 2018) of 427.8 nm that corresponds to the wavelength of the blue emissions from sprites and has been used successfully to study aurorae (Michell et al. 2014), which produce $N2^+$ emissions similar to those of sprites.

During the observations reported in this study, the camera was cooled to -50 degrees Celsius and operated at 256 × 256-pixel mode, with a 2× 2 internal binning that allowed an acceptable trade-off between temporal and spatial resolution. The camera was fitted with a 50 mm/f0.85 lens and a 426-440 nm nitrogen filter to observe the 427.8 nm emissions from sprites and was connected to a computer that ran the Andor Solis software, an image capture and analysis software that has been used in a wide range of scientific fields(Technology 2018). The software allowed us to control certain features on the camera, which include the pixel readout rate, the horizontal and vertical binning, pre-amplifier settings and the electron multiplying gain.

3.3 Camera pointing angle

Previous observations of sprites by various researchers suggest that sprites usually occur above active thunderstorms at altitudes of around 40–85 km (Lyons 1994; Barrington-Leigh 2001) and are accompanied by lightning discharges within and below the thunderstorm. Hence, for successful observations of sprites using ground-based systems, the camera needs to be pointed in the right direction, and slightly above the storm, as shown in Figure 3.3. This is to avoid any false detection from lightning strikes below the thunderstorm.

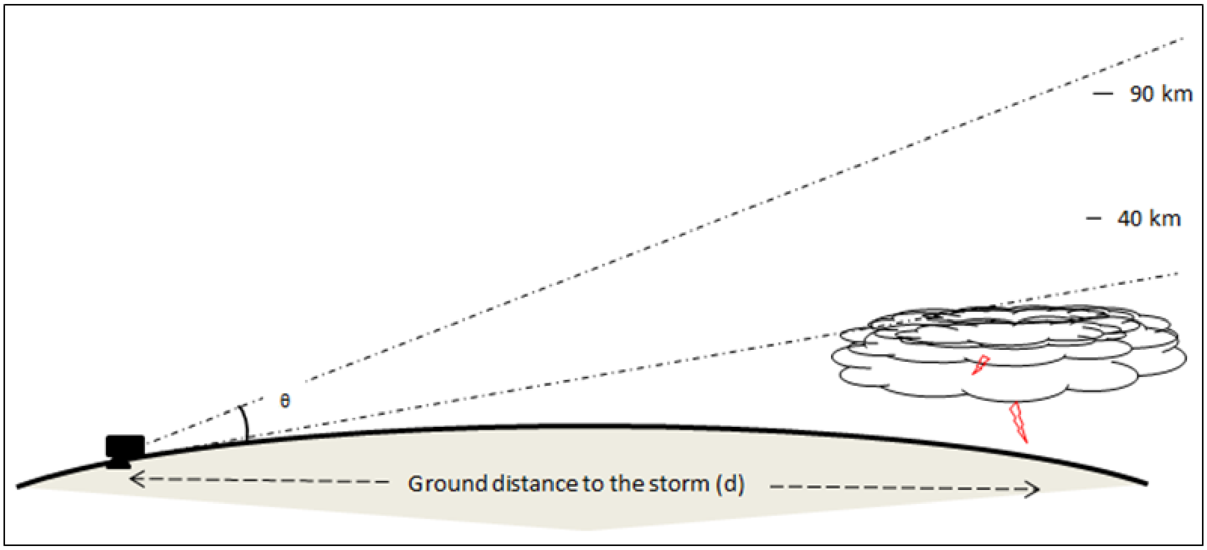

Figure 3.3: The camera pointing geometry.

The camera elevation angle (θ) used during these observations was determined from equation (3.1),which relates the pointing elevation angle for the camera to the ground distance of sprites and their altitudes using spherical geometry (Kosch et al. 2009).

$$\tan(90-\theta) = \frac{(h+r)\sin[\frac{d}{r}]}{(h+r)\cos[\frac{d}{r}]-r} \tag{3.1}$$

where θ is the observing elevation angle,

h = the assumed altitude above ground(km),

r = 6370 km is the radius of the Earth, and

d = the distance of the storm from the camera (km)

Hence, for h = 100 km (lower boundary of the night-time ionosphere):

d = 100 km $\Rightarrow \theta = 44.3\,^\circ$

d = 200 km $\Rightarrow \theta = 25.5\,^\circ$

d = 300 km $\Rightarrow \theta = 17.0\,^\circ$

d = 400 km $\Rightarrow \theta = 12.1\,^\circ$

During each night of observations, the ground distance between the camera and the storm was measured using the distance measuring tool on Google Earth software and the camera pointing elevation was adjusted accordingly. However, since most of the thunderstorms that were observed during this study occurred beyond 400 km from the observation point, an elevation angle of $15\,^\circ$ was used for most of the nights to avoid pointing the bottom edge of the camera's 33° vertical field of view below the horizon.

3.4 Observation techniques

The above instruments were set up at either SAAO or Klerefontein (Figure 3.1) and operated during the lightning-rich period in southern Africa (December- February)(Collier et al. 2006). When to operate the camera and where to point it was determined in real-time by observing storm activities over southern Africa using the Meteosat infrared imagery. Meteosat is a series of geostationary meteorological satellites that are operated by EUMETSAT and the European Space Agency. These organisations provide near-real-time weather forecast and severe weather warnings over Europe, Africa and the Indian Ocean (Eumetsat 2016). The primary role of these satellites is to detect and forecast high-impact weather phenomena, such as convective thunderstorms, from the initial stage to the matured thunderstorm.

During these observations, the imagery of the cumulonimbus thunderclouds was downloaded in real-time from the secured server of the Climate System Analysis Group (CSAG) of the University of Cape Town, South Africa. These images were regularly updated every 15 minutes on this server and were used to make decisions regarding the direction in which to point the camera during these observations. The infrared band of the imagery was chosen to detect the coldest part of the cloud because the colder the cloud,the greater the convection, and therefore the more likely it was to produce large lightning discharges and sprite events. The images were also colour-coded (Figure 3.4(right)) to determine the coldest spot in order to point the camera in that direction.

This was complemented by the lightning forecast data from SAT24 (`https://en.sat24.com/en/za?type=infrapolair&type=infrapolair`).

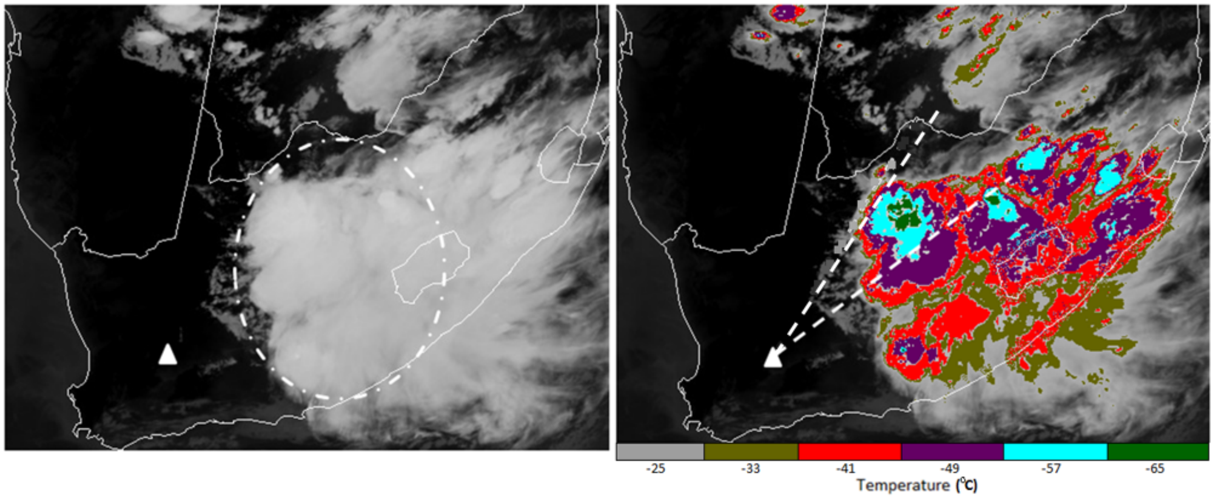

Figure 3.4: (Left)MeteoSat imagery showing the storm observed on 11th January 2016. (Right) The delineated structure of that storm based on its temperature values. The triangle on both images shows the observation point; the dotted lines show the camera's field of view during the observation, which was approximately 43°.

SAT24 is a company that uses the imagery from geostationary satellites to monitor precipitation and cloud cover over the entire continent. The website forecasts rain, temperature, wind and lightning discharges for any selected region. During the observations, this online tool was used to forecast lightning discharges over a seven-day interval in our observation area. Since the MeteoSat imagery is a nowcasting weather observational tool, the lightning forecast from the SAT24 website was mostly used during the day to prepare each night's observations.

3.5 Observation campaigns

The sprites observation campaigns reported in this thesis were held during the three consecutive austral summers of 2015/2016, 2016/2017 and 2017/2018. In each season, there was a specific observational goal and the objectives for each of these observing seasons were set accordingly. During the first observing season, the objective of the campaign was to record sprites in unfiltered light using a single camera. These observations were held from 10–16 December 2015, 5–13 January, and 2–10 February 2016. These dates were selected because they were within the lightning-rich period (December-February) in South Africa (Collier et al. 2006), the illumination from the moon was less than 5%, which was ideal for observations, and the lightning prediction from the weather service (SAT24) predicted potential lightning strikes within the search area.

The second phase of this experiment was conducted from 23rd January–3rd February and 21st February–2nd March of 2017. The objective of this campaign was to observe sprites at different wavelengths simultaneously. In order to achieve this, three different cameras were used for the observations. These cameras were filtered to observe sprites at different wavelengths that correspond to the emission lines of nitrogen. Whilst two of these cameras observed the red and blue emissions from sprites, the third camera was used without a filter to observe the emissions from sprites at all wavelengths within the visible region of the spectrum. All three cameras were mounted on a tripod and co-aligned to ensure that they were all pointing to the same part of the night sky. The essence of using an unfiltered (i.e. white-light) camera was to compare the imagery that was acquired by this instrument to those that were recorded by the filtered cameras. This allowed the comparison of the structures of each event at a specific wavelength band and to retrieve the spectral information at different altitudes within the sprite events. Although sprites were recorded during this period, the low sensitivity of the blue filtered camera limited the effort of simultaneously recording the red and blue emissions from sprites. Thus, a more sensitive optical imager was recommended for further observations.

The third and last phase of sprites observations during this study was conducted from the 16th January to the 8th February 2018. The objective of this campaign was also to observe sprite events at different wavelengths using multiple cameras simultaneously. During this period, a more sensitive optical instrument (iXon EMCCD) was used for these observations. This instrument is an electron multiplying CCD camera that amplifies weak signals above the noise floor of the detector. The aim of using this camera was to amplify the signals from the blue portion of the sprite's emission spectrum, which were not previously recorded by the Watec 910Hx camera.

3.6 Sprite observations

Studies have shown that sprites have emissions that correspond to different wavelengths within the visible region of the electromagnetic (EM) spectrum. For instance, whilst Mende et al. (1995) and Hampton et al. (1996) observed the red emissions, which correspond to the 640 nm emission band in the nitrogen spectrum, Armstrong et al. (1998), Suszcynsky et al. (1998) and Heavner et al. (2010) observed the blue and near UV emissions, corresponding to the 427.8 nm and 340 nm bond of nitrogen, respectively. These studies used non-imaging instruments (photometers) to study different sets of sprite events and were not able to estimate the fluxes of the electrons associated with these events at various altitudes of their emissions. The observations of sprites that are reported in this study were carried out at specific wavelength ranges (visible (400–750 nm), red (635–675 nm), blue (426–440)) that correspond to most of the emissions that are found in sprites.

3.6.1 Single-wavelength observations

The single–wavelength observations of sprite events involve the use a camera that operates within the visible region of the spectrum (Figure 3.5) to record sprite events. This methodology was effectively used to observe sprites during the southern summer of 2015/2016 at the SAAO (Nnadih et al. 2018), Sutherland. The objectives of these observations were to record a series of sprites over land and/or ocean using a single camera. The Watec camera was fitted with a wide field of view (8.0mm f1.4) lens to observe as many sprite events as possible within its view and was operated at 80 ms temporal resolution to increase its signal-to-noise ratio. During this observation, the orientation of the camera was initially set to azimuth $\sim 81^\circ$ and elevation 15°, which was later adjusted as the storm drifted from one active region to another.

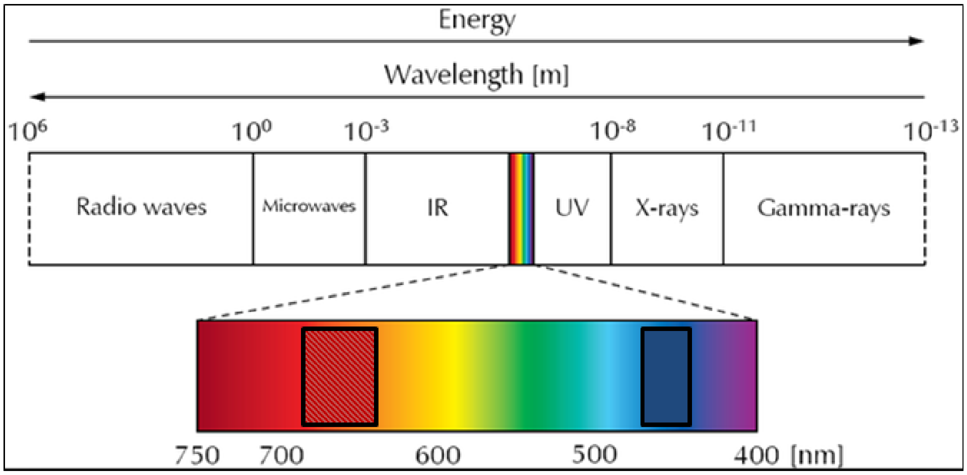

Figure 3.5: The electromagnetic spectrum. The shaded portions of the visible spectrum shows the wavelength ranges of the camera's filters.

.

The instrument used for our observations was set up in the Automatic Photoelectric Telescope (APT) Dome at the SAAO. The dome has a diameter of 4 meters, a concrete pier that is 2.7 meters above the ground level and a shutter that slides in an upward direction along the length of the dome slit, which allows it to open up to 15 ° past the zenith (Martinez et al. 2002).

During the period of these observations, the APT was not in use for astronomical studies. Hence, its dome was effectively used for sprites research. The sprites camera was mounted on the concrete floor as shown in Figure 3.6 and connected to the computer that was set up in the control room below the pier. The shutter of the dome was opened to allow a good view of a thunderstorm. The reason for using the telescope dome was to protect the observer and the instruments from the harsh weather conditions in the Karoo Desert, where the SAAO is situated.

Figure 3.6: Observation camera set-up.

On the night of 11 January 2016, a warm frontal wave passing over South Africa caused the development of active cumulonimbus thunderclouds over the North-Eastern Cape (Figure 3.4). This storm was ∼370 km away from the observing point (SAAO), and covered over 2000 square kilometres. The temperature of different sections of the storm, which typically varies from less than -25°C to -65°C was determined by a computer algorithm that uses the conversion factor of the Meteosat imagery (see Appendix A1) to determine the corresponding temperature values. This was effectively used to determine where to point the camera. During these observations, 54 video clips containing sprite events were recorded between 18:30 and 21:30 UTC. These video clips were ~ 2 seconds long, containing one or more sprite events. In total, over 90 sprite events were recorded within this period. These events comprise different shapes/structures (carrot (55%), Carrot/Column(11%), Unclassified (21%), Column (13%)) and were similar to what has been reported in the scientific literature.

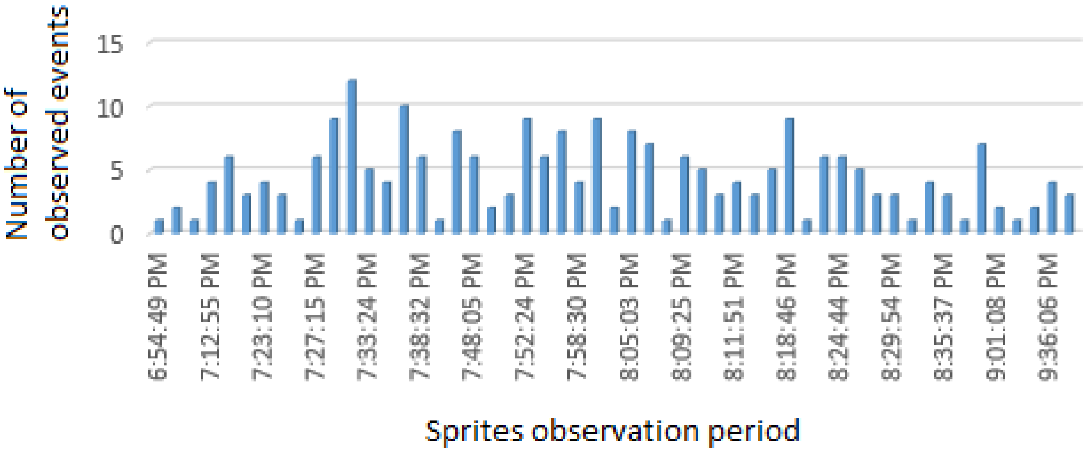

Figure 3.7: Sprite events time-line observed on the 11 January 2016. The number of sprites observed are approximate values because we cannot unambiguously determine the number by visually counting the events on the video frames.

On the night of 2nd February 2016, another cumulonimbus cloud was tracked over the same region in South Africa. In this case, the thundercloud was $\sim$ 280 km away from the observing point, covering an area of almost 150 square km. The storm was assumed to be caused as a result of uplift of cold frost (the frontal type of thunderstorm) from the Indian ocean. The temperature of different sections of this storm was similar to the thunderclouds that were observed on the 11th of January 2016. There were limited opportunity to observe this storm because of the mechanical issues that were encountered with the APT dome. However, four video clips containing $\sim$ 10 sprite events were recorded within a few hours of observations through the glass door in the lower control room of the dome. The observation were stopped when the storm drifted beyond the camera pointing direction through the door.

Figure 3.8 shows some of the events that were recorded during these periods. Table 3.2 shows the morphological statistics of these events.

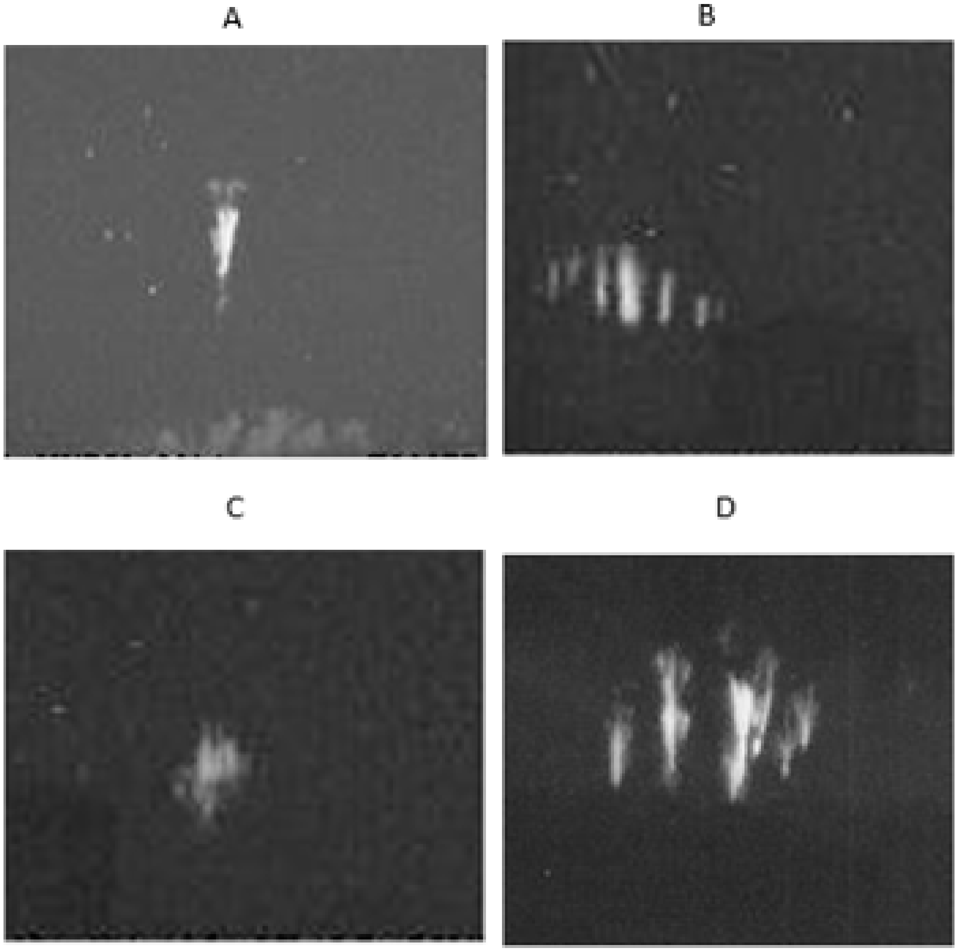
A
B
C
D

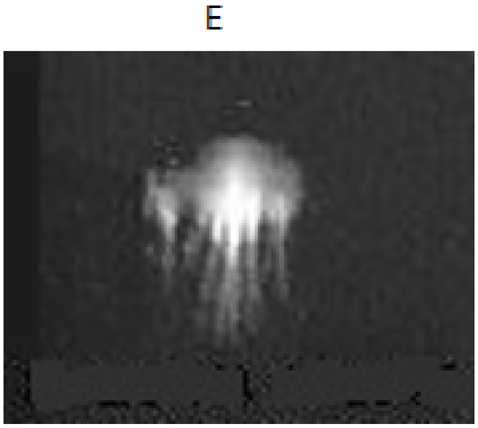

Figure 3.8: Some examples of the sprite events recorded in 2016 with variable zooming of the images: (A) carrot-shaped sprite observed on 2016/01/11 at 18:53:49.4 UTC, (B) column-shaped sprites observed on 2016/01/11 at 19:38:32.5 UTC, (C) unclassified shaped sprite observed on 2016/01/11 at 20:08:03.3 UTC, (D) carrot shaped sprites observed 2016/02/02 at 19:05:55.7 UTC, (E) Jelly-fish-shaped sprites observed 2016/01/11 at 20:29:53.8 UTC. The dark square in the bottom-left in panels (B) and (C) is a telescope dome in the foreground. The bright spots on the images are background stars.

.

Date	**Sprites type**	**Distribution (%)**
2016/01/11	Carrot	55
	Column	13
	Carrot/column	11
	Unclassified	21
2016/02/02	Carrot	100

Table 3.2: Morphological statistics of sprite events recorded during the first phase of the study. The term sprite event denote the smallest identifiable structure of sprites that can be resolved using our camera since the instrument might not be able to unambiguously identify the smallest structure (element) of a sprite.

3.6.2 Multi-wavelength observations

The multi-wavelength observations of sprite events involved the use of optical instruments (i.e. cameras) that operate within a specific range in the electromagnetic spectrum, to observe sprite events. The cameras were fitted with filters that allow the transmission of specific (635-675 nm and 426-440 nm) emissions within the spectrum that correspond to sprites emissions. This technique was also used to observe sprite events during the campaigns in the summer of 2017 and 2018. Figure 3.9 shows the camera set-up and placement during these periods.

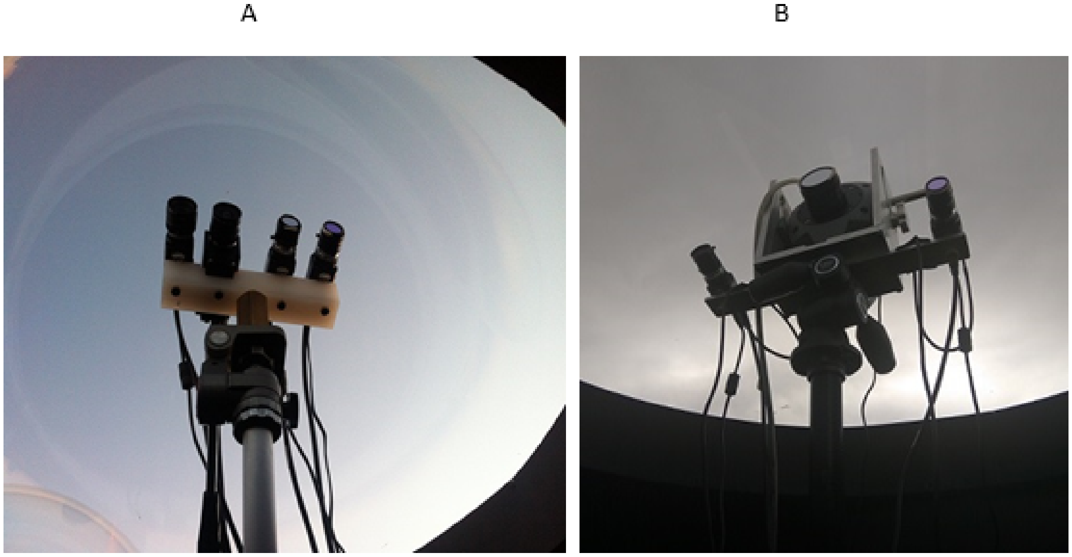

Figure 3.9: Multi-wavelength camera configurations used during this study. Panel (A) shows the configuration used during the 2016/2017 sprite campaign, panel (B) shows the configuration used during the 2017/2018 sprites observation. From the left of panel (A), the first two cameras are the white-light cameras, which is followed by the red-filtered and blue-filtered cameras. From the left on panel (B), we have the white-light camera,which is followed by blue-filtered, and then red-filtered camera

.

In 2017, the sprite campaign was held between the 23rd January and 3rd February, and 21st February and 2nd March 2017. The Watec910Hx cameras that were used for these observations were fitted with a 8mm f/1.4 lens that yielded a FOV of $43^{o} \times 33^{o}$. Two of these cameras had filters to observe sprite events at 635-675 nm and 426-440 nm wavelengths. These observations were made using the SANSA Optical Space Research (OSR) Laboratory that is situated at the SAAO at Sutherland. The OSR Laboratory is 6-metre long by 3-metre-high structure that is situated close to the 1.9-metre Telescope building within the SAAO premises at Sutherland. The facility has two different sections; an optical instrument section, which is regarded as the 'dark room' and the computer section or light room. The darkroom has transparent domes on the roof of this section of the laboratory for optical space-related studies. During sprite campaign, the cameras were mounted on a tripod, connected to the computers that ran the sprites capture software and placed in any of these domes for overnight observation.

On the night of 24th January 2017 (18:50 UTC), an active cumulonimbus thundercloud moving from Central Africa to the Indian ocean was observed over Botswana. The storm was approximately 750 km away from the observation site and had a width that spanned over 900 km covering the North-Eastern horizon from SAAO at a distance. The temperature of various sections of the storm ranged from -31°C to -73 °C. Within three hours of observations, 24 video clips containing over 44 sprite events were recorded. Approximately 13% of these video clips were simultaneously recorded by the white-light and red-filtered cameras. On the 6th of February 2017, a similar thunderstorm was observed over South Africa. In this case, the storm was smaller but actively discharged lightning strokes within an hour. Three video clips containing six sprite events were recorded. One of these events was simultaneously recorded by both the white-light and red filtered cameras. The blue filtered camera was not able to record any of these events because their signals were below the sensitivity of the camera. In all, the structures of the recorded sprite events were similar to what had been observed in the previous year of this study.

Table 3.3 shows the morphological distribution of the events that were recorded during this phase of the study. Figure 3.10 shows the examples of some of the events that were simultaneously recorded by the unfiltered and red filtered cameras.

Observation date	No. of video clips	No. of events observed by each camera			Event morphology	Distribution of morphologies (%)
		White-light	Red-filtered	Blue-filtered		
2017/01/24	24	All	3	None	Carrot Column Unknown Tree-like Carrot/ column	24 35 18 6 17
2017/02/06	3	All	1	None	Carrot Column Carrot/ column	33.3 33.3 33.3

Table 3.3: Sprite event statistics for the first multiple-wavelength observation of sprites reported in this thesis.

Figure 3.10: Some examples of the events that were simultaneously recorded at SAAO using two different cameras: (left) unfiltered white-light images (400 - 750 nm) and (right) filtered red light image (635 - 675 nm). The circled section on the unfiltered (left) images were assumed to be the blue emission in sprites or sprite emissions that were below the threshold of the red-filtered camera. Image (A) was observed on 2017/02/08 at 20:00:28.8 UTC and image (B) was observed on 2017/01/24 at 21:34:28.9 UTC.

The Watec camera is less sensitive when fitted with filters, thus making it unsuitable to observe the weak blue emissions from sprites. To make up for this, in the 2018 sprite observing campaign, a more sensitive optical instrument (iXon EMCCD) was used for the observations. The iXon EMCCD has an electron amplifier that amplifies weak signals above the detection noise floor of the CCD camera. The camera, when fitted with a blue filter, has effectively been used to observe the blue emissions from aurorae in the northern hemisphere, which occur at higher altitudes than sprites.

This phase of the observations started at the SAAO on the 16th of January 2018. In 18 out of the 22 nights of the proposed sprites observations, the thunderstorms when available were predominately around Bloemfontein, which is approximately 800 km to the northern east away SAAO and lies within the lightning-rich region of South Africa. At this distance, the cameras were not able to record any events from the thundercloud. Hence, there was a need to observe the storm from a different location closer to the thundercloud prone region. Thus, a farm at Klerefontein, Carnarvon, was chosen as an alternative observation site for sprites observations within this study.

The observations at the Klerefontein farm were conducted from an open field that is very close to the S-Band communication antenna that is managed by the SA-SKA organisation. During these observations, the antenna was not in operation. The sprites cameras were attached on a tripod mount and connected to the computers that ran the sprites capture software. Access to power and internet for real-time tracking of the storm were provided by the antenna infrastructure, which was also used to shield the instruments from wind on the farm. This methodology was effective to observe sprite events from an open field but was unsuccessful to observe the blue emissions from sprite on this occasion.

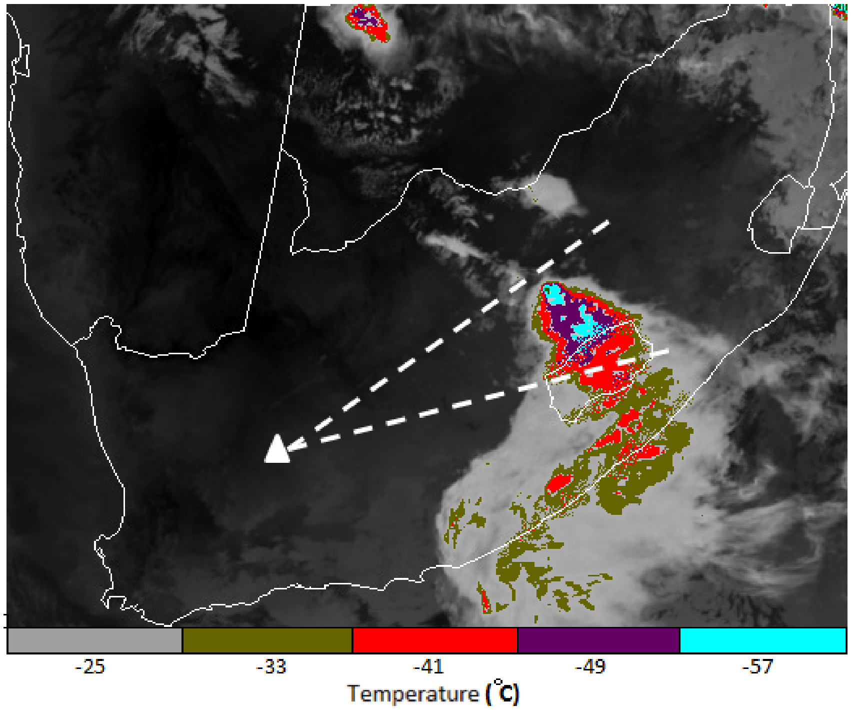

Figure 3.11: The thundercloud observed from Klerefontein farm on 31^{st} January 2018. The triangle shows the observation point; the dotted lines show the camera's cone of view.

On the 31st of January 2018 (20:19 to 01:11 UTC), a cold frontal wave from the Indian ocean caused the development of an active thunderstorm between Bloemfontein and Lesotho. The storm was approximately 500 km from the observation point. The coldest section of this thundercloud was over 350 km wide, with a maximum and minimum temperature of -25°C and -57°C, respectively. Twenty-eight video clips containing over sixty sprite events were recorded within four hours of observations. About 36% of these events were simultaneously recorded with the white-light and red filtered cameras. Since these events were at a much lower elevation in a distant horizon, the EMCCD camera that has the blue filter was not able to record any of these events because of the poor atmospheric transmission of the blue emission due to Rayleigh scattering at the lower elevation. Figure 3.12 shows some of the events that were recorded by the white-light and red filtered cameras.

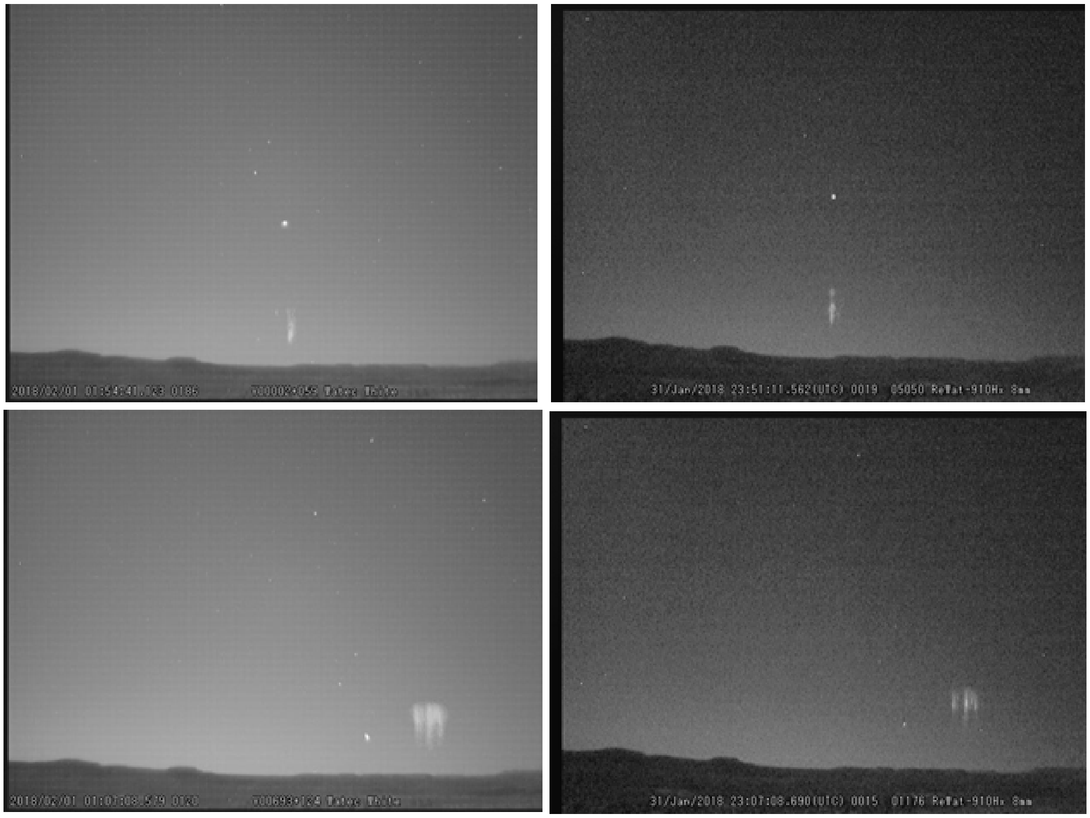

Figure 3.12: Some examples of the events that were simultaneously recorded at Carnarvon using two different cameras on the 31st of January 2018. (left) unfiltered white-light images and (right) filtered red light images.

Chapter 4

Data analysis

4.1 Image location and calibration using known stars in the star catalogue

The video frames were analysed using the Sonotaco Sprite Analyzer software, which has star coordinates from the SKY2000 Master Catalogue version 4. The stars from this catalogue were overlaid on the background stars on each of these sprites images in order to determine the azimuth and elevation angle of the sprite events. The alignment of these stars was manually done for any given camera pointing direction, location and time during the observations. The sprites analyzer software was able to determine an approximate coordinate (latitude/longitude) of each sprite events by knowing the elevation/azimuth of the reference stars and with the assumption that the top maximum emission altitude of sprite events is around 85 km (Pasko et al. 1997; Barrington-Leigh 2001; Wescott et al.

2001). This process works very well when there are many stars in the background of the sprites images, as shown in Figure 4.1, and was used in this dissertation. Table 4.1 shows the coordinates of each of these sprites (from left to right), as can visually be resolved by the observer.

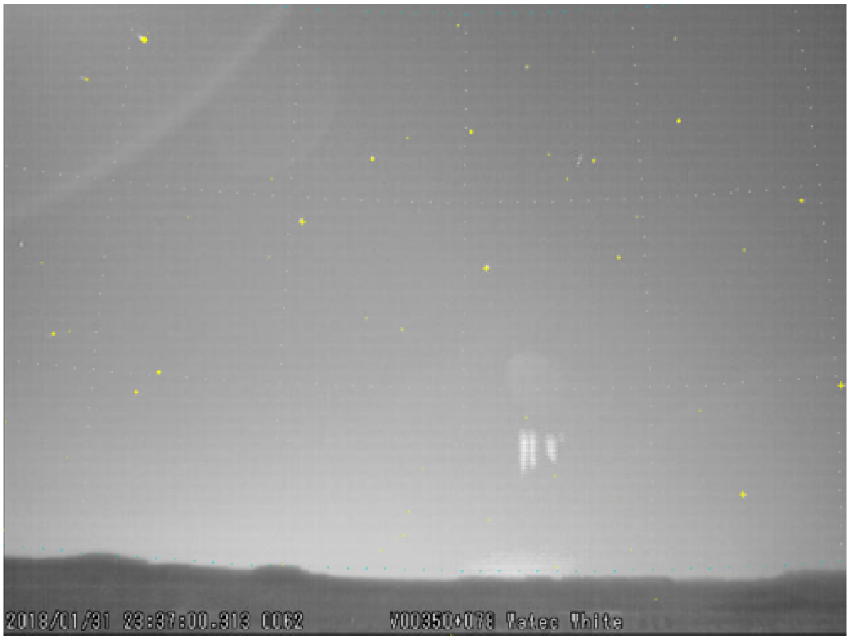

Figure 4.1: Sprite events and their corresponding celestial coordinates as derived from the Sonotaco Sprite Analyser software. The yellow dots on the image are the overlaid stars (∼ 47 stars) from the star catalogue.

Azimuth Angle	Elevation Angle	Longitude	Latitude
63	7.7	26.3333	-28.9747
64	7.8	26.3642	-28.9973
65	7.5	26.4902	-29.0322

Table 4.1: The coordinates of sprite events in Figure 4.1. (from left to right), as seen by the observer.

Since these images were not simultaneously recorded by two or more cameras that are positioned at different observations sites, the precise geographical positions could not be determined. However, their approximate locations were assumed by matching the coordinates of these events in position and time to a corresponding lightning stroke in the lightning strokes dataset because sprite events usually appear within 50 km horizontal distance away from their causative lightning strike (Wescott et al. 2001; Cummer and Fullekrug 2001). The coordinates of the lightning stroke that was closer to the position of the sprites as derived by the software was assumed to be the location of the event. Where there are multiple lightning strokes over an area, the sensors of the lightning detection network usually differentiate the time of arrival (TOA) of each of these strokes. In this case, the TOA of the stroke that was closer to the timestamp on the image and its position were used as the actual location of that event. There are a few other situations where a cluster of sprite events was associated with a single lightning stroke because the events appeared on a single video field (20 ms), within a few milliseconds and were less than 50 km from the assumed causative lightning stroke. In those cases, the location of the lightning strikes that preceded the sprite events in position and time were used as the approximate location of the events. Figure 4.2 A and B shows two clustered events and their positions with reference to background stars and the corresponding lightning stroke that was retrieved from the lightning detection networks.

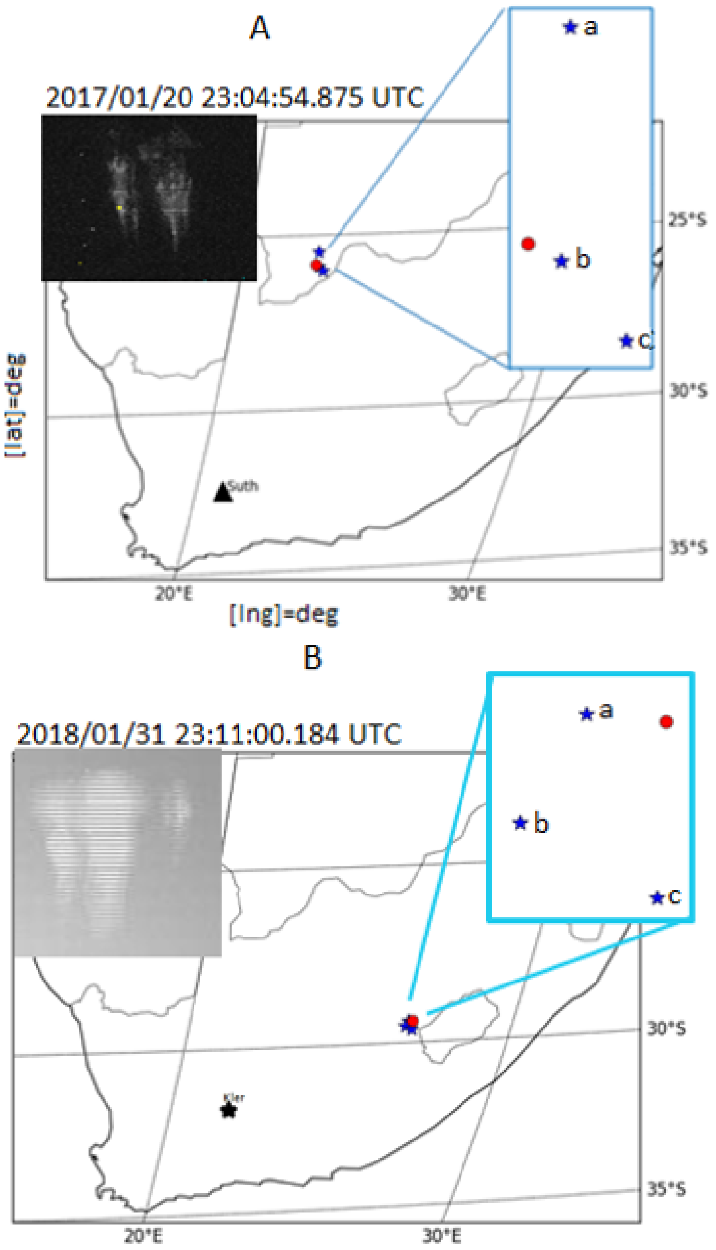

Figure 4.2: Two clusters of carrot-shaped sprite events observed simultaneously within a video field. While the red circle on the maps (A and B) shows the position of the lightning strikes that triggered the sprite events, as recorded by the SAWS LDN and verified by the ENTLN, the blue stars are the positions of the individual sprites in the group. These events were less than 40 km away from this causative lightning stroke. The black triangle on image "A" and the black star on the image "B" that was marked "suth" and "Kler" respectively show the position of the camera during the campaign. The two examples are shown for 2017 (panel A) and 2018 (panel B). The scale of the zoom is arbitrary.

4.1.1 Distance estimation

Previous studies have shown that sprites usually occur at a maximum altitude range of 78 to 90 km (Pasko et al. 1997; Barrington-Leigh 2001) and have a horizontal width that spans tens of kilometres at its widest point (Sentman et al. 1995). In this study, we assumed that the maximum altitude of the sprites was approximately 85 km. We then used the stars to deduced the camera's pointing direction, the elevation and azimuth angle of each sprite events. The uncertainty when using this method is dominated of the star-fit image pixel jitter in the vertical direction and the error (±5km) (Sentman et al. 1995) in the sprites initiation altitude. Figure 4.3 shows the source-observer geometry, where S is the source (sprite events), O is the observer's position, h is the altitude of the sprites, R_e is the radius of the Earth, d is the ground distance to the location of sprite events, ε is the angle subtended at the center of the Earth and θ is the camera pointing angle.

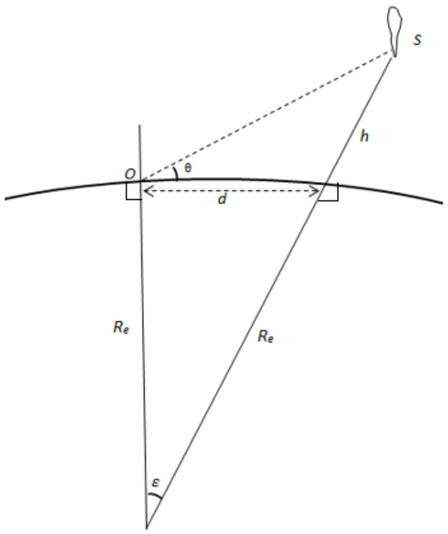

Figure 4.3: The source-observer geometry. Adapted from Kosch et al. (2009)

In spherical geometry,

$$\tan(90-\theta)=\frac{(h+R_{\mathrm{e}})\sin\varepsilon}{(h+R_{\mathrm{e}})\cos\varepsilon-R_{\mathrm{e}}} \tag{4.1}$$

where ε = d/ $\mathrm{R_e}$, Equation (4.1) becomes:

$$\tan(90-\theta)=\frac{(h+R_{\mathrm{e}})\sin(\frac{d}{R_{\mathrm{e}}})}{(h+R_{\mathrm{e}})\cos(\frac{d}{R_{\mathrm{e}}})-R_{\mathrm{e}}} \qquad \equiv \qquad \tan\theta=\frac{(h+R_{\mathrm{e}})\sin(\frac{d}{R_{\mathrm{e}}})}{(h+R_{\mathrm{e}})\cos(\frac{d}{R_{\mathrm{e}}})-R_{\mathrm{e}}} \tag{4.2}$$

Using the trigonometric relation,

$$\tan\theta=\frac{sin\theta}{cos\theta}$$

Equation 4.2 becomes:

$$\equiv \qquad \frac{sin\theta}{cos\theta}=\frac{(h+R_{\mathrm{e}})\sin(\frac{d}{R_{\mathrm{e}}})}{(h+R_{\mathrm{e}})\cos(\frac{d}{R_{\mathrm{e}}})-R_{\mathrm{e}}} \tag{4.3}$$

Simplifying equation 4.3 by assuming that $A=h+R_{\mathrm{e}} \qquad B=d/R_{\mathrm{e}}$

$$\frac{sin\theta}{cos\theta}=\frac{AsinB}{AcosB-R_{\mathrm{e}}}$$

$$Asin\theta cos\theta B-R_{\mathrm{e}}sin\theta=Acos\theta sinB$$

$$sin\theta cosB-cos\theta sinB=\frac{R_{\mathrm{e}}sin\theta}{A}$$

$$\theta=Bsin^{\text{-1}}\left(\frac{R_{\mathrm{e}}sin\theta}{A}\right)$$

Since A = h + R and B = d/$\mathrm{R_e}$

$$\frac{d}{R_\mathrm{e}} = \theta - sin^{\text{-1}}(\frac{R_\mathrm{e} sin\theta}{h + R_\mathrm{e}})$$

$$d = R_\mathrm{e}[\theta - sin^{\text{-1}}(\frac{R_\mathrm{e} sin\theta}{h + R_\mathrm{e}})] \tag{4.4}$$

Equation 4.4 was used to estimate the distance between the observer and sprite events. The result of this estimation shows that the average distance between the source (sprite events) and the observer was 639, 784 and 575 km for the events recorded in 2016, 2017 and 2018 respectively. The error in this estimation was ±5% of the distance, which implies that, for events that were 800 km away from the observation point, the uncertainty in the estimations was ± 40 km.

4.2 Sprite-producing thunderstorms

For most of the campaign nights, there were no thunderclouds over South Africa or within the range of view of our cameras. However, a total of 7 convective thunderclouds were observed during the 65 nights of observations. During these periods, sprites were observed in 5 out of 7 convective storms. These thunderclouds were smaller than those that occur in North and South America. We classified these storms as sprites-producing storms because sprites were observed from them. We further sub-classified these sprites-producing convective storms into two categories based on their dimensions and mechanism that influenced them.

On the 11th of January 2016, one of these convective sprites-producing thunderstorms was observed. The development, which started in the late afternoon/evening, reached its full extent around midnight, occurred as a result of the strong air current from the Indian Ocean or the Mozambique channel, which forced the cold air parcel to rise above the high plains over land. The storm had a horizontal dimension that was less than 500 km and an active horizontal section that was also less than 300 km. This storm was classified as category "A" because it was influenced by a cold front from the ocean. The sprites-producing phase of this storm was assumed to be within the time-frame that sprite events were recorded over the storm, started around 18:30 UTC and lasted for approximately 3 hours. This phase coincided with the active (energetic) phase of the storm as seen from the Meteosat imagery. Similar storms were observed on the 2nd February 2016, 6th February 2017 as well as on the 31st January 2018, but in these cases, the thunderstorms were smaller and very weak, having an active section that was less than 150 km. However, sprite events were also observed within a few hours that also correspond to the active phase of the storm as seen from the satellite imagery. Figure 4.4 shows the cloud-to-ground lightning discharges that were associated with this thunderstorm.

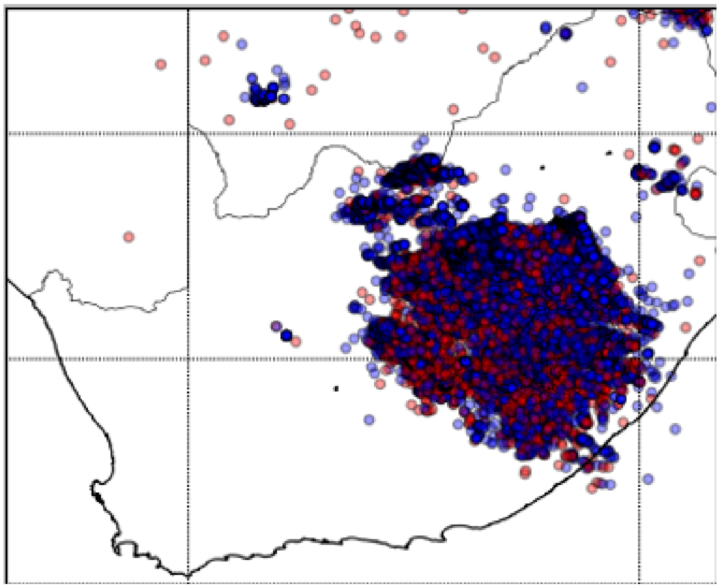

Figure 4.4: The cloud-to-ground lightning discharges associated with the type–A thundercloud that was observed between 18:30 - 22:39 UTC, 11th January 2016. The red dots are the positive CG strokes; the blue dots are the negative CG lightning strokes, which suggests that we had more of negative lightning discharges. There were limited number of lightning strokes detected over Namibia because the efficiency of the South African Lightning Detection Network is limited over that region

We also observed a different type of sprites-producing thunderstorm on the 24th of January 2017. In this case, the thundercloud spanned over hundreds of kilometres covering much of Namibia, Botswana and South Africa. This large thundercloud was partly influenced by the cold current from the South Atlantic Ocean as well as the current from the Indian Ocean. The adjacent high plains in Namibia and South Africa forced the moist air produced by these currents to rise. The convective systems resulting from the updraught of these air parcels covered most of the country and later merged over Botswana, having a series of active hotspots with a lifetime that exceeded several hours. This type of thunderstorm was classified as category "B" because it covered hundreds of kilometres. The sprites-producing section of the thunderstorm that was closer to the observer was over Botswana (approximately 800 km from the observation site), lasted for more than 3 hours. Figure 4.5 shows the lightning discharge activity over South Africa during this storm.

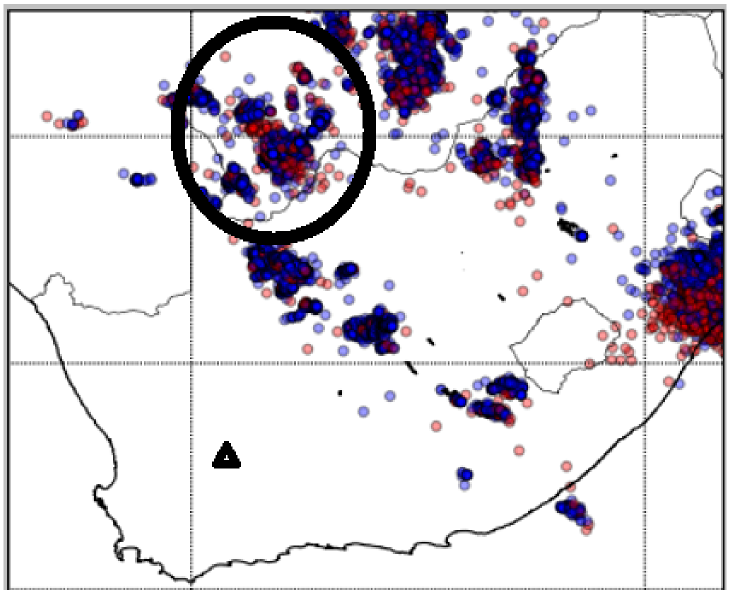

Figure 4.5: The cloud-to-ground lightning discharges associated with the category B thundercloud observed on the 24th of January 2017. The storm was more active over Namibia and Botswana. There were a limited number of lightning strikes over Namibia because the plot was derived from the lightning stroke data of the SALDN, which also detects lightning discharges in some parts of Botswana. Whilst the red dots are the positive CG lightning discharges, the blue dots are the negative CG lightning strokes.The black triangle shows the observing point. The sprites-producing region that is closer to the observation point is enclosed in the large circle.

4.2.1 Estimation of the cloud-top temperature of clouds that initiate sprite events

As a way to estimate the cloud-top temperatures of clouds that initiated sprites, the images of the thunderclouds that initiated these events were downloaded from the secured server of Meteosat. These images were colour-coded using an algorithm that was developed for that purpose. The algorithm read the image pixel values, using the pixel conversion look-up table (see Appendix A1) of the Meteosat infrared imagery, the algorithm was able to assign colours that have a temperature value to different sections of the image based on their pixel value. The ideal method to determine the cloud-top temperature and height would have been to use radar data (Chris Lennard, Personal communication, 2017), but where such a facility was not available during the study, the algorithm was used.

We then plotted the coordinates of each sprite events on a map and overlaid these maps on an appropriate colour-coded image of the storm that initiated the event. The cloud-top temperature as at the time the events were initiated was read from their position on the colour-coded map. Figure 4.6 shows some examples of these plots.

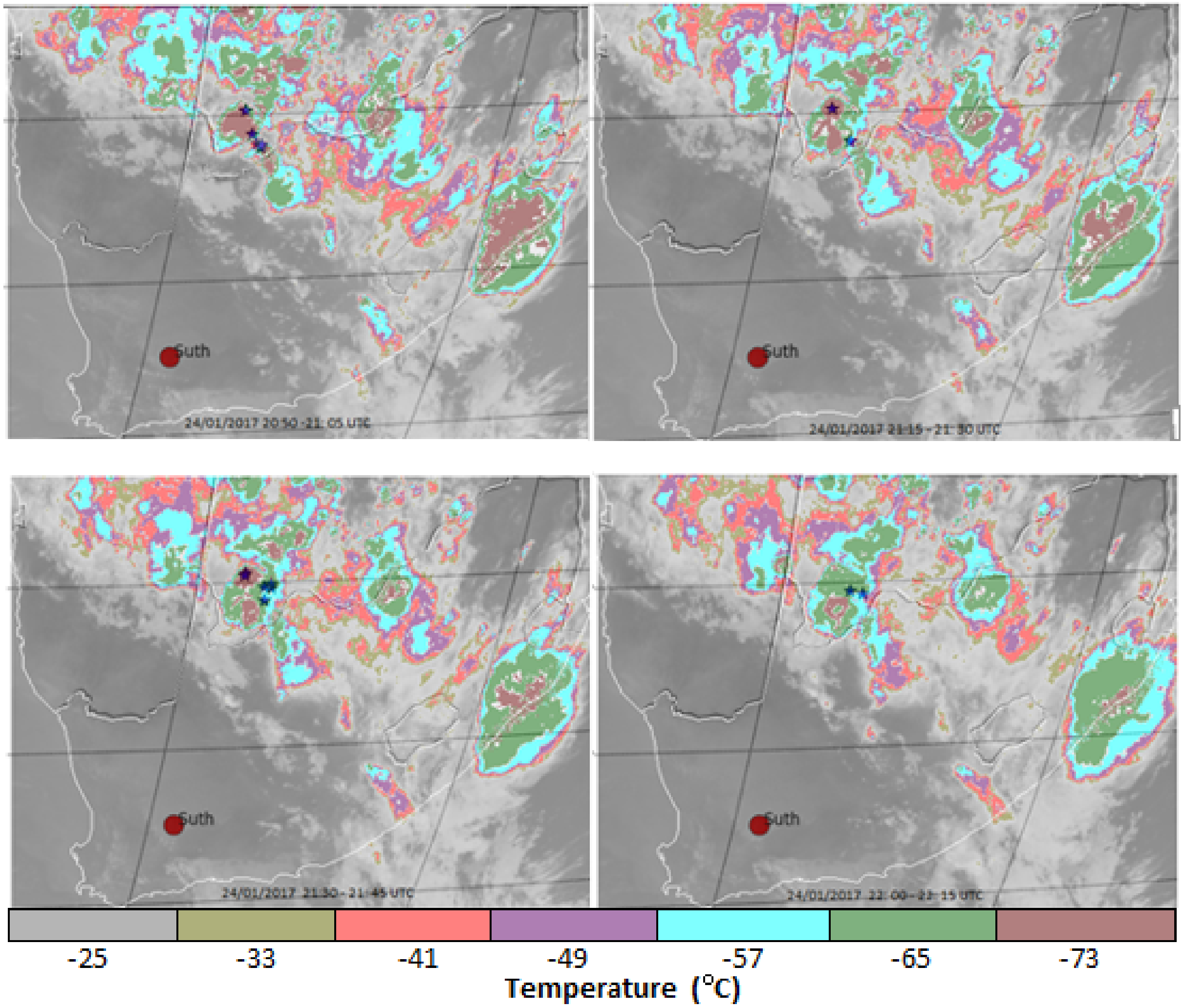

Figure 4.6: Some of the delineated structure of the thunderstorm based on the cloud-top temperature of different sections of the storm. The location marked "Suth" was the observation site. The panels are the thundercloud that was downloaded at 15-minute intervals during the observations. The blue-star symbol on the images represents the position of the sprite events that were recorded within the time frame of the storm.

The average cloud-top temperature of the storm that initiated the sprite events recorded during this study was derived from these plots, which suggest that the average temperature of the storms we observed in 2016, 2017 and 2018 was -52°C, -67°C, and -56°C respectively. Relating these temperature values to the atmospheric temperature height profile (Figure 2.3) shows the variation in the cloud-top height during these campaigns as shown in Table 4.2, which summarises the characteristics of the observed thunderstorms and the approximate number of sprites that were observed over the storms.

Date	Storm system linear size ∼(km)	Active cell linear size ∼(km)	Min. Cloud-top temperature (°C)	Cloud-top height (km)	No. of sprite events
2016					
2016/01/11	480	280	-65	15	95
2016/02/02	400	220	-49	12	10
2017					
2017/01/24	>2000	290	-73	18	46
2017/02/06	400	150	-65	15	3
2018					
2018/01/31	506	150	-57	12	62

Table 4.2: Summary of the characteristics of the thunderstorms observed during this study.

We also compared the different structures of observed sprites to the cloud-top temperature of the storm that initiated them. This comparison suggests that the mechanism that determines the varying shape of sprites has no relationship with the cloud-top temperature of the storm.

4.3 Sprite classification and the nature of lightning processes

The observations show that sprites come in a variety of forms and concentrations. Classifying these events into their respective groups (number of events and shapes) was not difficult because they assume similar structures that have been reported elsewhere, aside from a few events that could not be classified into any of these known structures. Those events were regarded as unclassified structures. Figure 4.7 shows the classification of events based on the number of sprite events on each image.

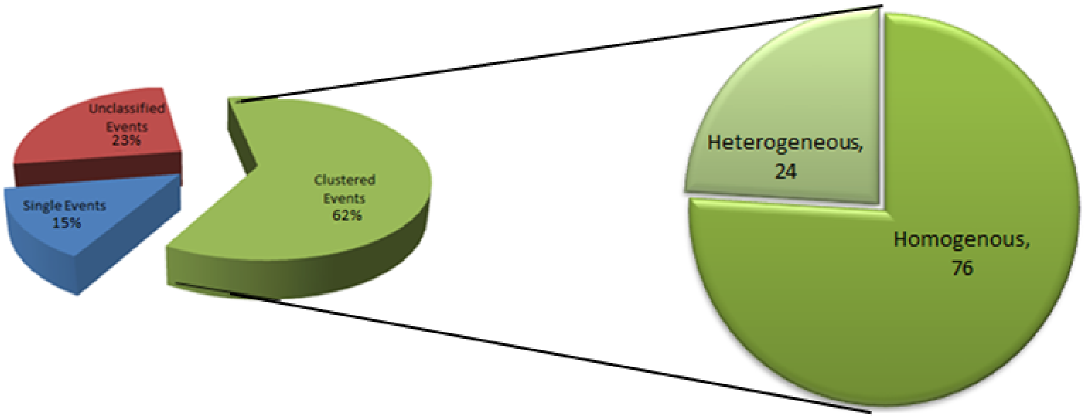

Figure 4.7: Classification of the sprite events observed in the austral summer of 2015/2016, 2016/2017 and 2017/2018. The single-type events are either carrot, column or tree-like-shaped sprite events, which can unambiguously be resolved by the observer. The clustered events are groups of sprites that were recorded within a single video clip, which comprise sprite events of the same structure (homogeneous) or various shapes (heterogeneous)

.

These events were further associated with their causative lightning stroke (Figure 4.8) using the coordinates that were retrieved from the sprites analyser software. These coordinates were matched in position and time to lightning flash data from the South African Weather Service (SAWS) lightning detection network and the Earth Network, Total Lightning Network (ENTLN). The essence of using the lightning stroke data from two different sources was to verify the position and time of arrival of these flashes. While both LDNs provide the date/time, longitude and latitude of the stroke, their peak current (kilo-Amps) and polarity of these lightning strikes, the ENTLN also provides the information relating to nature (IC or CG) of the stroke. This information was effectively used to understand the nature of the causative lightning flash that initiated each sprite events.

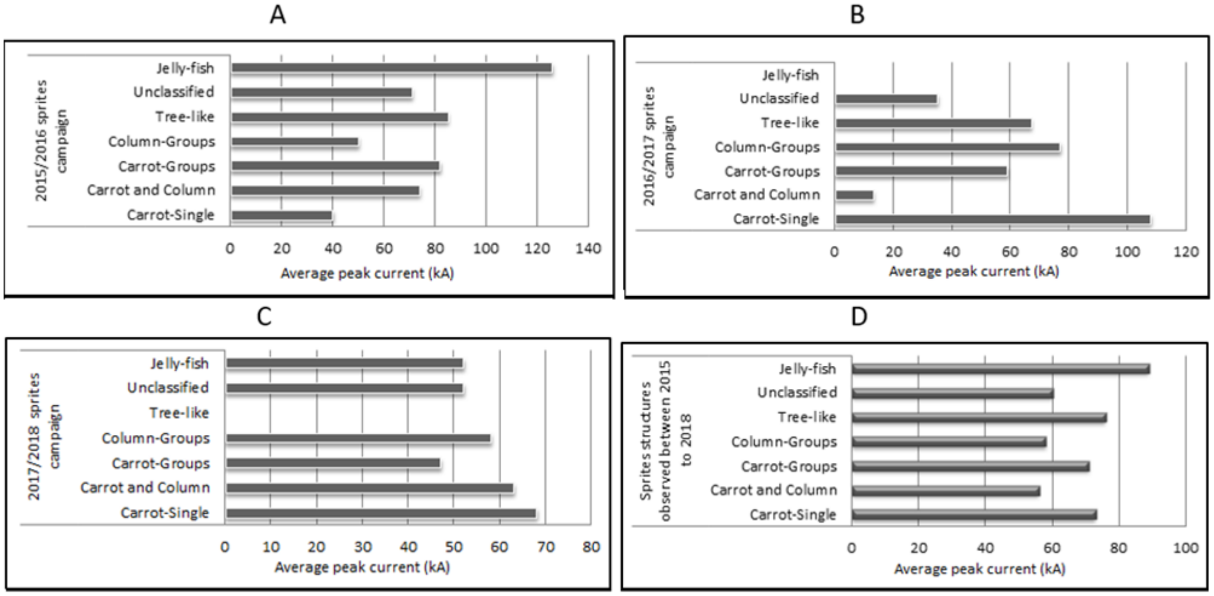

Figure 4.8: Sprites structures and the average peak current of the lightning strike that initiated them. Whilst panels A, B and C represent the structural statistics of the events recorded in 2016, 2017 and 2018 respectively, panel D represents all the events recorded in this study. The SAWS data was used for this plot.

The timestamp on the sprites video frames was associated with the TOA of large positive lightning strikes on these data sources (SAWS, ENTLN), prior to the timestamp on the sprite's video frames. In most of the cases, the lightning strikes that triggered the sprite events were detected by either one of the two lightning detection networks or both. Whilst there are some events whose causative lightning flash was not detected by any of these lightning detection systems, there were also a few other events where the ENTLN identified their causative lightning strokes as IC lightning discharges. These events were further analysed.

4.3.1 Sprites without causative lightning strokes

Figure 4.9A shows some of the sprite events for which we were not able to identify their causative lightning flash. These events appeared a few minutes after a group of sprites that are known as dancing sprites (Figure 4.9B) were recorded. Sprite events are considered to dance across the sky when they appear one after another, displaced in time and in space, thereby creating an illusion that they dance.

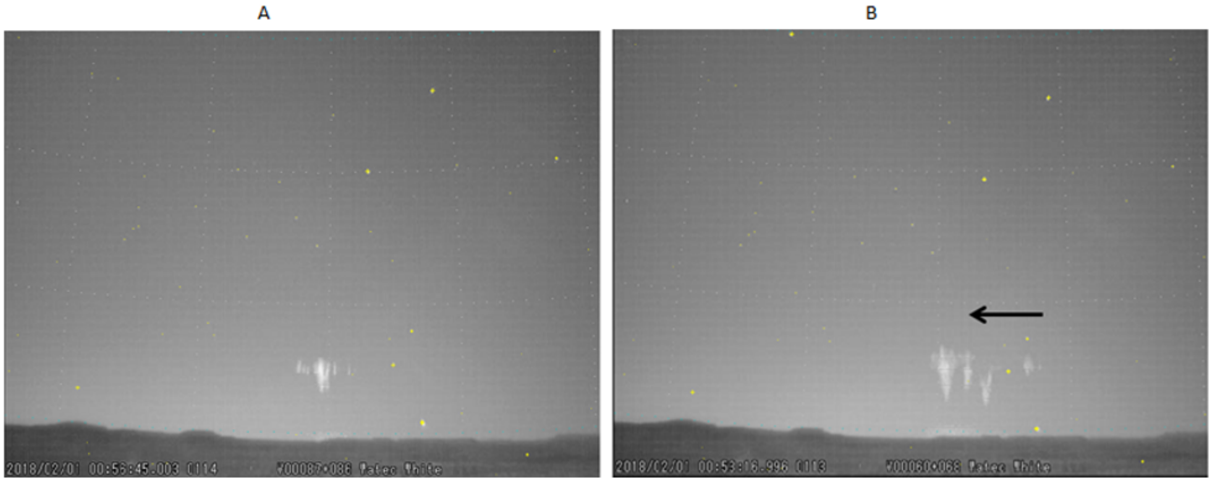

Figure 4.9: (A) Sprite events without a causative lightning (00:53:16.996 UTC, 2018/02/01). (B) Dancing sprite events recorded at 00:56:45.003 UTC 2018/02/01, prior to the events shown in Figure 4.9A. The black arrow on the image shows their direction of movement across the sky. The bright dots are the bright stars used during image calibration.

We assumed that the lightning strike that triggered most of the events listed in Table B1, B2 and B3 (see Appendix B) was not found because in some cases, the algorithms of most of the LDNs usually flag some large sprites producing +CG lightning strokes as questionable detections whenever their error ellipses exceed certain values (Martin Fullekrug 2017, personal communication). In the case of the event shown in Figure 4.9(A), we assumed that the event was triggered by a charge redistribution in the cloud as reported by a few studies (Der Velde et al. 2006; Wescott et al. 2001), following the dancing sprite events.

4.3.2 Sprites initiated by intra-cloud lightning strokes

A comparison of the waveform signals that correspond to the sprites producing lightning discharges was made, using the lightning flash waveform data from the ENTLN system. This shows that the waveform signals of the lightning flash that triggered three of the sprite events were IC lightning flashes. The signals for IC lightning discharges differ from CG flashes and are characterised by a longer rise time and peak width of the waveform, whereas the characteristic waveforms for CG lightning flashes have a shorter rise time and peak width (Jeff Lapierre, personal communication, 25th Sep. 2018). During the observation, the concurrent spectrum of radio receivers that operate between 4Hz–400 kHz, indicates the presence of radio noise in the cloud when these 3 images were recorded by the video camera. Figure 4.10 (panel "A1" and "A2", "B1" and "B2", "C1" and "C2") shows the waveform signals for the IC lightning discharge as recorded by different sensors of the LDN. Panels "A3", "B3" and "C3" show the lightning activities in the cloud and panels "A4", "B4' and "C4" show the sprite events that were recorded. Figure 4.11 ("A", "B") shows a sample of the CG lightning flashes.

A1

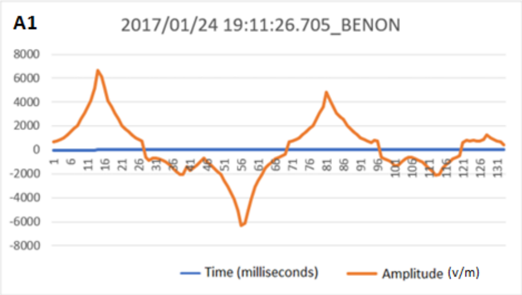

A2

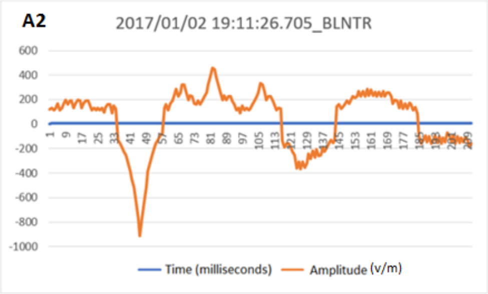

A3

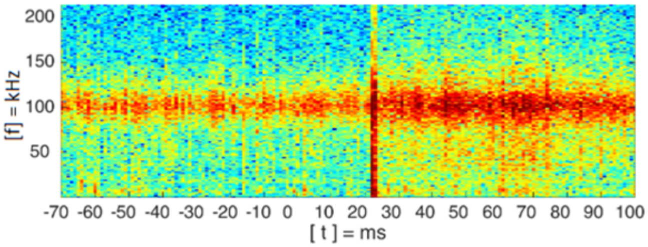

A4

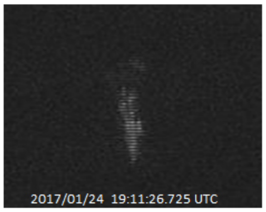

B1

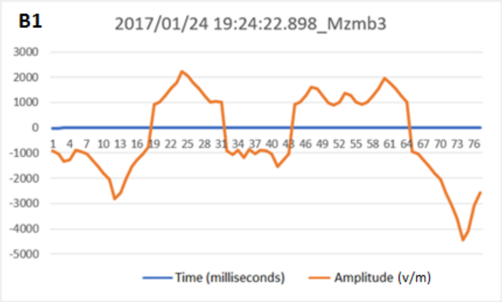

B2

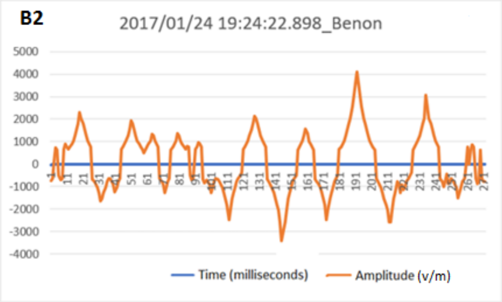

B3

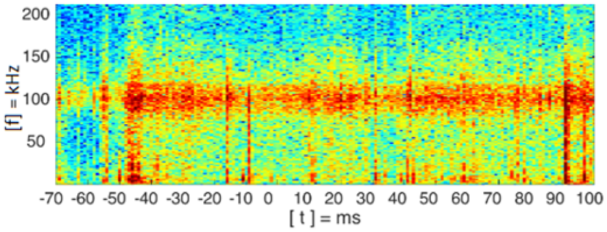

B4

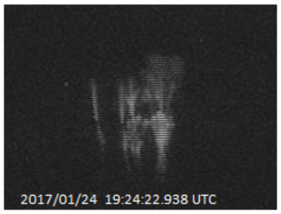

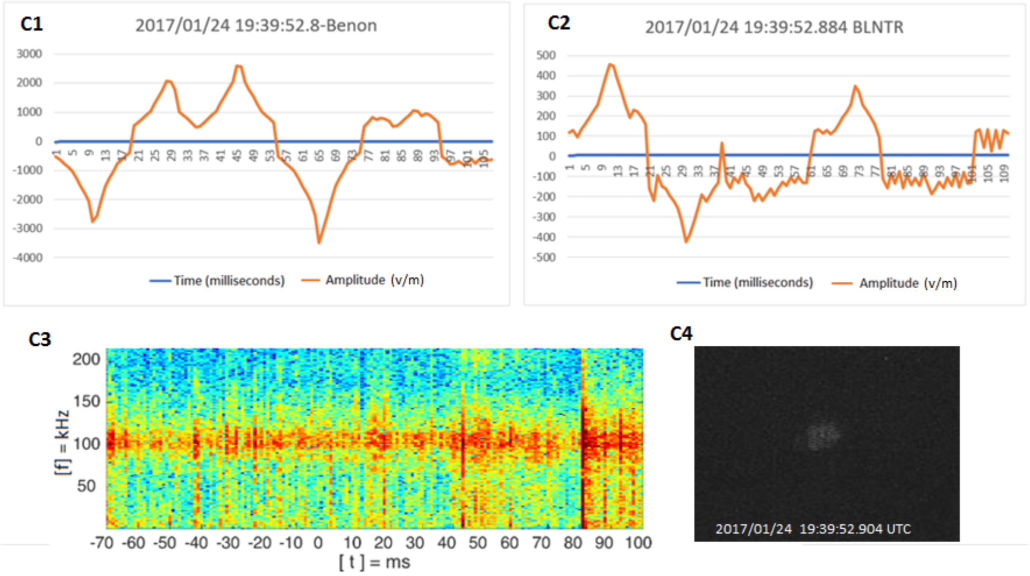

Figure 4.10: Panels "A1" and "A2", "B1" and "B2", and "C1" and "C2" show the waveform signals for the IC lightning flash the initiated the sprite events (panels "A4", "B4" and "C4"). Panels "A3", "B3" and "C3" are the spectra of the radio receiver showing the lightning flash activities in the cloud prior to the sprite events. The t=0 is the time of the initiation of the lightning strike, which was preceded by sprites initiations. The name tags "BENON", "BLNTR", and "Mzmb3" are the lightning sensor designated names. The "wiggles" on panel "A2" and "C2" are local noise on the waveform as a result of the distance between the sensor (BLNTR) and the position of the stroke, which was approximately 500 km. In all the cases, the waveform signal rise time is more than 5ms.

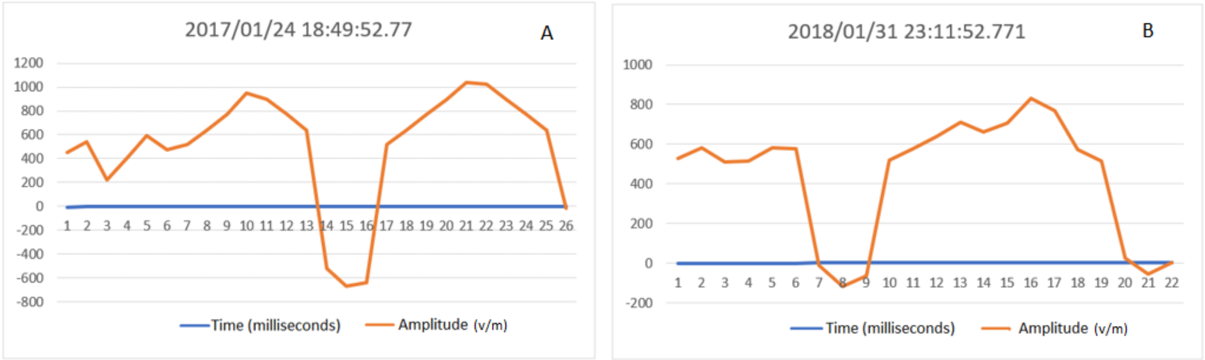

Figure 4.11: Sample waveforms for two CG lightning flashes. (A) and (B) are waveform signal for different lightning strokes. The signal rise time is ∼1ms.

Although the general assumption was that sprites are produced by strong positive CG lightning discharges, these events, however, support a few other studies (Der Velde et al. 2006; Ohkubo et al. 2005) which suggest that IC lightning discharges can also initiate sprites.

4.4 Sprite brightness, emission profile and electron flux estimation

4.4.1 Sprite brightness estimation

Sprite brightnesses were analysed using the ImageJ software (`https://imagej.net/ImageJ`). We also referenced the brightness of a star that appeared on the sprite image since the stars have a known constant brightness. In order to achieve this, we read the pixel value of the stars on each of the sprites image and documented their average pixel(brightness) value ($\mathrm{Star}_{\mathrm{avg}}$). The essence of using the average of these values over a certain period was to remove the scintillation effect, which is caused by the presence of the atmosphere between the observer and the stars. We then used the $\mathrm{Star}_{\mathrm{avg}}$ to estimate the brightness of all the sprite images that were recorded on that night because the camera gain setting was set to a fixed value (35 db) during the observations. Figure 4.12 shows a plot of the star brightness for 50 frame images of the star.

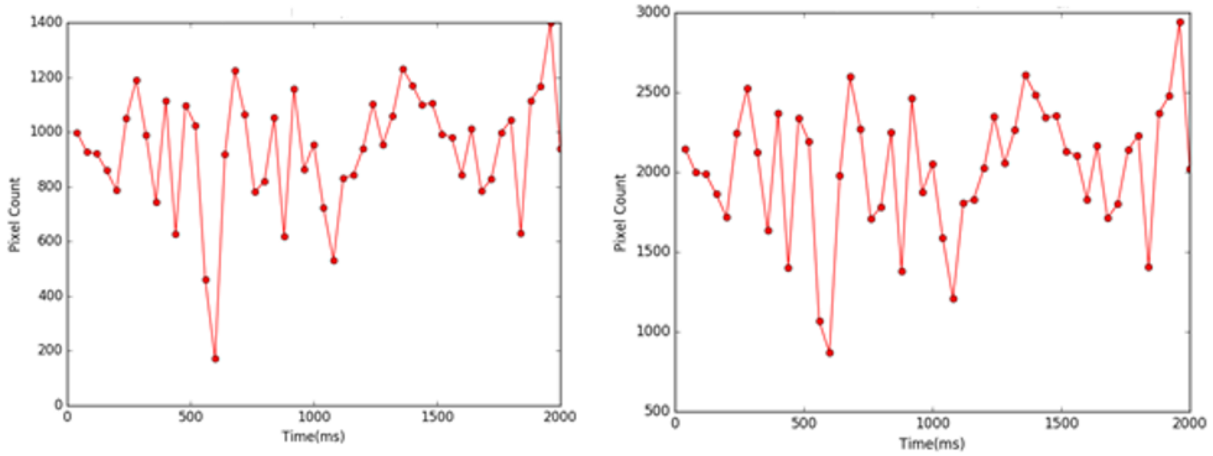

Figure 4.12: The reference star brightness that was observed within sprites video frames on different nights of observations (24 January and 2nd February 2017).

We then applied a 7 X 7 median filter on all images to remove the background stars and any underlying lightning flash from the storm (Figure 4.13). Next, we measured the brightness of two different areas of the sky background (without sprite events, marked "1" and "2") on the opposite sides of the sprite events (Sky_{bk1} and Sky_{bk2}).We then recorded their average brightness (Sky_{avg}) and the brightness of an area that was a superposition of both background sky and a sprite events ($\text{Sp+Sky}_{\text{bk}}$) were documented.

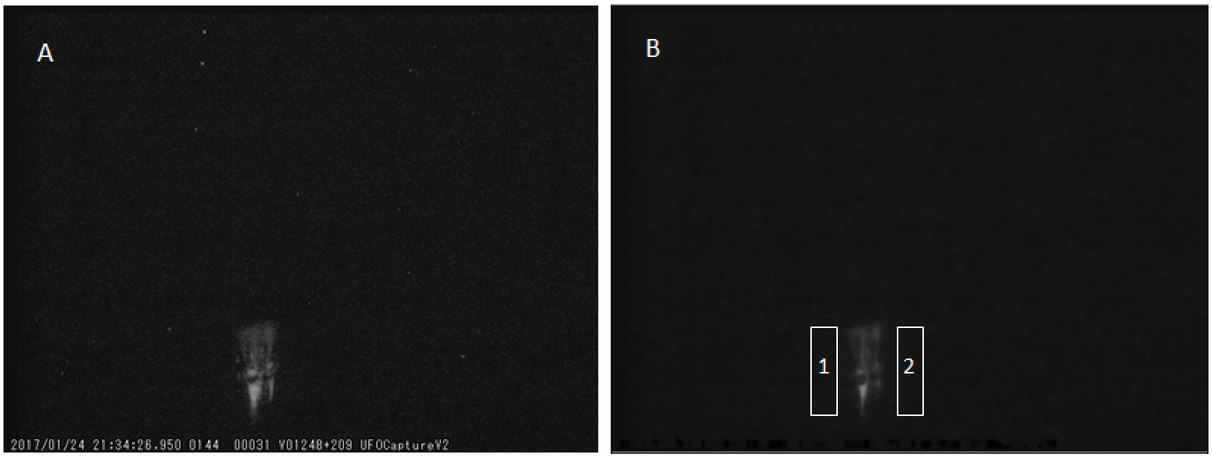

Figure 4.13: Sprite event (A) before and (B) after 7 × 7 median filter to remove the background stars. The sections marked “1” and “2” on image “B” are the areas that were used to derive the value of the background sky intensity.

We ensured that these measured areas (Sky$_{\text{bk1}}$, Sky$_{\text{bk2}}$, Sp+Sky$_{\text{bk}}$) had the same dimension and were measured at approximately the same altitude in the sky where the sprite events appeared on the image. Thereafter, we derived Sky$_{\text{avg}}$ from Sp+Sky$_{\text{bk}}$ to estimate the brightness of each sprite events. Finally, we normalised the sprite’s brightness values by dividing its brightness values by the average brightness of the referenced star (Star$_{\text{avg}}$). Since brightness is inversely proportional to the square of the distance, we then divided each of the obtained values by the square of its corresponding distance to the observer. Table B.1 (Appendix B) shows the sprite events that were recorded in 2016, and their corresponding mean brightness values, which range from 4.25×10^{-4} to 8×10^{-9}(arbitrary units). There was no quantifiable relationship between the brightness and peak current for the sets of observed sprites.

4.4.2 Sprite emission profile for the broadband and N2 PG band emissions.

We used sprite events that were simultaneously observed by the white-light and red-filtered cameras to estimate the emission profile of sprites that correspond to the broadband and N2 (PG) band emissions. In order to achieve this, we used the same procedure that was formerly used to estimate the brightness of sprites, but in this case, we assumed that the top maximum and bottom minimum brightness altitudes of the events were 85 km and 40 km respectively, which suggests that sprites have a vertical profile range of 45 km. We then divided this vertical profile into nine equal sections with the assumption that each section spans approximately a 5 km vertical. Next, we measured the pixel value of each of these sections that comprises the superposition of the sprite events and background sky (Sp+Sky) and also the average pixel value ($\mathrm{Sky_{avg}}$) of two adjacent areas of the sky without the sprites, but at the same altitude of each Sp+Sky measurement. Thereafter, for each of the Sp+Sky, we subtracted the value of $\mathrm{Sky_{avg}}$ to derive the emission of that event at each height. This was done on both the filtered and unfiltered sprites images. The values that were derived from this subtraction were used to plot the emission profile for specific sprite events that were recorded using the red filtered and unfiltered cameras. Figure 4.14 shows a sample of the sprite events and their corresponding emission profile plots. Figure 4.15 shows the emission profile of some other events that were simultaneously recorded by the white-light and red-filtered cameras. These plots suggest that the N2 (PG) emission within sprites dominates around 65 km, for the 5 events for which the emissions profile was analyzed.

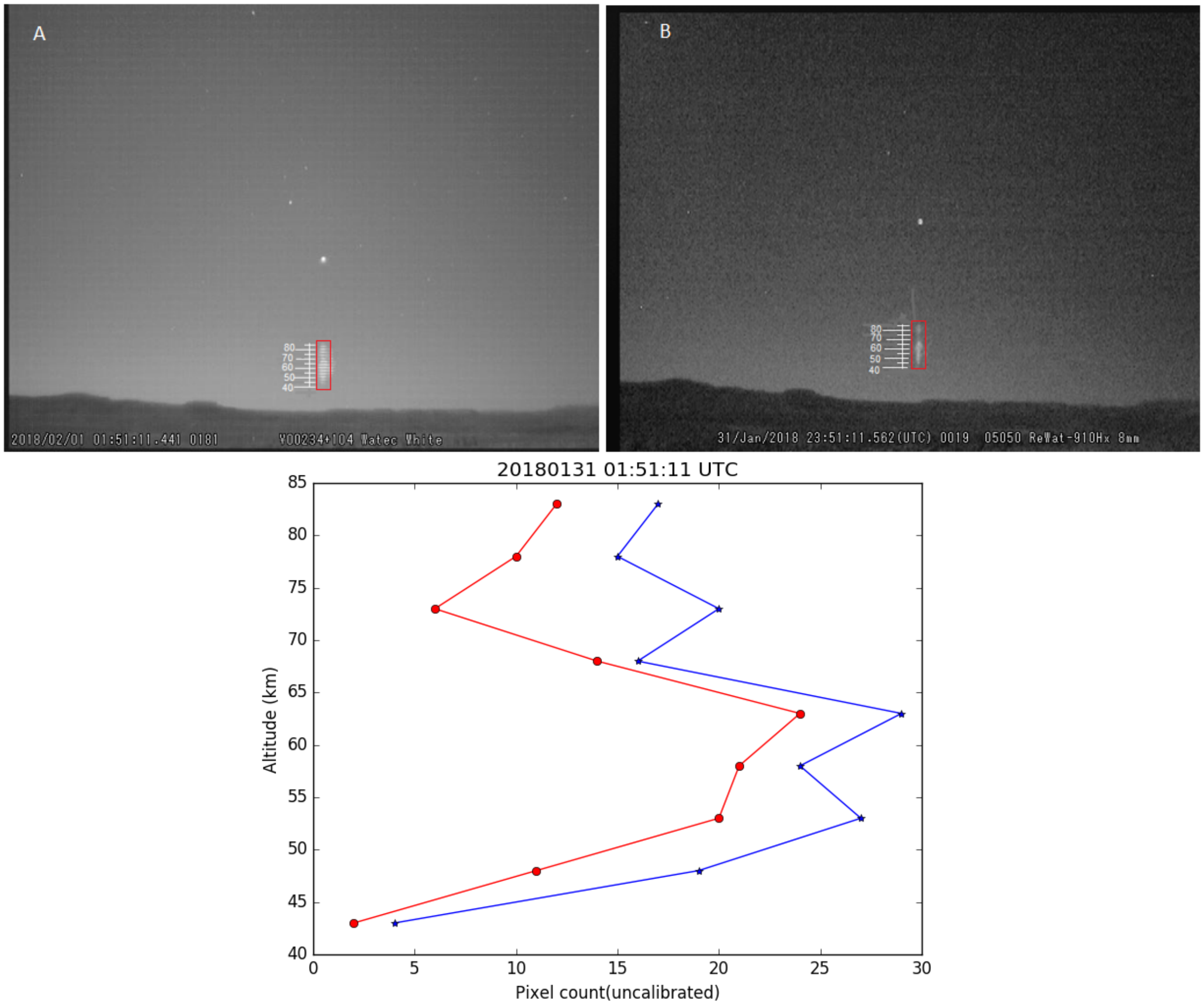

Figure 4.14: A sample of a sprite events that was simultaneously observed with the multi-wavelength cameras. Panel "A" shows the image of the sprites that was acquired with the white-light (unfiltered)camera. Panel "B" shows the same event as recorded with the red-filtered camera, which we regard as the N2 (PG) emission band. The bottom panel shows the emission profile of the event for both the white-light(blue dots) and red-filtered (red dots) camera. The red rectangular section on the images shows the area that was used for the estimation of the emission profile. The bright dots on the images are the reference stars that were used to calibrate the brightness of the event.

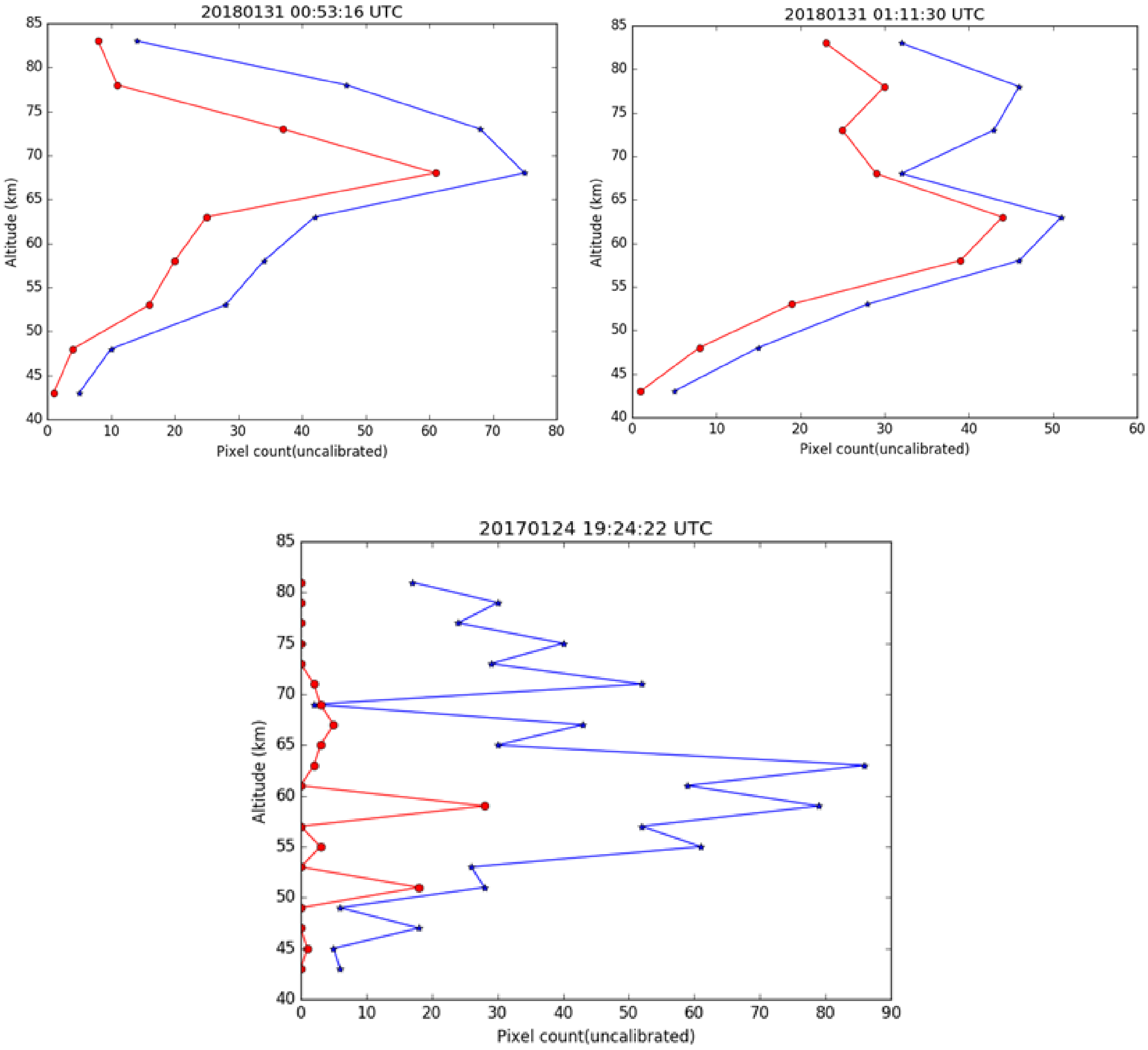
20180131 00:53:16 UTC

20180131 01:11:30 UTC

20170124 19:24:22 UTC

Figure 4.15: The emission profile of events that were simultaneously recorded by the white-light and red-filtered cameras. The red and blue lines show the emission that was recorded by the red-filtered and white-light cameras respectively.The pixel count units were used because the white-light camera was not filtered and thus, the image could not be calibrated using known stars in the star catalogue. Each of the plots represent the emission profile of a single carrot-shaped sprites event observed at different time scale shown above the plot, using filtered and unfiltered cameras.

4.4.3 Estimation of electron fluxes at different altitudes

The flux of the electrons was estimated using the red-filtered data, which are refereed to as the "red images". We first ensured that a given image to be analysed contained at least one of the known stars in the star catalogue. The essence of having known stars on the images was to enable us to relate the flux of a known quantity (the stars) to the sprites images since they were both recorded at the same time, using the same camera gain setting with the same atmospheric loss. We then used similar techniques to those previously used to estimate the emission profile of sprites to derive the pixel values of the sprite events at various altitudes. Finally, we used equation 4.5 to estimate the flux of the electrons within sprites at various altitudes.

$$Sprites_{\text{flux}}(ph/m^2/s) = \frac{Star_{\text{flux}}(Sprites_{\text{avg-brightness}} - Sky_{\text{bg}})}{Star_{\text{avg}} - Sky_{\text{bg}}} \tag{4.5}$$

where:

$\text{Star}_{\text{flux}} = \frac{Star_{\text{power}}(watts/m^2)}{E_{\text{photon}}(watts/ph)}$

Figure 4.16 shows the flux of the electrons at different altitudes for some of the red-filtered sprite events.

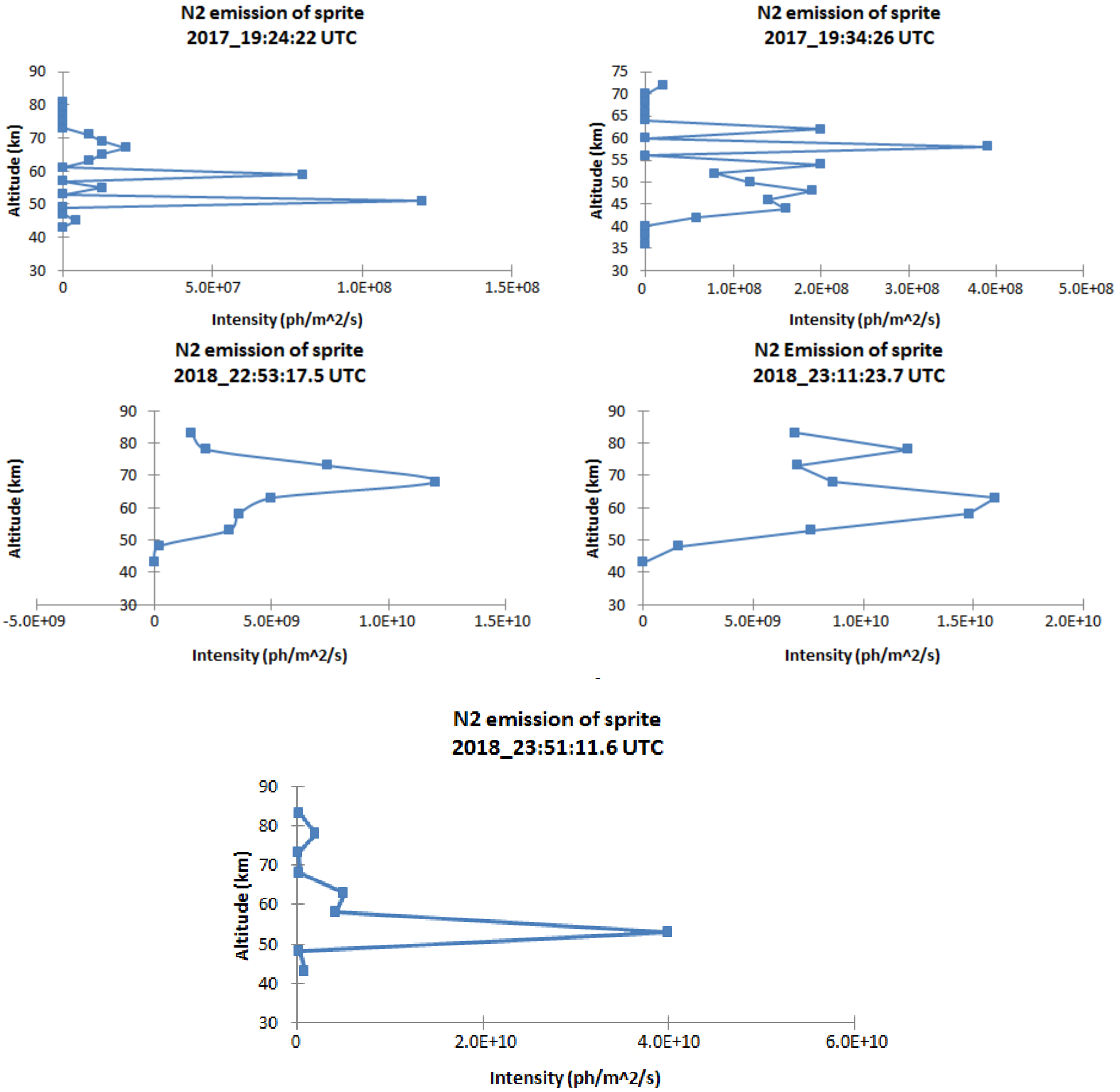

Figure 4.16: The N2 emission profile plot of five sprite events.

These plots suggest that the N2 photon emission within sprites peak between 55 km and 70 km for the events, for which the fluxes of the electrons were estimated. This agrees with other literature(Sentman et al. 1995; Neubert et al. 2001) that suggests that sprites attain their maximum brightness at around 68 km.

4.5 Estimation of characteristic electron energies and electric field strength within sprites

4.5.1 Characteristic electron energies ($\mathbf{Q_o}$)

The characteristic electron energies within sprites were inferred using the Maxwell-Boltzmann distribution function for collisional gases assuming a non-relativistic motion, which is given by:

$$f(v) = \sqrt{\frac{2}{\pi}\left(\frac{m}{KT}\right)^3 v^2 \exp\left(-\frac{mv^2}{2KT}\right)} \tag{4.6}$$

where m is the mass of electron, T is the temperature, K is the Boltzmann constant and v equals the velocity.

Equation 4.6 can be rewritten to derive the energy term as :

$$f(v) = 2\sqrt{\frac{2}{\pi}}\left(\frac{1}{KT}\right)^{\frac{3}{2}}(m)^{\frac{1}{2}}\frac{1}{2}mv^2 \exp\left[-\frac{\frac{1}{2}mv^2}{KT}\right]$$

where energy (Q)

$$Q = \frac{3}{2}KT = \frac{1}{2}mv^2$$

Equation (4.6) can then be rearranged as:

$$f(v) = KQ \exp\left[-\frac{Q}{Q_{\mathrm{o}}}\right] \tag{4.7}$$

where $f(v)$ is the flux of electrons within sprites at different altitudes, K is the constant of proportionality, Q is the energy of the electrons and Q_{o} is the characteristic electron energy.

Since the flux of the electrons producing the red emissions $f(v)_{\mathrm{r}}$ has previously been estimated in this study, we assumed that all the electrons that produced the red and blue photon emissions can be assigned a single energy corresponding to the peak in the collisional excitation cross-section. i.e $Q_{\mathrm{r}} = 10$ eV (Green et al. 1996) and $Q_{\mathrm{b}} = 100$ eV (Gustavsson et al. 2005) respectively. Thus, equation (4.7) was modified to relate to the fluxes of the electrons that could be observed by the red and blue filtered cameras.

$$f(v)_{\mathrm{r}} = KQ_{\mathrm{r}} \exp\left[-\frac{Q_{\mathrm{r}}}{Q_{\mathrm{o}}}\right] \tag{4.8}$$

$$f(v)_{\mathrm{b}} = KQ_{\mathrm{b}} \exp\left[-\frac{Q_{\mathrm{b}}}{Q_{\mathrm{o}}}\right] \tag{4.9}$$

Since we were unable to observe the blue emissions from sprites during these observations, we assumed that the fluxes of electrons that produce the blue emissions were at or below the sensitivity threshold of the camera. We also assumed that every photon that was above the excitation threshold of the camera, produces an electron per collision. However, there are situations where the excited electron de-excite through collisions with other molecules whilst producing no photon. This process is termed quenching and occur as a result of the local atmospheric density and altitude (Ihaddadene and Celestin 2017). These cases were not considered in this study.

We then assumed that the EMCCD camera used for the observations had a linear response. The threshold of the camera was derived using the equation of a straight line.

$$y = mx + c$$

where "y" and "x" are the pixel values and flux of stars that were observed during the observations. The variable "c" is the derived threshold of the camera, which was assigned to $f(v)_{\mathrm{b}}$ in equation 4.9. We finally solved equation (4.8) and (4.9) simultaneously to determine Q_{o} for a given value of $f(v)_{\mathrm{r}}$ at various altitudes. Figure 4.17 shows the scatter plot of Q_{o} as a function of altitude, which suggests that the average Q_{o} for the sprite events was 5.5 eV. We later assigned half of the value of the derived camera sensitivity threshold to blue emissions from sprites $f(v)_{\mathrm{b}}$. The estimated value of the characteristic energy within sprites at various altitudes ranges from 4.8 to 6.4 eV, with an average value of 5.2 eV. This shows that the techniques used for this estimation do not depend entirely on the blue emission data from sprites.

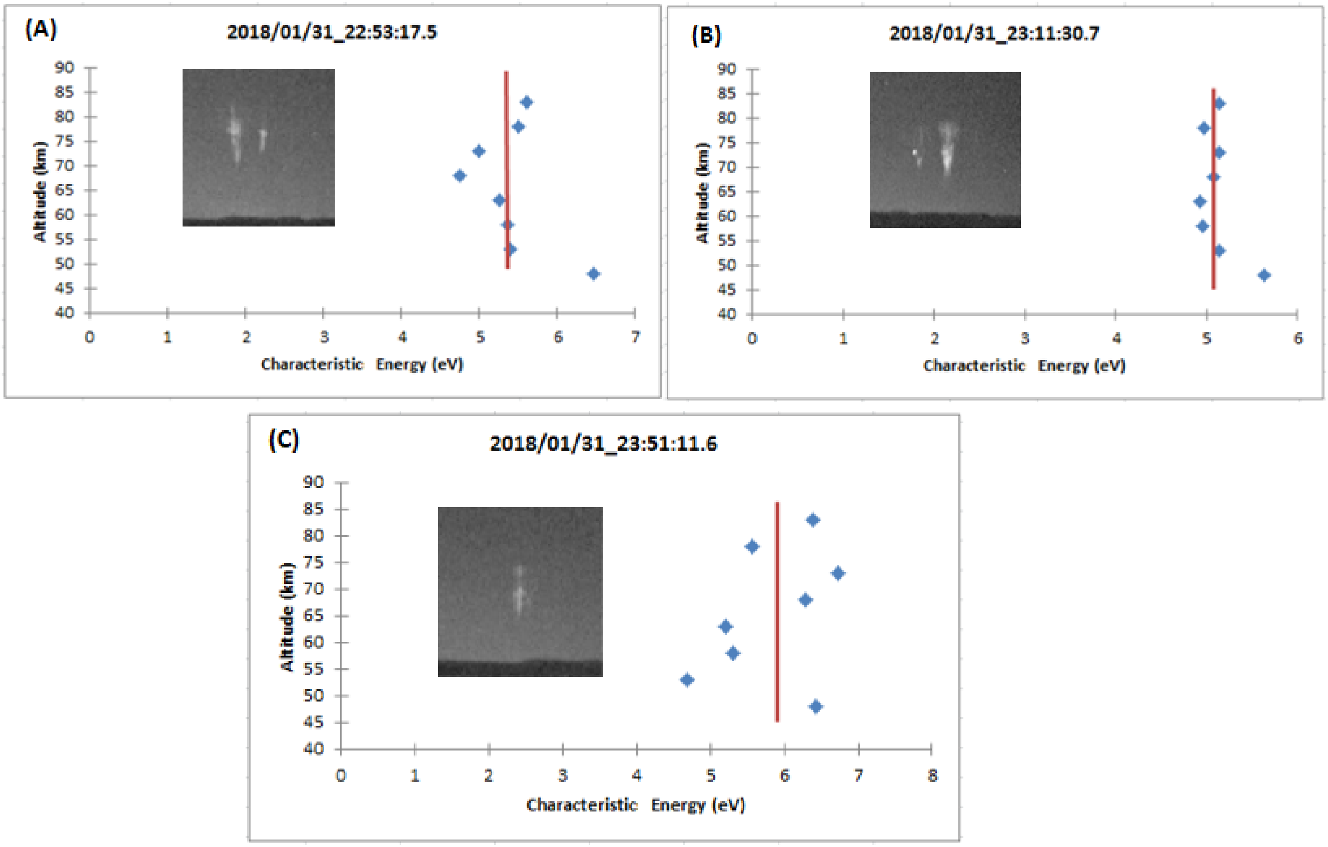

Figure 4.17: The characteristic electron energies as a function of altitude for three observed sprite events. The red bar shows the average Q_o(5.4 eV, 5.1 eV and 5.8eV) of each of these events. The corresponding sprite events are overlaid on the plot. Panel (A), the sprite event on the left was used for the analysis. Panel (B) the sprite event on the right was used for the analysis. These events were chosen because they were brighter on the image. The altitude scale on the plot does not apply to the overlaid sprite image.

4.5.2 Electric field estimation

To estimate the electric field, we assume that the electric field is the only force that was applied to the electrons whilst neglecting the ions.

$$F = ma = Eq \tag{4.10}$$

where F is the force, m is the mass of the electron (9.109 x 10^{-31} kg), a is acceleration, q is the charge of the electrons (1.602 x 10^{-19} coulombs) and E, the electric field. From equation (4.10)

$$E = \frac{q}{ma} \tag{4.11}$$

We assume that the collision between the electrons and neutrals is elastic in nature and the electron motion is non-relativistic. i.e.

$$Q = \frac{1}{2}mv^2 \Rightarrow v = \sqrt{\frac{2Q}{m}} \tag{4.12}$$

and that the electrons started from rest following each collision, i.e.

$$v = at \Rightarrow a = v\nu \tag{4.13}$$

where v is the velocity of the electrons, Q_{o} is the characteristic energy of the electrons at different altitudes, t is the time between collisions of the electron, which is inversely proportional to the collision frequency (ν) of the electrons at various altitudes. The collision frequencies of the electrons at various altitudes has been measured by Benson (1964) and Kane (1959), which suggests that at these altitudes (48, 53, 58, 63, 68, 73 and 78 km), the corresponding collision frequencies (ν) are 5.0×10^7, 1.8×10^7, 9.7×10^6, 2.8×10^7, 1.4×10^7, 5.7×10^6 and $2.4\times 10^6\nu$ (Sec^{-1}) respectively. Substituting equation (4.12) into equation (4.13), we have

$$a = \nu\sqrt{\frac{2Q}{m}} \tag{4.14}$$

The electric field (E(v/m)) can be determined by substituting equation (4.14) into (4.11),

$$E = \frac{q}{\nu\sqrt{2Qm}} \tag{4.15}$$

Equation (4.15) was finally used to determine the strength of the electric field within sprite events as a function of altitude of estimated ν (Benson 1964; Kane 1959) and derived Q_o. The derived values are shown in Figure 4.18.

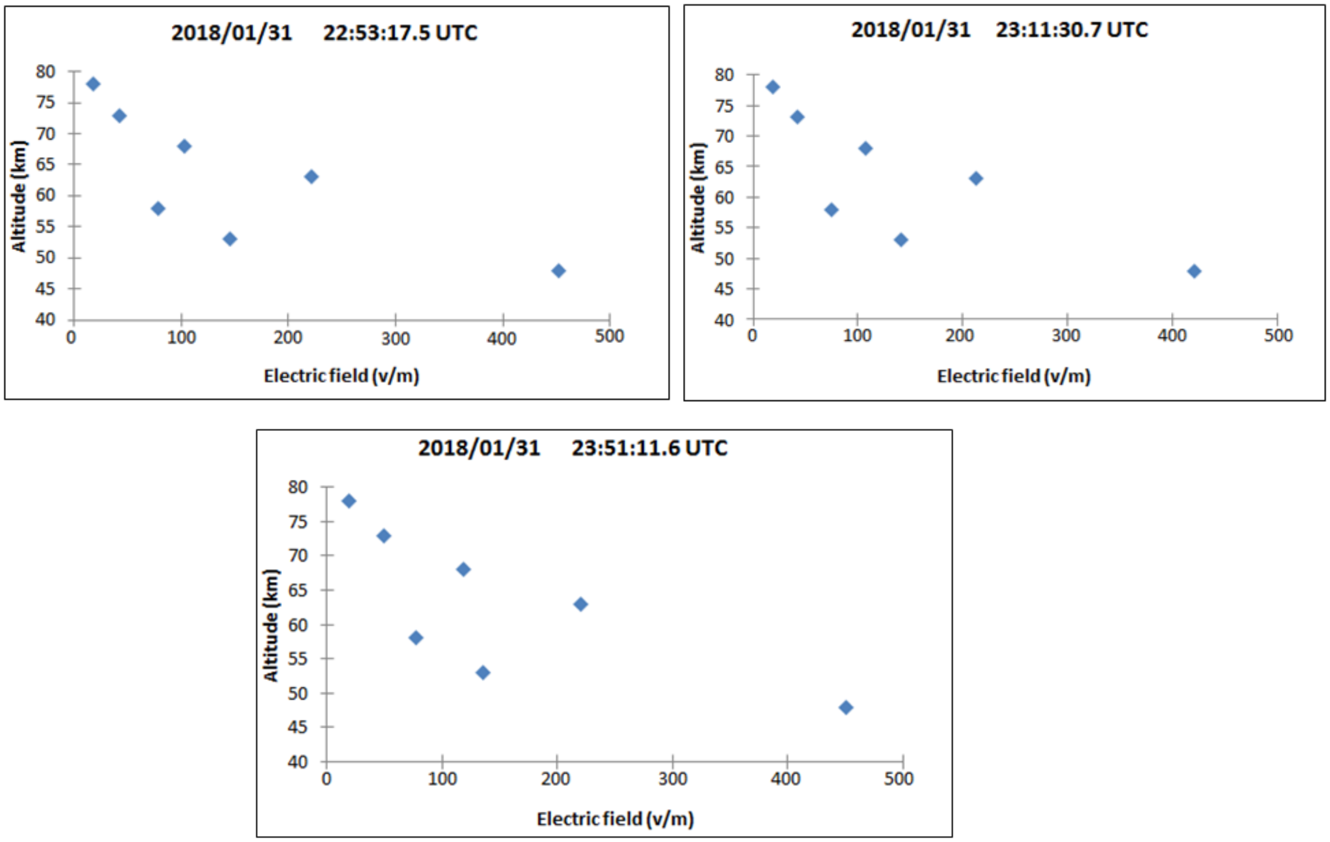

Figure 4.18: The strength of the electric field within sprites at various altitudes for three of the recorded events.

Figure 4.18 shows that, for the sprite events that were analysed, the strength of the electric field within sprite events increases with a decrease in altitude. These plots agree with the conventional breakdown of air in the atmosphere (Figure 1.1) though slightly deviate at 58 and 53 km probabily due to the camera's interlacing effect. The plots also relate to the nominal conventional electric breakdown of pure dry air (Figure 4.19), which was derived using equation 4.16 (Surkov and Hayakawa 2012).

$$E_k = \frac{32N_{\mathrm{m}}}{N_{\mathrm{o}}}(kV/cm^{\text{-1}}) \tag{4.16}$$

where N_{o} is the constant of the order of air number density at ground levelSurkov and Hayakawa (2012), which is equal to $2.7 \times 10\ ^{25}\mathrm{m}^{\text{-3}}$, N_{m} is the number of neutral gases at constant gas temperature T derived from the MSIS-E-90 Atmosphere Model(Papitashvili 2018) for the particular day/time of sprites observations.

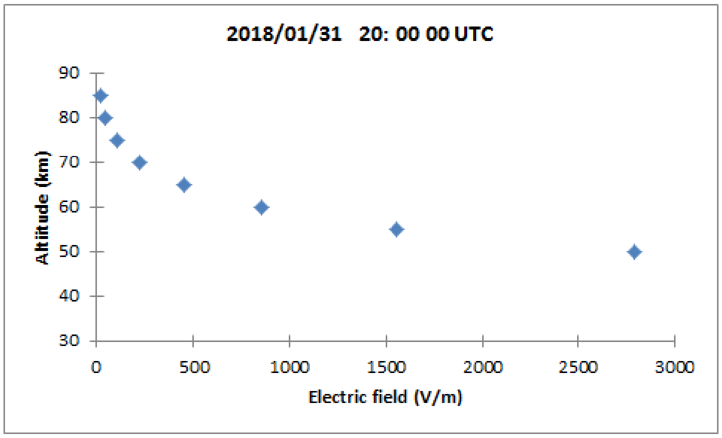

Figure 4.19: The nominal conventional electric breakdown of pure dry air.

The discrepancy between these plots (Figure 4.18) and Figure 1.1 and Figure 4.19, which was consistent at the lower altitude, in all the three analysed events were presumed to result from the series of assumptions that were made in estimating the electric field, the sprites-lightning charge moment change or the camera's interlacing effect on the image frames.

4.6 Charge moment change estimation in sprites

The charge moment change (CMC) is the multiplication of charge and the altitude from where these charges are lowered to the ground. The method that has already been used by a few other researchers(Huang et al. 1999; Matsudo et al. 2007) was used to estimate the charge moment change of the sprite events that were observed.

The waveform data of the ELF signals that were associated with the lightning strikes were obtained from the Schumann Resonance (SR) Station in Hungary (NCK; 47.62^o N, 16.72^o E) during the 2016 sprite campaign. In 2017 and 2018, the SR station in Hungary was not operational. However, the waveform data of the ELF signals were sourced from the Hylaty geophysical station in Poland (49.20^o N,22.54^o E). These systems record both the horizontal magnetic field (H$_{NS}$ and H$_{EW}$) and vertical electric field components of a sprites-producing lightning strike, deduce the source-to-the-station angular distance (θ) in order to determine the charge moment change of the corresponding lightning strike that initiated the sprite events. This processes is well described by Huang et al. (1999) and Mlynarczyk et al. (2015).

The derived CMC values range from 489 C.km to 4331 C.km and were in agreement with the theoretical threshold (500 - 1000 C.km) for dielectric breakdown of the mesosphere (Williams 2010). Figure 4.20 shows a quasi linear relationship between the charge moment change and the observed sprite brightness (Nnadih et al. 2018) for the events recorded in 2016, for which the Schumann Resonance (SR) data and the causative Cloud-to-Ground lightning strike data were available. Figure 4.21 shows the charge moment change for the most-frequently observed sprites morphologies (carrot sprites and column sprites).

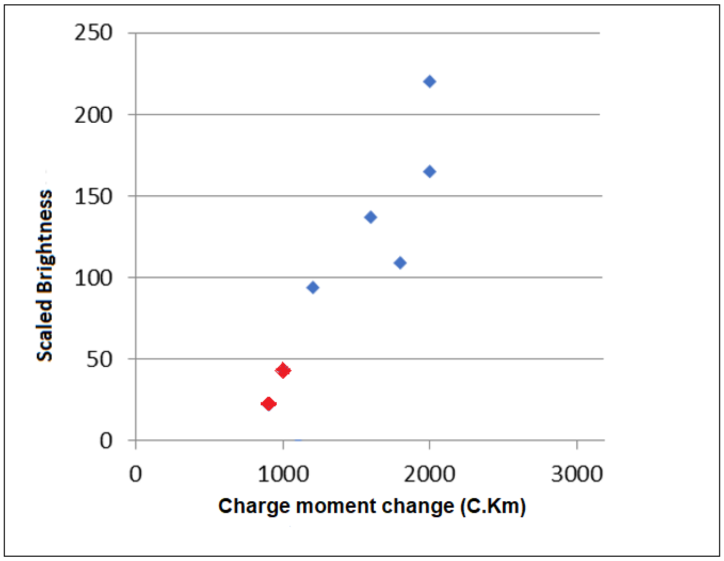

Figure 4.20: The relationship between sprites brightness and the charge moment change (Nnadih et al. 2018) for the events where the Schumann Resonance (SR) data and the causative Cloud-to-Ground lightning strike data were available. The red points are the columniform sprites. The blue points are the carrot-shaped sprites.

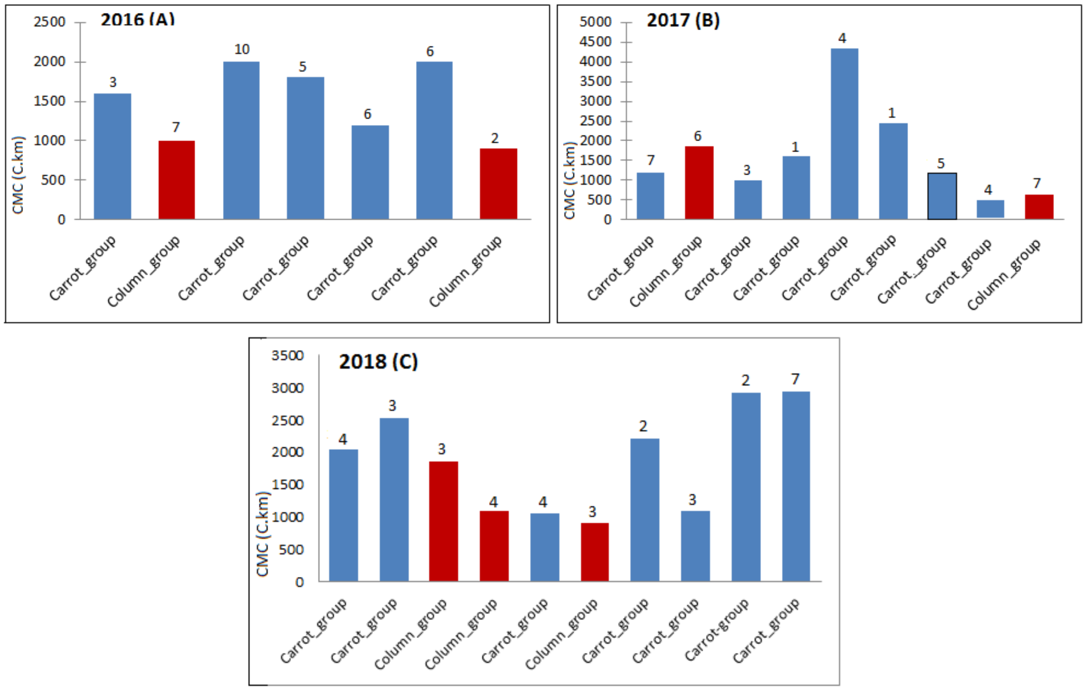

Figure 4.21: The charge moment change for the grouped carrot and column shaped sprite events recorded during the sprite campaigns in 2016("A"), 2017("B") and 2018("C"). The blue bars shows the CMC for the carrot-shaped sprites; the red bars show the charge moment change for the columniform sprites. Each bar represent a sprite's video frame. The number above the bar is the approximate number of sprite events on the frame. The average CMC for the carrot and columniform-shaped sprites was 1874 C.km and 1178 C.km respectively.

These plots (Figure 4.20 and Figure 4.21) show that the larger a given sprites/lightning CMC, the larger the electric field and the brighter the sprites that were triggered by the lightning stroke, as was previously suggested by Yang et al. (2013), and that the carrot-shaped sprites are usually associated with an increase in the charge moment change during their development. Figure 4.21 also suggests that the absence of upward streamers during the development of the column-shaped sprites as observed by high-speed imagery (Stanley 1999) is related to the nature of the charge moment change that triggered the events.

Chapter 5

Discussion and summary

5.1 Discussion

The study shows that the occurrence of sprites-producing convective thunderstorms in central Europe is higher (28 stormy nights in 55 nights of observations) (Bor 2013) when compared to what was observed during this study in southern Africa (5 stormy nights in 65 nights of observations). These observations were made in the summers of 2007–2009 (July–August) in central Europe and December–February (2016 - 2018) in southern Africa. In southern Africa, the thunderstorms had a maximum and minimum frontal extent of over 2000 km (a single night) and approximately 400 km (several nights) respectively and were also smaller in size compared to the convective sprites-producing thunderstorms in the North and South America. However, this comparison depends on the approach for forecasting and the observation conditions in these regions.

The observed thunderstorms in South Africa had an active lightning discharging section that spans between 150 km to 290 km, with an average cloud-top temperature of approximately -52^{o}C, -67^{o}C and -56^{o}C for thunderclouds that were observed in 2016, 2017 and 2018 respectively. The cloud-top temperature of these storms shows that the thunderstorms were around 12 to 14 km above sea level, which corresponds to the approximate height of the storms in the tropics.

During these observations, a total of 113 video clips containing $\sim$ 216 sprite events were recorded. The average detection rate for these sprite events frames was 0.14 sprite events every minute as shown in Table 5.1, which is similar to the finding of Yair et al. (2004) who estimate that the global occurrence rate for sprites is about 0.13 sprites every minute.

Observation date	**No. of video clips containing sprites**	**Observations period (hours)**	**Total No. of events**	**Detection rate (sprites/min)**
11/01/2016	54	3	96	0.3
02/02/2016	4	1	10	0.1
24/01/2017	24	3	44	0.1
06/02/2017	3	1	6	0.1
31/01/2018	28	4	60	0.11
Total	113	12	216	0.142 (average detection rate)

Table 5.1: Detection rate for sprite events over southern Africa.

Whilst 51% of these video clips were recorded using a wide field-of-view lens in 2016, 24% of the events and 25 % of them were recorded using a narrow field-of-view lens during the 2017 and 2018 sprite campaign respectively. The wide and narrow FOV lenses have their respective benefits and disadvantages. For instance, the wide field-of-view lens recorded more sprites whilst compromising the resolution for the events at a distant location, whereas the narrow field-of-view lens records fewer events within its FOV, but with better spatial resolution. Hence, the wide FOV ($43^o\times 33^o$) lens was used during the early stage of the research, in 2016, when the objective was to record as many sprite events as possible, and the narrow FOV ($22^o\times 18^o$) was later used to observe specific events at higher spatial resolution and at multiple wavelengths.

We were not able to determine the precise geo-location of the recorded sprite events because the images were not simultaneously recorded from different observation sites. However, the approximate location of the events was derived by fitting the stars on the images to their catalogue positions. These fits were manually done to a single-pixel resolution to estimate the azimuth, elevation and thence the geographical coordinates (longitude and latitude) of the sprite events. The error in fitting the star positions consists of the star-pixel jitter (1-pixel, equivalent to 0.09 degrees). The error in the estimation of the sprites distance is influenced in part by the assumptions of the sprites top maximum optical observable emission altitude (85 ± 5 km) (Sentman et al. 1995). The process works well when there are many background stars on the images and was used in earlier studies (Nnadih et al. 2018). The derived coordinates for the sprites were matched in position and in time with the coordinates of the nearest large (>10 kA) positive lightning flash as detected by the SALDN. Although in rare cases, sprites are triggered by negative lightning flashes, all the observed sprites in this study were associated with positive CG lightning discharges. Whilst the average lightning peak current that was associated with these sprites was 64 kA; the maximum and minimum peak current values were 191 kA and 11 kA respectively. These events were observed at distances from $\sim$ 429 km to 890 km.

The observed events were visually classified by their morphology, and then by the number of individual sprite events that appeared on a single image. The morphological classification of the sprite events was based on the shape of the event as recorded on the images, which were acquired with a frame rate of 25 Hz. This frame rate is too slow to capture the temporal evolution of sprites, but it is adequate for morphological classification purposes.

This shows that the morphology of the observed sprite events were carrot-shaped, column, tree-like and jelly-fish-shaped. These events were named following the previous notations used in published scientific literature (Winckler et al. 1996; Stanley 1999; Sentman et al. 1995). There were some cases were the recorded structures could not be unambiguously classified into any of these known morphological types because the events were either too dim/blurred due to the source-observer distance or they were so densely packed that the individual events could not be visually resolved. Those structures were regarded as "unclassified" groups. These groups were observed in 24/113 events (23%).

Classifying the events by their number of appearance on a single video frame shows that they can be grouped as single events or multiple (clustered) events. Whilst the single events were observed in 17/113 (15%) frames, the clustered events were recorded in 70/113 frames (62%), which supports previous studies (Sentman et al. 1995; Stanley 1999) that found that sprites tend to appear more often in clusters rather than alone.Valdivia et al. (1997) suggest that the frequent appearance of sprites in groups is caused by the horizontal lightning flashes, which act as a fractal(non-uniform) antenna. During this study, one of the 70 clustered events observed was the special group known as dancing sprites. Sprites are considered to dance across the sky when they appear horizontally on a video clip, in the form of a sequential luminous emission that is displaced in position and in time from each other, creating an impression of motion in the sky. Whilst considering the shape of these clustered groups of sprites, the events were further classified into homogeneous (the same structure on a video frame) and heterogeneous (different structures on a single video frame) groups (Figure 4.7). Homogeneous clustering was observed in 53/70 (76%) of events whereas the heterogeneous clustered were seen in 17/70 (24%) events. This shows that sprites of the same structures seem to appear together than sprites of different shapes.

The morphological categorization also shows that whilst 70% of the observed sprite events were carrot/column sprites, which is known to be the most prevalent shape of sprites, 7% of these events have tree-like and jelly-fish structure, and 23% of them were regarded as "unclassified" for the reason mentioned above. Comparing the CMC of the lightning flash that triggered these often-observed sprites structures (carrot and column) shows that the carrot-shaped events usually have higher CMC than the column-shaped structures, and that the absence of the upward streamers in columniform sprites as reported by high-speed imagery of sprites structures (Stenbaek-Nielsen et al. 2013; Stanley 1999) is related to the nature of the charge moment change that triggered the events, which in most cases is lower than the charge moment change associated with carrot-shaped sprites as shown in this study.

The coordinates (latitude and longitude) of these events that were derived from the sprites analyser software were associated with the location of the lightning discharges with the assumption that sprites are located within 50 km of the causative lightning flash. Whilst 70% of the events were initiated by CG lightning discharge, 3% of them were associated to IC lightning flashes, and the causative lightning flash for 27% of the events was not found in both the lightning dataset of SALDN and ENTLN.

The waveform signals for the IC lightning flashes that triggered 3% of the events were characterised by a longer rise time and peak width than the waveform signals for the CG lightning discharges, which had a shorter rise time and peak width. It was assumed that the events without any detectable lightning discharge could have been triggered by a continuing current in the cloud as reported by a few researchers (Lyons 1996; Neubert et al. 2001) or their parent +CG were flagged as questionable detections, and discarded as in the case of some of the sensors of the lightning detection networks in Europe (Martin Fullekrug 2017, personal communication).

The brightness and flux of the electrons within sprites at different altitudes were estimated by relating the emission of the events to the brightness and flux of a known star in the star catalogue. Since brightness is inversely proportional to the square of the distance, the brightness values obtained were normalised by dividing them by the square of their corresponding distance to the observer. Again, comparing these values to the sprite's lightning charge moment change shows a quasi-linear relationship between the CMC and the sprite's brightness, for the events observed in 2016, for which their corresponding parent lightning discharge and the Schumann resonance data were available. The fluxes of the electrons within sprites at various altitudes, when observed in the wavelength range (635 - 675 nm) peak around 55 to 70 km for the events, for which the fluxes of the electrons were estimated. This result corresponds to previous observations, which shows that sprites achieve their maximum brightness at around 68 km (Sentman et al. 1995; Neubert et al. 2001).

The characteristic electron energies within sprites were estimated using the Maxwell-Boltzmann distribution function for collisional gases with a non-relativistic motion. We assumed that the electrons that produce the red and blue photons can be assigned to a single energy that corresponds to the peak in the collisional excitation cross-sections and that and that the camera detects every photon that is excited by the electron whenever the energy of the photons is above the detection threshold of the camera. We also assumed that since we were not able to record the blue emissions from sprites, the emission was at or below the detection threshold of the camera. The estimation shows that the characteristic electron energy within sprites, for the three events that were analysed, range from 4.7 eV to 6.7 eV. These values are twice those obtained from aircraft measurement(Morrill et al. 2002), they also correspond to satellite-based observation (Kuo et al. 2005). Whilst the aircraft-based estimation uses the blue emission data from sprites, which are absorbed by the atmosphere at aircraft operating altitudes, our estimation assumed that the blue emission from sprites was at the camera threshold. The uncertainty in the characteristic electron energies within sprites that was estimated in this study results from the ambiguity in determining the sprite's altitude emission vertical range, which in our case, was presumed that the emission profile for a typical sprite events spans around 45 km in the vertical. The result of our estimation is consistent with the theoretical studies of sprites streamers (Liu and Pasko 2005).

The strength of the electric field on the electrons was estimated by assuming that the motion of these electrons was non-relativistic and that their collision with neutrals species was also elastic in nature. The estimation shows that the electric field increases with a decrease in altitude. Comparing these results to the altitude profile for dielectric breakdown of the atmosphere (Figure 1.1) shows that whilst at 68 km, the average electric field for the analysed events (Figure 4.17) was 110 V/m, whereas the model shows that the electric field at 68 km is approximately 150 - 200 V/m. At 50 km altitude, our estimation shows that the average electric field is 450 V/m, whereas the model suggests between 500 to 550 V/m at 50 km. The discrepancy in these results could be related to the assumptions that were made in our study and the assumed CMC values in the models.

5.2 Summary

Recognizing the limited data set that were available during the study, we conclude that sprites have been imaged for the first time in southern Africa since the earliest sightings reported anecdotally in 1937. In 5 out of 65 nights of observations, 113 video images containing around 216 sprites were successfully recorded using ground-based systems (Table 5.1). These events comprise various structures (carrot, column, tree-like and jelly-fish shaped sprites) that have been recorded in other parts of the world, and were between 429 - 890 km away from the observer. Comparing the observed storms to a similar sprite campaign in Central Europe (Bor 2013) shows that a few sprites-producing thunderstorms were present during this study, which had an average cloud-top temperature and height of about -58°C and 14 km, respectively.

The recorded sprites images were analysed using the sprites analyser software and the lightning data from both the SALDN and the ENTLN. The maximum and minimum peak amplitude of the causative lightning current that were associated with these events were 191 kA and 11 kA respectively. The sprites lightning CMC was analysed, which shows a quasi-linear relationship between sprites brightness observed in 2016 and the CMC, as earlier suggested by Adachi et al. (2004) and Yaniv et al. (2013), and that the carrot-shaped sprites are usually accompanied by an increase in the CMC when compared to the columniform sprites.

The study showed that the average occurrence rate for sprite events in southern Africa was 0.14 sprite/minutes and that whilst these events frequently appeared in cluster, sprites cluster of the same structure usually appear together rather than sprites cluster of different morphology.

The characteristic electron energies within sprites averaged at various altitudes range from 4.7 eV to 6.7 eV. These values correspond to satellite-based measurement (Kuo et al. 2005), and was also consistent with the theoretical estimation of the sprites streamers model (Liu and Pasko 2005). The strength of the electric field derived within sprites also correlates with the altitude profile for dielectric breakdown of the atmosphere between 50 to 80km.

5.3 Suggestions for future work

Finally, the following suggestions would improve the results presented in this study.

1. **Bistatic observations of sprites.**

   Since the sprites optical data presented in this study were acquired from a single observation site, we were not able to determine the precise geo-location and altitude of the events . However, their approximate position was determined by fitting the stars on the images in the catalogue position and relating the derived coordinate to the position of the corresponding lightning stroke in the LDN data list. The maximum altitude above the thunderstorm was also assumed to be around 85 km, which was used to estimate sprite's emission profile (section 4.4.2) and the fluxes of electrons within sprites when observed in the specific wavelength range (635-675 nm) (section 4.4.3). The accuracy of these results could be improved by observing sprite events simultaneously from two different observation sites. We propose observing sprites simultaneously from SAAO and Carnarvon (Klerefontein Farm). These sites are relatively close to each other thus, the error due to the atmospheric effects such as refraction and scintillation would be significantly reduced, if the distance to sprites from these locations is small. Depending on the position of the sprites-producing thunderstorms described in section 4.2, the viewing geometry shown in Figure 5.1 will be used to determine the accurate position and altitude of sprite events.

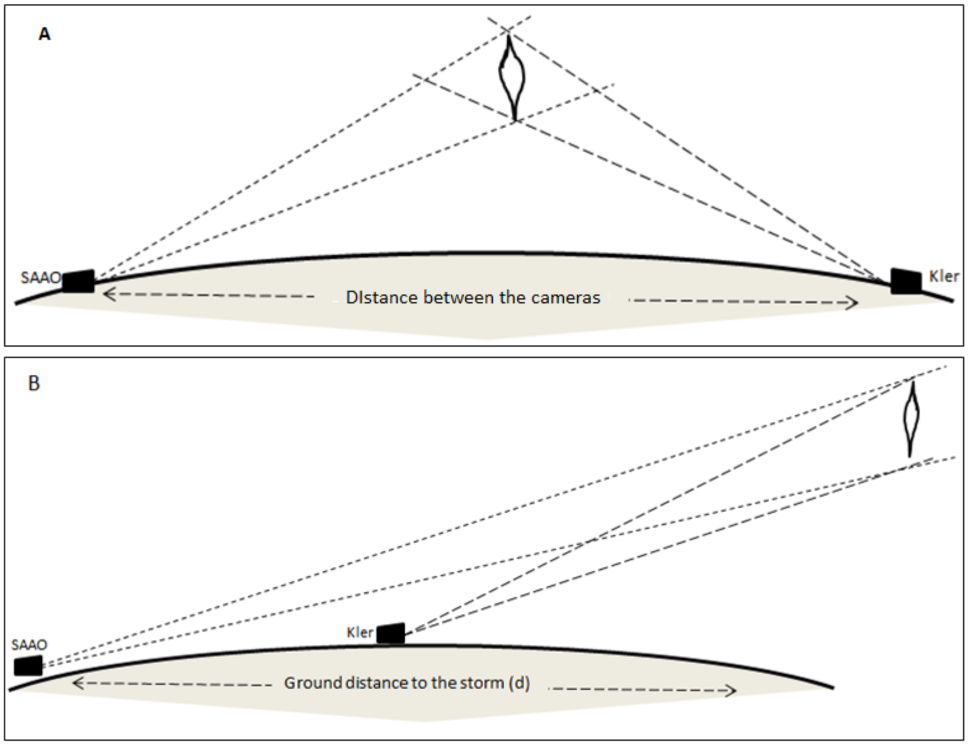

Figure 5.1: Viewing geometry for bistatic observations.

The issue with the proposed viewing geometry is getting the sprites-producing storm to be approximately an equal distance to the two observing points (Panel A) or at a distance that will be visible to the observers at these observing points (Panel B). Since we will not be able to control the position of the thundercloud, we assume that any of these viewing geometries can be used depending on the location of the storm.

As soon as the uncertainty that is associated with the positioning and altitude estimation of sprites is reduced by simultaneously observing sprite events from two locations, we would be able to accurately determine the fluxes of the electrons, the strength of the electric field (section 4.5.2) and the characteristic energy (section

4.5.1) within sprites at various altitudes. Since this study has shown (Figure 4.19) that carrot-shaped sprite events are usually associated with an increase in the charge moment change value when compared to the columniform structures, we could also be able to precisely determine the correlation (if any) between various structures of sprites and their altitude above the thunderstorm. This will provide additional insight to the phenomenology of sprites.

2. **High-speed ground-based imaging of sprites.**
   The data presented in this thesis were obtained using imagers that observed sprite events at 25 fps. Although the 216 recorded sprite events paved the way for more comprehensive observations of sprites from southern Africa, a lot more information could be resolved from sprites by observing their emissions with high-speed imagers. Ground-based observations of sprites using high-speed imagers with sampling frequency between 1000 to 100,000 fps would allow us to resolve the dynamics, spatial and temporal evolutions of sprites. It will also assist us to detect and record the blue emissions of sprites from the sprites-producing thunderstorms that are within 250 to 350 km from the observer since these blue emissions (N2+(1NG)) are very weak due to Rayleigh scattering whilst having optical durations of approximately 5 ms (Heavner et al. 2010). Simultaneous observation of the blue ((N2+(1NG)) and red (N2(2PG)) emission from sprite events will greatly improve our estimations of the characteristic electron energies and electric field strength within sprites using the methodology presented in this study.

We also note that the techniques developed in the course of this study can as well be used to validate data from the ongoing (ASIM mission on the ISS) (Neubert and et al. 2019) and the proposed space-based observations (French satellite - TARANIS) (Pincon and et al. 2011) of TLEs.

Appendices

Appendix A

Meteosat infrared imagery temperature look-up table

Colour	Enhancement				Count values					
	8-bit Brightness		Temp		Blue		Green		Red	
	Min	Max	Min	Max	Min	Max	Min	Max	Min	Max
Grey	0	173	57	-29.5	0	255	0	255	0	255
Yellow	174	181	-30	-36	0	0	255	100	255	100
Red	182	189	-37	-44	0	0	0	0	100	255
Magentas	190	197	-45	-52	255	100	0	0	255	100
Cyans	198	205	-53	-60	100	255	100	255	0	0
Green	206	213	-61	-68	0	0	255	100	0	0
Blue	214	221	-69	-78	255	100	0	0	0	0

Table A.1: Meteosat inferred imagery conversion look-up table (Adapted from The COMET Program, MeteoSat 2018.

Appendix B

Catalogue of observed sprite video clips

Tables B.1, B.2 and B.3 list all the events that were observed during the 2016, 2017 and 2018 sprite campaigns respectively. Since these sprite events were not simultaneously observed from multiple observing sites, we were not able to determine their location accurately. However, their approximate coordinates were estimated and these are presented in the tables. Where the causative lightning discharges were not available from both the SALDN and the ENTLN, we were not able to determine the position of the events unambiguously and hence, the cloud-top temperature was not estimated.

Table B.1: Sprite events observed in 2016. The events observed on the 2nd of February 2016 were recorded through a glass door. Thus, we were not able to analyse these events because of the reflection of light on the images from the computer screen.

Sprite initiation time (UT) and coordinates Lat/Long		Lightning strike locations Lat/Long	Peak current (kA)	Offset (km) between sprite and lightning strike	Ground range from SAAO (km)	Charge moment change (C.km)	Mean brightness (arbitrary units)
11th January 2016							
18:53:49.4	25.3024 -31.7954	25.3401 -31.8200	37	5	429	-	4.25×10^{-4}
18:59:09.5	25.6347 -31.8300	25.5448 -31.9019	82	12	462	-	2.65×10^{-5}
19:10:04.6	24.8808 -28.1392	- -	-	-	612	1100	6.97×10^{-8}
19:12:54.9	24.3084 -28.4995	24.3175 -28.5099	29	2	547	-	2.33×10^{-6}
19:17:09.8	24.5073 -28.1307	24.7613 -28.1460	23	25	570	-	3.35×10^{-6}
19:22:25.3	24.0999 -28.5828	24.0152 -28.5189	97	11	537	1600	4.75×10^{-6}
19:23:10.0	23.4682 -28.3421	23.4040 -28.3151	66	7	516	-	3.43×10^{-6}
19:27:15.5	24.2038 -28.7308	- -	-	-	520	-	5.47×10^{-6}
19:28:34.2	23.5125 -28.2842	23.4345 -28.2995	69	8	524	-	3.01×10^{-6}
19:30:07.4	24.9510 -27.7642	24.7704 -27.8367	12	21	649	-	1.75×10^{-6}
19:33:06.8	24.2423 -28.1746	- -	-	-	572	-	2.13×10^{-6}
19:33:24.0	24.8765 -27.8765	24.7929 -27.8783	189	9	635	-	5.12×10^{-6}
19:34:46.6	24.8765 -27.7398	23.7861 -27.4338	55	35	583	-	1.62×10^{-6}

Sprite initiation time (UT) and coordinates Lat/Long		Lightning strike locations Lat/Long	Peak current (kA)	Offset (km) between sprite and lightning strike	Ground range from SAAO (km)	Charge moment change (C.km)	Mean brightness (arbitrary units)
11th January 2016							
19:36:07.3	24.1841 -28.3945	- -	-	-	549	-	4.90×10^{-6}
19:38:32.5	23.5757 -27.5451	23.5498 -27.5378	48	3	600	1000	1.21×10^{-6}
19:39:35.3	26.5030 -27.8099	- -	-	-	747	-	8×10^{-9}
19:40:15.4	24.3912 -28.0973	- -	-	-	587	-	3.03×10^{-6}
19:48:05.3	25.0053 -28.0583	25.0333 -27.7024	93	40	627	-	2.32×10^{-6}
19:49:19.7	24.4021 -28.0632	- -	-	-	591	1500	2.65×10^{-6}
19:49:54.3	26.7969 -27.5946	27.0356 -27.4784	57	29	784	-	3.54×10^{-7}
19:52:23.9	24.4145 -28.1858	24.0780 -28.2561	87	38	602	-	4.56×10^{-6}
19:52:35.4	26.9646 -27.8676	- -	-	-	776	4700	3.18×10^{-6}
19:55:08.1	24.4354 -27.5697	24.4551 -27.5364	91	4	639	-	1.06×10^{-6}
19:56:58.9	24.5887 -27.9368	- -	-	-	613	-	2.20×10^{-6}
19:58:01.3	27.0188 -27.6672	27.0492 -27.6776	42	3	795	-	1.44×10^{-6}
19:58:29.6	24.8720 -27.8516	25.1202 -27.6913	11	28	637	1800	2.68×10^{-6}

Sprite initiation time (UT) and coordinates Lat/Long		Lightning strike locations Lat/Long	Peak current (kA)	Offset (km) between sprite and lightning strike	Ground range from SAAO (km)	Charge moment change (C.km)	Mean brightness (arbitrary units)
11th January 2016							
20:01:24.0	24.1773 -28.3431	- -		-	553	-	7.96×10^{-6}
20:03:32.5	26.7051 -27.7585	26.7221 -27.3040	37	51	765	-	1.71×10^{-6}
29:05:02.6	24.1703 -28.0736	- -	-	-	578	-	5.86×10^{-6}
20:07:43.4	24.7642 -28.84874	- -	-	-	545	-	2.63×10^{-6}
20:08:03.3	24.1425 -28.2888	23.9417 -28.2424	88	20	556	-	3.33×10^{-6}
20:09:25.3	23.5002 -28.2749	23.6325 -27.9044	71	40	548	1200	3.13×10^{-6}
20:10:04.9	24.1268 -28.2749	23.9624 -28.2622	101	18	557	-	7×10^{-6}
20:11:51.2	25.0633 -27.7316	- -	-	-	637	-	2.03×10^{-6}
20:14:02.2	24.7353 -27.3453	24.6316 -27.2807	105	13	644	-	7.3×10^{-7}
20:16:22.7	27.2402 -27.6185	27.0816 -27.6647	26	16	815	-	2.55×10^{-6}
20:18:46.4	24.5685 -28.4006	24.8348 -28.0621	104	46	639	2000	5×10^{-6}
20:19:42.3	27.2746 -27.7756	- -	-	-	805	-	5.4×10^{-6}
20:22:27.8	23.9542 -27.9267	23.9375 -28.2608	33	34	542	-	3.11×10^{-6}

Sprite initiation time (UT) and coordinates Lat/Long		Lightning strike locations Lat/Long	Peak current (kA)	Offset (km) between sprite and lightning strike	Ground range from SAAO (km)	Charge moment change (C.km)	Mean brightness (arbitrary units)
11th January 2016							
20:24:43.7	24.4635 -27.4314	24.6346 -27.5543	191	22	640	-	3.72×10^{-6}
20:26:21.9	27.8017 -27.4314	27.5728 -27.5507	177	26	829	-	1.58×10^{-6}
20:27:34.7	24.2481 -27.7547	24.6414 -27.4252	20	17	612	-	3.25×10^{-6}
20:29:53.8	24.6414 -27.4252	24.6573 -27.5065	126	8	627	2000	4.20×10^{-6}
20:32:46.0	27.3154 -27.9365	- -	-	-	796	-	8.9×10^{-6}
20:33:19.2	24.2790 -27.6155	23.9460 -27.5698	101	33	605	-	3.80×10^{-6}
20:35:37.2	24.2840 -27.7041	- -	-	-	618	-	3.19×10^{-6}
20:38:43.4	27.3937 -27.6200	27.4279 -27.5663	85	7	804	-	1.08×10^{-6}
20:46:42.3	28.0412 -28.0546	27.7280 -27.9726	87	32	795	-	2.20×10^{-6}
21:01:08.0	23.9499 -26.7322	23.9083 -26.4024	48	40	698	-	8×10^{-7}
21:29:05.4	24.8736 -26.8661	25.0126 -26.7303	46	21	728	900	4.1×10^{-7}
21:33:49.1	25.0884 -26.6717	25.0916 -26.7336	159	7	758	-	2.42×10^{-6}

Sprite initiation time (UT) and coordinates Lat/Long		Lightning strike locations Lat/Long	Peak current (kA)	Offset (km) between sprite and lightning strike	Ground range from SAAO (km)	Charge moment change (C.km)	Mean brightness (arbitrary units)
11th January 2016							
21:36:06.5	27.4001 -27.2624	27.4186 -26.8319	31	48	806	-	1.14×10^{-6}
21:41:24.3	27.2281 -27.8010	- -	-	-	800	-	2.24×10^{-6}
2nd February 2016							
18:51:08.8	- -	- -	- -	- -	- -	- -	-
19:05:55.7	- -	- -	- -	- -	- -	- -	-
19:16:55.8	- -	- -	- -	- -	- -	- -	-
19:22:16.3	- -	- -	- -	- -	- -	- -	-

Table B.2: Sprite events observed in 2017. We were not able to determine the CMC of some of the events that had noisy signals.

Sprite initiation time (UT) and coordinates Lat/Long		Lightning strike locations Lat/Long	Peak current (kA)	Offset (km) between sprite and lightning strike	Ground range from SAAO (km)	Charge moment change (C.km)	Cloud-top temperature (°C)
24th January 2017							
18:49:42.080	22.0759 -25.8534	22.0400 -25.6451	44	23	737	1646	-65
18:54:01.688	22.2013 -25.9532	22.1028 -25.8255	12	17	728	1179	-65
19:02:33.856	21.8578 -25.5619	21.8177 -25.5520	77	4	766	1849	-73
19:04:54.946	22.1998 -25.8624	22.1340 -25.8309	45	7	738	990	-65
19:11:26.705	21.5286 -24.8713	21.8265 -24.8047	117	30	839	1611	-73
19:24:22.899	22.1983 -24.8649	22.1839 -24.8221	13	5	742	4331	-57
19:28:23.956	21.4564 -24.8649	21.3448 -24.8221	164	12	840	2440	-73
19:34:26.950	22.1054 -25.5180	22.3302 -25.1875	21	42	774	-	-65
19:39:51.081	22.2440 -25.1583	22.3230 -25.1732	37	8	816	1969	-65
19:40:34.628	21.3698 -24.6886	21.3654 -24.7952	67	11	887	714	-73
19:44:14.467	22.2297 -25.0544	22.3496 -25.1550	36	16	827	-	-65
19:44:44.854	21.3738 -24.7811	21.3775 -24.7801	31	0.4	886	-	-73
19:47:42.961	22.0363 -25.1257	22.2277 -25.2309	115	23	817	1190	-65

Sprite initiation time (UT) and coordinates Lat/Long		Lightning strike locations Lat/Long	Peak current (kA)	Offset (km) between sprite and lightning strike	Ground range from SAAO (km)	Charge moment change (C.km)	Cloud-top temperature (°C)
20:04:16.553	22.0684 -25.2295	22.4860 -25.3545	38	47	806	497	-65
20:10:14.541	22.4943 -25.4496	- -	-	-	788	-	-
20:19:30.735	22.4552 -25.3236	22.5331 -25.2900	86	9	802	-	-57
20:54:53.458	22.6220 -27.9248	22.8219 -27.9345	46	22	774	641	-65
2nd February 2017							
18:00:53.604	24.1613 -30.6416	- -	-	-	371	-	-
18:04:15.047	24.6164 -30.3931	- -	-	-	423	-	-
18:09:57.687	24.1946 -30.3669	- -	-	-	371	-	-
19:24:22.945	24.6254 -30.3571	- -	-	-	371	-	-

Table B.3: Sprite events observed in 2018. We were not able to determine the CMC of some of the events that had noisy signals.

Sprite initiation time (UT) and coordinates Lat/Long		Lightning strike locations Lat/Long	Peak current (kA)	Offset (km) between sprite and lightning strike	Ground range from Carnarvon (km)	Charge moment change (C.km)	Cloud-top temperature (°C)
31st January 2018							
20:19:14.720	26.3562 -29.2378	26.2460 -29.3299	52	15	498	872	-45
21:04:37.584	26.6013 -29.3791	26.5806 -29.1894	42	19	478	2042	-37
21:11:00.255	26.5921 -29.3484	26.7134 -29.3639	80	13	479	2534	-37
21:37:00.397	26.4902 -29.0322	26.5258 -29.8160	55	22	485	1864	-41
22:23:20.660	26.8817 -28.5677	- -	-	-	543	-	-
22:29:01.852	28.5369 -29.2528	28.4658 -29.0794	44	19	659	-	-41
22:30:19.776	27.1596 -28.9463	- -	-	-	547	-	-
22:46:21.392	27.6515 -29.0312	27.6546 -28.9612	43	7	587	1089	-45
22:53:17.054	27.1609 -28.5989	27.4472 -28.5044	45	30	565	-	-49
22:56:45.043	27.0792 -28.2766	- -	-	-	577	-	-
22:58:57.802	27.8705 -29.0951	27.8371 -28.8870	100	21	604	902	-49
23:14:38.151	28.0674 -29.1515	- -	-	-	620	-	-
23:04:54.574	27.4060 -29.1504	- -	-	-	560	-	-

Sprite initiation time (UT) and coordinates Lat/Long		Lightning strike locations Lat/Long	Peak current (kA)	Offset (km) between sprite and lightning strike	Ground range from Carnarvon (km)	Charge moment change (C.km)	Cloud-top temperature (°C)
23:07:08.464	27.4665 -29.2048	28.1103 -29.1108	52	11	563	600	-41
23:11:30.487	27.4423 -28.6788	27.2272 -28.4541	43	32	585	2214	-41
23:21:33.836	27.3443 -28.3260	27.3903 -28.2951	64	5	596	1090	-49
23:29:39.864	27.3844 -28.3920	- -	-	-	595	-	-
23:36:54.914	28.0903 -28.8074	28.0297 -28.6692	53	15	636	2920	-41
23:39:02.560	27.3612 -28.1514	- -	-	-	607	-	-
23:41:46.809	27.9791 -28.7646	28.0790 -28.7703	32	11	628	-	-41
23:42:49.741	27.2078 -28.0991	27.2869 -27.9566	52	16	598	1561	-49
23:51:11.441	27.6062 -27.9933	- -	-	-	638	-	-
23:54:42.562	27.4390 -28.0200	27.1615 -28.1344	84	32	622	683	-41
23:57:33.314	28.4048 -28.6851	28.3994 -28.4964	26	18	670	-	-45
23:57:33.724	27.7237 -28.7722	27.7998 -28.7269	78	10	605	1336	-41
00:01:42.063	27.7001 -27.9357	- -	-	-	648	-	-

Sprite initiation time (UT) and coordinates Lat/Long		Lightning strike locations Lat/Long	Peak current (kA)	Offset (km) between sprite and lightning strike	Ground range from Carnarvon (km)	Charge moment change (C.km)	Cloud-top temperature (°C)
00:09:45.265	27.6375 -27.9667	27.7907 -27.9366	60	30	641	-	-41
00:25:21.237	27.8159 -27.4170	27.5954 -27.4506	51	25	690	724	-41
00:31:49.290	27.7697 -28.6875	28.0073 -28.6034	83	27	613	669	-45
00:48:35.895	27.9296 -28.5267	28.2981 -28.5420	68	41	635	2197	-49
00:53:16.996	27.1609 -28.5989	27.4472 -28.5044	45	30	565	-	-49
00:56:45.003	27.1609 -28.2766	- -	-	-	577	-	-49
01:11:54.811	27.0792 -27.5534	27.3564 -27.5955	49	5	648	385	-41

References

Abarca, S. F., Corbosiero, L. K., Galarneau Jr, T. J. An evaluation of the World-Wide Lightning Location Network (WWLLN) using the National Lightning Detection Network (NLDN) as ground truth. Journal of Geophysical Research, 115:D18206, 2010.

Adachi, T., Fukunshi, H., Takahashi, Y., Sato, M. Role of the EMP and QE in the generation of columiform sprites. Geophysical Research. Letter, 31:L04107, 2004.

Admirat, P., Goyer, G. G., Wojtiw, L., Carte, E. A., and et al. A comparative study of hail storms in Switzerland, Canada and South Africa. Journal of Climatology, 5:35, 1985.

Andor-Technology, ixonem+ 897 (back-illuminated). Technical report, Andor Technology 2008. Available at `https://biochimie.umontreal.ca/wp-content/uploads/sites/37/2015/12/Andor-EMCCD-iXon897.pdf`.

Armstrong, R. A., Shorter, J. A., Taylor, M. J., Suszcynsky, D. M., and et al. Photometric measurements in the SPRITES '95 and '96 campaigns: nitrogen second positive and first negative emission. Journal of Atmospheric and Solar Terrestrial Physics, 60:787, 1998.

Ashley, W. S., Mote, T. L., Grady, P., Trotter, S. L., and et al. Distribution of mesoscale convective complex rainfall in the United States. Monthly Weather Review, 131:3003, 2003.

Ashmore, S. E. Unusual lightning. Weather, 5:331, 1950.

Astroshop, Watec camera WAT-910HX-RC videokamera. 2018. `https://www.astroshop.eu/astronomical-cameras/watec-camera-wat-910hx-rc-videokamera/p,33009`.

Barrington-Leigh, C. P. Identification of sprites and ELVES with intensify video and broadband array photometry. Journal of Geophysical Research., 106:1741, 2001.

Barrington-Leigh, C. P. and Inam, U. S. Sprites triggered by negative lightning discharges. Journal of Geophysical Research Letters., 26:3605, 1999.

Bell, T. F., Reising, S. J., and Inan, U. S. Intense continuing currents following positive cloud- to-ground lightning associated with red sprites. Geophysical Research Letters, 25:1285, 1998.

Benson, R. F. Electron collision frequency in the Ionospheric D Region. Radio Science Journal of Research, 68D:10, 1964.

Bhavika, B. The influence of terrain elevation on lightning density in South Africa. Master's thesis, University of Johannesburg, 2007.

Blamey, R. C., and Reason, C. J. Mesoscale convective complexes over southern Africa. American Meteorological Society, 25:754, 2012.

Blanc, E., Farges, T., Roche, R., Brebion, D., and et al. Nadir observations of sprites from the International Space Station. Journal of Geophysical Research.109:A02306, 2004.

Boccippio, D. J., Williams, E. R., Heckman, S. J., Lyons, W. A., and et al. ELF Transient and positive ground strokes. Science, 269:1088, 1995.

Bor, J. Optically perceptible characteristics of sprites observed in Central Europe in 2007-2009. Journal of Atmospheric and Solar Terrestrial Physics, 92:151, 2013.

Bor, J., Satori, G., and Betz, H. D. Observation of TLEs in Central Europe from Hungary supported by

LINET. In Coupling of Thunderstorms and Lightning Discharges to Near-Earth Space: Proceedings of the Workshop Corte (France), volume 1118, page 73, 2009.

Boys, C. V. Progressive lightning. Nature., 118:749, 1926. Brooks, C. E. The distribution of thunderstorms over the globe. Geophys. Memo, 3:147, 1925.

Bui, V., Lin-Ching, C., and Heckman, S. A performance study of Earth Networks Total Lightning Network (ENTLN) and World-Wide Lightning Location Network (WWLLN). International Conference on Computational Science and Computational Intelligence, 108(D1), 2015.

Burgesser, R. E. Assessment of the World Wide Lightning Location Network (WWLLN) detection efficiency by comparison to the Lightning Imaging Sensor. Quarterly Journal of the Royal Meteorological Society, 143:2809, 2017.

Campbell, K. SA space scientists in the hunt for the elusive sprite, 2014. URL. `http://www.engineeringnews.co.za/article/sa-space-scientists-in-the-hunt-for-the-elusive-sprites-2014-11-28/rep_id:4136`.

Carte, A. E. Morphology of persistent storms in the transvaal on 16-17 October 1981. Beitrage zur Physik der Atmosphare, 54:86, 1981.

Chen, A. B., Kuo, C., Lee, Y., Su, H., and et al. Global distributions and occurrence rates of transient luminous events. Journal of Geophysical Research, 113:A08306,2008.

Chern, J. S., Wu, A. M., and Lin, S. F. Lessons learned from FORMOSAT-2 mission operations. Acta Astronautica., 59:344, 2006.

Christian, H. J., Blakeslee, J. R., Boccippio, J. D., Boeck W. L., and et al., Global frequency and distribution of lightning as observed from space by the Optical Transient Detector. Journal of Geophysical Research, 108(D1):4005, 2003.

Collier, A. B., Hughes, A. R. W., Lichtenberger, J., and Steinbach, P. Seasonal and diurnal variation of lightning activity over southern Africa and correlation with European whistler observations. Annales Geophysicae, 24:529, 2006.

Cooray, V. An introduction to Lightning. Number 71. Springer, 2014.

Corliss, W. R. Hand book of unusual natural phenomena. Anchor Books/Doubleday,Garden City, New York, 423, 1977.

Cotton, M. Bandpass filter selection guide. Technical report. Andover Corporation. Available at `https://www.andovercorp.com/products/bandpass-filters/bandpass-filter-selection-guide/`. 2010.

Cummer, S. A. ELF radiation produced by electrical currents in sprites. Geophysical Research Letters., 25:1281, 1998.

Cummer, S. A., and Fullekrug, M. Unusually intense continuing current in lightning produces delayed mesospheric breakdown. Geophysical Research Letters, 28:495,2001.

Cummins, K. L. and Murphy, M. J. An overview of lightning locating systems: History, techniques, and data uses, with an in-depth look at the U.S. NLDN. IEEE Transactions on Electromagnetic Compatibility, 51:3, 2009.

Davidson, J. E. Thunderstorm and Auroral phenomena. Nature, 47:582, 1893.

Der Velde, A. O., Mika, A., Soula, S., Haldoupis, C., and et al. Observations of the relationship between sprite morphology and in-cloud lightning processes. Journal of Geophysical Research, 111:D15203, 2006.

Dowden, R. L., Brundell, B., and Rodger J. C., VLF lightning location by time of group arrival (TOGA) at multiple sites. Journal of Atmospheric and Solar-Terrestrial Physics, 64:817, 2002.

Durkee, J. D., and Mote, T. L. A climatology of warm-season mesoscale convective complexes in subtropical South America. International Journal of Climatology, 30:418, 2009.

Earth Network Total Lightning Network Data Feed User manual Version 3.0. Available at `https://support.earthnetworks.com/resource/ENTLNLightningDataFeedvICDUM`.

Ebert, U. Review of recent results on streamer discharges and discussion of their relevance for sprites and lightning. Journal of Geophysical Research, 115, 2010.

Eumetsat. Monitoring weather and climate from space, 2016. URL `http://www.eumetsat.int/website/home/index.html`.

Everett, W. H. Rocket lightning. Geophysical Research Letters, 68:599, 1903.

Franz, C. R., Nemezek, J. R., and Winckler, J. R. Television image of large upward electrical discharge above a thunderstorm system. Science., 249:48, 1990.

Frey, H. U., Mende, S. B., Harris, S. E., Heetderks, H., and et al. The Imager for Sprites and Upper Atmospheric Lightning (ISUAL). Journal of Geophysical Research: Space Physics, 121:8134, 2016.

Fullekrug, M., Mezentsev, A., Soula, S., and van der Velde, O., and et al. Sprites in low-frequency radio noise. Geophysical Research Letters., 40:2395, 2013.

Gamero, W. R., Cummer, S. A., Li, J., Stenbaek-Nielsen, H. C., and et al. Comparison of sprite initiation altitudes between observations and model. Journal of Geophysical Research Letters, 116:A02317, 2011.

Gerken, E. A., Inan, U. S., Barrington-Leigh, C. Telescopic imaging of sprites. Geophysical Research Letters, 27:2637, 2000.

Gijben, M. The lightning climatology of South Africa. South African Journal of Science, 108(3/4):1,2012.

Gill, T. Initial steps in the development of a comprehensive lightning climatology of South Africa. Master's thesis, University of the Witwatersrand, 2008.

Green, B. D., Fraser, M. E., Rawlins, W. T., Jeong, L., and et al. Molecular excitation in sprites. Journal of Geophysical Research, 23:2161, 1996.

Groenendaal, H. Van De. SA weather service introduces real-time display. Vector,5:68, 2007.

Gustavsson, B., Sergienko, T., Kosch, M. J., Rietveld, M. T., and et al. The electron energy distribution during HF pumping a picture painted with all colors. Annales Geophysicae, 23:1747, 2005.

Hampton, D. L., Heavner, M. J., Wescott, E. M., and Sentman, D. D. Optical spectral characteristics of sprites. Journal of Geophysics Research letters, 23:89,1996.

Hardman, S. F., Richard, D., James, B., John, B., and et al. Sprite observation in the northern territory in Australia. Journal of Geophysics Research letters, 105:468,2000.

Heavner, M. J. Optical spectroscopic observations of sprites, Blue Jets, and ELVES: Inferred microphysical processes and their macro-physical implications. PhD thesis,University of Alaska Fairbanks, 2000.

Heavner, M. J., Morrill, J. S., Siefring, C., Sentman, D. D., and et al. NUV/Blue spectral observations of sprites in the 320-460 region:N2 (2PG) emissions. Journal of Geophysical Research, 2010.

Hiraki, Y., Kasai, Y., and Fukunishi, H. Chemistry of sprite discharges through ion-neutral reactions. Atmospheric chemistry and physics, 8, 2008.

Holzworth, B. World-Wide Lightning Location Network, 2018. `http://wwlln.net/`.

Houze, R. A. Mesoscale convective systems. Reviews of Geophysics, 42:RG4003, 2004.

Hu, W. Lightning charge moment changes for the initiation of sprites. Geophysical Research Letters, 29:8, 2002.

Huang, E., Williams, E., Boldi, R., Heckman, S., and et al. Criteria for sprites and ELVES based on Schumann Resonance observations. Journal of Geophysical Research,104:16943, 1999.

Hutchins, M. L., Holzworth, R. H., Brundell, B. J., and Rodger, J. C. Relative Detection efficiency of the World Wide Lightning Location Network. Radio Science, 47:2344, 2012.

Hutchins, M. L., Holzworth, R. H., Virts, S. K., Wallace, J. M., and et al. Radiated VLF energy differences of land and oceanic lightning. Geophysical Research Letter, 40:2390,2013.

Ignaccolo, M., Farges, T., Mika, A., Allin T. H., and et al. The planetary rate of sprite events. Geophysical Research Letters, 33, 2006.

Ihaddadene, M., and Celestin, S. Determination of sprite streamers altitude based on N2 spectroscopic analysis. Journal of Geophysical Research: Space Physics, 122:1000, 2017.

Jayaratne, E. R. Temperature gradients in ice as a charge generation process in thunderstorm. Atmospheric Research., 29:247, 1984.

Jayaratne, E. R., and Saunders, C. P. The rain gush, lightning and the lower positive charge center in thunderstorms. Journal of Geophysical Research, 89:11816, 1984.

Jehl, A., Blanc, T., Farges, E. Color pictures of sprites from non-dedicated observation on board the International Space Station. Geophysical Research Space Physics, 118:454, 2013.

Kane, J. A. Arctic measurements of electron collision frequencies in the D-Region of the Ionosphere. Journal of Geophysical Research, 64:113, 1959.

Kosar, B., Liu, N., and Rassoul, H. K. Luminosity and propagation characteristics of sprite streamers initiated from small ionospheric disturbances at sub-breakdown conditions. Journal of Geophysical Research Letters., 117:A08328, 2012.

Kosch, M. J., Pedersen, T., and Esposito, R. Wide angle mirror system design for distortion less imaging of the sky. Applied optics., 48:4703, 2009.

Kotaki, M., and Katoh, M. The global distribution of thunderstorm activity observed by the ionosphere sounding satellite (ISS-b). Journal of Atmospheric and Terrestrial physics, 45:843, 1983.

Krehbiel, P. R. The Electrical Structure of Thunderstorms. In: Geophysics Study committee, ed. The Earth's Electrical Environment. Number 90. Washington D. C: National Academy Press, 1986.

Kuo, C. L., Hsu, R. R., Chen, A. B., Su, H. T., and et al. Electric fields and electron energies inferred from the ISUAL recorded sprites. Geophysical Research Letters,32:L19103, 2005.

Laing, A. G., and Fritsch, J. M. Mesoscale convective complexes in Africa. Quarterly Journal of the Royal Meteorological Society, 121:2254, 1993.

Laing, A. G., and Fritsch, J. M. The global population of mesoscale convective complexes. Quarterly Journal of the Royal Meteorological Society 123:389, 2004.

Lang, T. J., Miller, L. J., Weisman, M., Rutledge, S. A., and et al. The severe Thunderstorm electrification and precipitation study. Bulletin of the American Meteorological Society, 85(8):1107, 2004.

Lay, E. H., Holzworth, H. R., Rodger, J. C., Thomas J. N. and et al. WWLLN Global Lightning Detection System: Regional Validation Study in Brazil. Geophysical Research, 31(3):L03102, 2004.

Liu, N., Kosar, B., Sadighi, S., Dwyer, J. R., and Rassoul, H. K. Formation of streamer discharges from an isolated ionization column at subbreakdown conditions. Physical Review. Letters, 109:2, 2012.

Liu, N., Dwyer, J. R., Stenbaek-Nielsen, H. C., and McHarg, M. G. Sprites streamer initiation from natural mesospheric structures. Nature Communication., 29:7540,2015.

Liu, N. Y., and Pasko, V. P. Effects of photo-ionization on propagation and branching of positive and negative streamers in sprites. Journal of Geophysical Research, 109:A04301, 2004.

Liu, N. Y., and Pasko, V. P. Molecular nitrogen LBH band system far-UV emissions of sprite streamers. Geophysical Research Letters, 32:L05104, 2005.

Liu, N. Y., Boggs, L. D., and Cummer, S. A. Observation-constrained modeling of the ionospheric impact of negative sprites. Geophysical Research Letters, page 43,2016.

Lu, G., Cummer, S. A., Li, J., Zigoneanu, L., and et al. Coordinated observations of sprites and in-cloud lightning ash structure. Geophysical Research Letters., 118:6607, 2013.

Lyons, W. A. Characteristics of luminous structures in the stratosphere above thunderstorm as imaged by a low-light video. Geophysical Research Letters, 21:875,1994.

Lyons, W. A. Sprite observations above the U.S. high plains in relation to their parent thunderstorm systems. Journal of Geophysical Research., 101:29,641, 1996.

Lyons, W. A. The meteorology of Transient Luminous Events- An Introduction and overview, chapter 2, page 19. Springer, 2004.

MacKenzie, T., and Toynbee, H. Meteorological phenomena. Nature, 33:26, 1886.

Maddox, R. A. Mesoscale convective complexes. Bulletin of the American Meteorological Society, 1374:61,1980.

Malan, D. J. Sur les decharges orageuses dans la haute atmosphere. Academie des Sciences, 1937.

Malan, D. J. Physics of Lightning. Number 176. English University Press,London,1963.

Mansell, E. R., Macgorman, D. R., Ziegler, C. L., and Straka, J. M. Change structure and lightning sensitivity in a simulated multicell thunderstorm. Journal of Geophysical Research, 110:D12101, 2005.

Martinez, P., Kilkenny, M. D., Cox, G., Carter D. B., and et al., The Automatic Photometric Telescope at the South African Astronomical Observatory. Astronomical Society of Southern Africa, 61:102, 2002.

Matsudo, Y., Suzuki, T., Hayakawa, M., Yamashita, K., and et al. Characteristics of Japanese winter sprites and their parent lightning as estimated by VHF lightning and ELF transients. Journal of

Atmospheric and Solar-Terrestrial Physics, 69:1431, 2007.

Mende, S. B., Rairden, R. L., and Swenson, G. R. Sprite spectra; N2 1 PG band identification. Journal of Geophysics Research, 22:263, 1995.

Mezuman, K., Price, C., and Galanti, E. On the spatial and temporal distribution of thunderstorm cells. Environment Research Letters, 21:1088, 2014.

Michell, G. R., Grydeland, T., and Samara, M. Characteristics of poker at incoherent scatter radar (PFISR) naturally enhanced ion-acoustic lines (NEIAL) in relation to auroral forms. Ann Geophys, 32:1333, 2014.

Milikh, G. M., and Papadopoulos, K. On the physics of high altitude lightning. Geophysical Research Letters, 22:85, 1995.

Mlynarczyk, J., Bor, J., Kulak, A., Popek, M., and et al. An unusual sequence of sprites followed by a secondary TLE: An analysis of elf radio measurements and optical observations. Journal of Geophysical Research, 120:2241, 2015.

Moore, C. B., and Vonnegut, B. The Thundercloud: Physics of Lightning. Number 51. Academic Press, 1977.

Moran, M. J., and Morgan, M. D. Meteorology, the Atmosphere and Science of Weather. Macmillan Collage, New York, 1994.

Morrill, J., Bucsela, E., Siefring, C., Heavner M., and et al. Electron energy and electric field estimates in sprites derived from ionized and neutral N2 emissions. Geophysical Research Letters, 29:1462, 2002.

Neubert, T, H., Allin T., Stenbaek-Nielsen, H., and Blanc, E. Sprites over Europe. Geophysical Research Letters, 28:3585, 2001.

Neubert, T., Ostgaard, N., Reglero, V., Blanc, E., and et al. The ASIM Mission on the International Space Station. Space Science Reviews, 26:215, 2019.

Neubert, T., Rycroft, M., Farges, T., Blanc, E., and et al. Recent results from studies of electric discharges in the mesosphere. Surveys in Geophysics, 29:71, 2008.

Nnadih, S., Kosch, M., Martinez, P., and Bor, J. First ground-based observations of sprite over southern Africa. South African Journal of Science, 9/10:84, 2018.

Ohkubo, A., Fukunishi, H., Takahashi, Y., and Adachi, T. VLF/ELF sferic evidence for in-cloud discharge activity producing sprites. Geophysical Research Letters, 32:L04812, 2005.

Orville, R. E., and Spencer, D. W. Global lightning ash frequency. Monthly Weather Reviews, 107:934, 1979.

Papitashvili, N. MSIS-E-90 Atmosphere Model, 2018. URL `https://ccmc.gsfc.nasa.gov/modelweb/models/msis_vitmo.php`.

Pasko, V. P. Red sprite discharges in the atmosphere at high altitude: the molecular physics and the similarity with laboratory discharges. Plasma Sources. SciTechnol, 16:13, 2007.

Pasko, V. P. Recent advances in theory of transient luminous events. Journal of Geophysical Research., 115, 2015.

Pasko, V. P., Inan, U. S., and Bell, F. T. Sprite produced by quasi-electrostatic heating and ionization in the lower ionosphere. Journal of Geophysical Research,102:4529, 1997.

Pasko, V. P., Inan, U.S., and Bell, T.F. Spatial structure of sprites. Geophysical Research Letters, 12:2123, 1998.

Pasko, V. P., Qin, J., and Celestin, S. Toward better understanding of sprite Streamers: Initiation, morphology, and polarity asymmetry. Surveys in Geophysics, 34:797, 2013.

Pincon, J. L., Blanc, E., Blelly P. L., Parrot, M., and et al. TARANIS - scientific payload and mission strategy. IEEE, 9: 978, 2011.

Powell, G. Lightning. Marine Observer, 38:173, 1968.

Price, C. Global Thunderstorm Activity, chapter 4. Springer, 2004.

Price, C. Lightning sensors for observing, tracking and nowcasting severe weather.Sensors, 8:157, 2013.

Qin, J., Celestin, S., and Pasko., V. P. Minimum charge moment change in positive and negative cloud to ground lightning discharges producing sprites. Geophysical Research Letters, 39:L22801, 2012.

Qin, J., Celestin, S., Pasko, V. P., Cummer, S. A., and et al. Mechanism of column and carrot sprites derived from optical and radio observations. Geophysical Research Letters, 40:4777, 2013.

Raizer, Y. P., Milikh, G. M., Shneider, M. N., and Novakovski, S. V. Long streamers in the upper atmosphere above thundercloud. Journal of Physics, 31:3255, 1998.

Rakov, V. A., and Uman, M. A. Lightning: Physics and effect. Cambridge University Press, UK, 2003a.

Rakov, V. A., and Uman, M. A. Lightning Physics and Effects. Number 67. Cambridge University Press, New York, 2003b.

Rodger, C. J. Red sprites, upward lightning, and VLF perturbations. Reviews of Geophysics., 37:317, 1999.

Rodger, C. J., Brundell, J. B., Dowden, R. L., and Thomson, N. R. Location accuracy of long distance VLF lightning location network. Annales. Geophysicae., 22:747,2004.

Rudlosky, S. D., and Shea, D.T. Evaluating WWLLN performance relative to TRMM/LIS. Journal of Geophysical Research, 40:2344, 2013.

Sao-Sabbas, F. T., Sentman, D. D., Wescott, E. M., Pinto Jr, O., and et al. Statistical analysis of space-time relationship between sprites and lightning. Journal of Atmospheric and Solar-terrestrial Physics., 65:525, 2003.

Sato, M., and Fukunishi, H. Global sprite occurrence locations and rates derived from triangulation of Transient Schumann Resonance events. Journal of Geophysical Research Letters., 30:1859, 2003.

Sato, M. T., Ushio, T., Morimoto, M., Kikuchi, H., and et al. Overview and early results of the global lightning and sprite measurements mission. Journal of Geophysical Research: Atmosphere, 120:3822, 2015.

Saunders, C. P. A review of thunderstorm electrification processes. Journal of Applied Meteorology,32:642, 1993.

Sentman, D. D., and Wescott, E. M. Red sprites and Blue Jets, Geophysical Institute video production. Technical report, University of Alaska, Fairbanks, 1994.

Sentman, D. D., Wescott, E. M., Osborne, D. L., Hampton, D. L., and et al. Preliminary results from the Sprites94 campaign: Red sprites. Journal of Geophysical Research Letters, 22:1205, 1995.

Serge, S., Mlynarczyk, J., Fullekrug, M., Pineda, N., and et al. Dancing sprites: Details analysis of two case studies. Journal of Geophysical Research., 122:3173,2015.

Shevtsov, B. M., Firstov P. P., Cherneva, V. N., Holzworth R. H., and et al. Lightning and electrical activity during the Shiveluch volcano eruption on 16 November 2014. Natural Hazards and Earth System Sciences, 16:817, 2016.

Soula, S., van der Velde, O., Montanya, J., Neubert, T., and et al. Analysis of thunderstorm and lightning activity associated with sprites observed during the EuroSprite campaigns: Two case studies. Atmospheric Research Letters, 91:514,2009.

Soula, S., Kasereka J. K., Georgis, J.F., and Barthe, C. Lightning climatology in the Congo Basin. Atmospheric Research Letters, 178:304, 2016.

Stanley, M. High-speed video of initial sprite development. Journal of Geophysical Research Letters, 26:3201, 1999.

Stenbaek-Nielsen, H., Kanmae, C. T., McHarg, M. G., and Haaland, R. High-speed observations of sprite streamers. Surveys in Geophysics, 34:769, 2013.

Stewart, W. Watec902 and 910 series cameras. Technical report, Nemetode, 2015. Available at `http://www.nemetode.org/Technical%20Notes/TechNote%2001%20Watec%20Cameras%2020150127_03.pdf`

Surkov, V. V., and Hayakawa, M. Underlying mechanisms of Transient Luminous Events: a review.

Annales Geophysicae, 30:1185, 2012.

Suszcynsky, D. M., Roussel-Dupre, R., Lyons, W. A., and Armstrong, R. A. Blue-light imagery and photometry of sprites. Journal of Atmospheric and Solar Terrestrial Physics, 60:801, 1998.

Suzuki, T., Hayakawa, M., Matsudo, Y., and Michimoto, K. How do winter thundercloud systems generate sprite-induced lightning in the Hokuriku area of Japan? Geophysical Research Letters, 33:10,467, 2006.

Takahashi, T. Riming electrification as a charge generation mechanism in thunderstorms. Journal of the Atmospheric Sciences, 35:1536, 1978.

Taranenko, Y., and Roussel-Dupre, R. High altitude discharge and gamma-ray ashes: A manifestation of runaway air breakdown. Geophysical Research Letters,23:571, 1996.

Taylor, M. J., Bailey, M. A., Pautet, P. D., Cummer, S. A., Jaugey, N., and et al. Rare measurements of a sprite with halo event driven by a negative lightning discharge over Argentina. Geophysical Research Letters, 35:L14812, 2008.

Technology, Andor. Solis software packages. Technical report, Andor Technology, 2018. Available at `http://www.andor.com/pdfs/literature/Andor_iXon3_EMCCD_Brochure.pdf`

The South African Weather Service Lightning Detection Network, Annual Report 2017-2018. Available at `http://www.weathersa.co.za/Documents/AnnualReports/SAWS_AR_2017_2018_v40.pdf`

Tyson, P. D. Climatic change and variability in southern Africa. Number 131.Oxford University Press, 1986.

Uman, M. A. The Lightning Discharge. International Geophysics Series, 1987.

Vaisala, AZ. Data fusion concepts for storm nowcasting. Tucson Conference Proceeding. 17th International. Lightning Detection Conference, 17, 2002.

Valdivia, J. A., Milikh, G., and Papadopoulos, K. Red sprites: Lightning as a fractal antenna. Geophysical Research Letters, 24:3169, 1997.

Vaughan, O. H. Recent observations of lightning discharges from the top of a Thundercloud into the clear air above. Journal of Geophysical Research., 94:13,1989.

Vaughan, O.H., and Vonnegut, B. Lightning to the ionosphere? Weatherwise., 70:35, 1982.

Virts, K. S., Katrina, S., Wallace, J., Hutchins, M. L. and et al. Diurnal and seasonal lightning variability over the gulf stream and the Gulf of Mexico. Journal of the Atmospheric Sciences, 72:2657, 2015.

Vonnegut, B. Cloud to stratosphere lightning. Weather, 35:56, 1980.

Watts, A. New finding on sprite formation above thunderstorms. Technical report, WUWT., January 2016. URL `http://wattsupwiththat.com/2015/06/29/128300/>`.

Wescott, E. M., Sentman, D. D., Osborne, D., Hampton, D., and et al. Preliminary results from the Sprites94 Aircraft Campaign: 2. Blue Jets. Geophysical Research Letters, 22:1209, 1995.

Wescott, E. M., Stenbaek-Nielsen, H. C., Sentman, D. D., Heavner, M. J., Moudry, D. R., and et al. Triangulation of sprites, associated halos and their possible relation to causative lightning and micrometeors. Journal of Geophysical Research,106:10,467, 2001.

William, B. L., Vaughan, O. H., Blakeslee, R. J., Vonnegut, B., and et al. The role of the space shuttle videotapes in the discovery of Sprites, Jets, and ELVES, 1998. URL `https://ghrc.nsstc.nasa.gov/lightning/sprites.html`.

Williams, E. R., Lyons, W. A., Hobara, Y., Mushtak, V. C., and et al. Ground-based detection of sprites and their parent lightning ashes over Africa during the 2006 AMMA campaign. Journal of Royal Meteorological Society., 136:257, 2010.

Williams, E. R. The tripole structure of thunderstorm. Journal of Geophysical Research, 94:13151, 1989.

Wilson, C. T. On some determinations of the sign and magnitude of electric discharge in lightning ashes. Proceedings of the Royal Society of London. Mathematical, Physical and Engineering Science, 92(644):555, 1916.

Wilson, C. T. A theory of thundercloud electricity. Proceeding - Royal Meteorological Society London, 236:297, 1956.

Winckler, J. R., Lyons, W. A., Nelson, T. E., and Nemzek, R. J. New high-resolution ground-based studies of sprites. Journal of Geophysical Research., 101:6997, 1996.

Winckler, J. R., Lyons, W. A., Nelson, T. E., and Nemzek, R. J. New high-resolution ground-based studies of cloud-ionosphere discharges over thunderstorms. Journal of Geophysics Research letters, 101:6997, 1999.

Wood, C. A. Unusual lightning. Weather., 6:64, 1951.

Wood, G. T. Geo-location of individual lightning discharges using impulsive VLF Electromagnetic waveforms. PhD thesis, Stanford University UK, 2004.

Yair, Y., Israelevich, P., Devir, D. A., Moalem, M., and et al. New observations of sprites from the space shuttle. Journal of Geophysics Research letters, 109:34, 2004.

Yang, J., Yang, M., Liu, C., and Feng, G. Case studies of sprite-producing and non sprites-producing summer thunderstorms. Advance Atmosphere Science, 30:1786, 2013.

Yaniv, R., Yair, Y., Price, C., Bor, J., and et al. Ground-based observations of the relations between lightning Charge Moment Change and the physical and optical properties of column sprites. Journal of Atmospheric and Solar-terrestrial Physics,107:60, 2013.

Yaniv, R., Yair, Y., Price, C., Bor, J., and et al. Ground-based observations of the relations between lightning charge-moment-charge and the physical and optical properties of column sprites. Journal of Atmospheric and solar-terrestrial physics, 107:60, 2014.

Zhu, Y., Rakov, V. A., Tran, M. D., Stock M. G., and et al. Evaluation of ENTLN performance characteristics based on the ground truth natural and rocket-triggered lightning data acquired in Florida. Journal of Geophysical Research: Atmospheres, 122:9858, 2017.

Zipser, E. J., Cecil, D. J., Nesbitt, S. W., and Yorty, D. P. Where are the most intense thunderstorms on Earth? Bulletin of the American Meteorological Society, 87:1057, 2006.